Titre: Title:	Evaluation and effects of temperature in optoelectronic waveguide devices
Auteur: Author:	Mathieu Allard
Date:	1998
Type:	Mémoire ou thèse / Dissertation or Thesis
Référence: Citation:	Allard, M. (1998). Evaluation and effects of temperature in optoelectronic waveguide devices [Master's thesis, École Polytechnique de Montréal]. PolyPublie. https://publications.polymtl.ca/6752/

Document en libre accès dans PolyPublie
Open Access document in PolyPublie

URL de PolyPublie: PolyPublie URL:	https://publications.polymtl.ca/6752/
Directeurs de recherche: Advisors:	Rémo A. Masut, & Marc Bourdeau
Programme: Program:	Unspecified

UNIVERSITÉ DE MONTRÉAL

Evaluation and Effects of Temperature in Optoelectronic Waveguide Devices

Mathieu Allard

Département de génie physique et de génie des matériaux
École Polytechnique de Montréal

ÉCOLE
POLYTECHNIQUE
MONTRÉAL

Mémoire présenté en vue de l'obtention
du diplôme de maîtrise ès sciences appliquées
(Génie physique)

Juillet 1998

The author has granted a non-exclusive licence allowing the National Library of Canada to reproduce, loan, distribute or sell copies of this thesis in microform, paper or electronic formats.

The author retains ownership of the copyright in this thesis. Neither the thesis nor substantial extracts from it may be printed or otherwise reproduced without the author's permission.

L'auteur a accordé une licence non exclusive permettant à la Bibliothèque nationale du Canada de reproduire, prêter, distribuer ou vendre des copies de cette thèse sous la forme de microfiche/film, de reproduction sur papier ou sur format électronique.

L'auteur conserve la propriété du droit d'auteur qui protège cette thèse. Ni la thèse ni des extraits substantiels de celle-ci ne doivent être imprimés ou autrement reproduits sans son autorisation.

0-612-37424-6

Canada

UNIVERSITÉ DE MONTRÉAL

ÉCOLE POLYTECHNIQUE DE MONTRÉAL

Ce mémoire intitulé:

Evaluation and Effects of Temperature in

Optoelectronic Waveguide Devices

présenté par ALLARD, Mathieu

en vue de l'obtention du diplôme de maîtrise ès sciences appliquées

a été dûment accepté par le jury d'examen constitué de

Prof. MEUNIER, Michel, Ph.D., président

Prof. MASUT, Remo A., Ph.D., membre et directeur de recherche

M. BOUDREAU, Marcel, Ph.D., membre et co-directeur de recherche

Prof. FAUCHER, Guy, D.Sc., membre

SERVICE DES ÉTUDES
SUPÉRIEURES

AUTORISATION DE CONSULTATION ET DE REPRODUCTION
(Documents et disquettes)

DESCRIPTION DU DOCUMENT:

Auteur: Mathieu Allard

Titre: Evaluation and Effects of Temperature in Optoelectronic Waveguide Devices

☐ Mémoire M.Ing. : 19___		☐ Thèse: 19___	
☒ Mémoire M.Sc.A.: 1998		☐ Autre (spécifier): _____	

Disquettes incluses   oui ☐   non ☒

Reproduction permise   oui ☒   non ☐

Je déclare par la présente être le seul auteur du document cité.

J'autorise l'École Polytechnique de Montréal à prêter ce document à d'autres institutions ou individus à des fins d'étude ou de recherche.

J'autorise également l'École Polytechnique de Montréal ou son contractant à reproduire ce document et à prêter ou vendre des copies de ce document aux personnes intéressées à des fins d'étude ou de recherche.

Cette autorisation ne peut être révoquée, mais elle n'est pas nécessairement exclusive. Par ailleurs, je me réserve tous les autres droits de diffusion ou de publication.

_____   98-08-24
Signature de l'étudiant   Date

La présente autorisation entre en vigueur à la date ci-dessus à moins que le Service des études supérieures n'ait autorisé son report à une date ultérieure. Dans ce cas, l'autorisation est reportée au _____.

SES-09A (95-10)

Acknowledgements

I would like to thank my directors, Dr. Remo Masut (École Polytechnique) and Dr. Marcel Boudreau (Nortel) for their support, advice and help. Many thanks also to all the people at Nortel who kindly helped me while I realized my project there, especially Robert Mallard, Scott Bradshaw, Claude Rolland, Arthur Smith and Jeffrey Yu. Thanks also to all the people who provided valuable advice and help at one point or another: Nicolas, Roxane, Stéphane, Laurent, Patrick, Damien, Dominique, etc.

Abstract

The absorption of light and the passage of current in optoelectronic devices generate heat, which may significantly raise the internal temperature. This can result in potentially serious detrimental effects. The operation characteristics of the device can change, for example, the wavelength of emission of a laser or the switching voltage of a modulator. High temperatures can also trigger an accelerated degradation of the device, and thus affect its reliability.

The present work has been carried out on a multi-purpose multiple-quantum-well waveguide device, incorporating top metal contact electrodes. The device could serve as an electro-absorption or an electro-refraction modulator by making use of the quantum-confined Stark effect. Traditional techniques, such as infrared microscopy or photoluminescence, can not be used on this device, because of the limitations imposed by its particular geometry. To study the thermal issues arising in the waveguide device, an experimental technique and an advanced thermal model were developed, both capable of measuring temperature in the device. The experimental technique uses liquid crystals to measure the maximum temperature present on the surface of the device for any combination of applied voltage and photocurrent generated when light is absorbed. The technique is easy to implement, inexpensive, fast and versatile. In conjunction with the experimental work, a finite-element 3-D thermal model of the waveguide device was constructed, to obtain the temperature in the active region of the device. The model takes into consideration the fact that both the optical absorption in the waveguide and the thermal conductivity of the various materials composing the device vary with temperature. This requires the knowledge of the absorption coefficient in the waveguide, which was measured over broad ranges of voltage and temperature. The temperatures

predicted by the model were compared to the experimental data: the agreement was found to be good in most conditions, thus proving the validity of the thermal model.

The model has shown that thermal runaway can occur in the waveguide device under certain combinations of voltage and photocurrent. Thermal runaway results from the fact that optical absorption increases with temperature: this causes an additional heating that, in turn, raises the local temperature further. The cycle could repeat itself until damage is induced in the device, possibly leading to catastrophic failure. Another important achievement of both the model and the experimental technique was to produce evidence of a thermal cross-talk between the laser diode and the waveguide device in a hybrid configuration incorporating both devices. Thermal cross-talk causes the internal temperature to be higher in hybrid devices than in stand-alone waveguide devices for identical voltage and photocurrent, due to the heat generated in the laser. This was corroborated by further experiments where the voltage and photocurrent leading to the instantaneous blow-up of the waveguide device were measured: the heat produced by the integrated laser causes the blow-up to happen at a lower voltage.

A large number of devices coming from nine different wafers, on which the absorption and the thermal behavior had already been measured, were submitted to high temperatures and voltages for extended periods of time to simulate accelerated aging, in order to evaluate their long-term reliability. The correlation was evaluated between the absorption in the waveguide, the temperature rise, blow-up voltage, other electro-optic quantities and the failure rate during aging tests, as part of a search for early indicators of reliability. A good correlation was found between the optical absorption and the temperature rise. This analysis also suggests that a correlation exists between the absorption and the results of the aging tests: a poor performance in aging tests could be related to high absorption and temperature rise. This supports eventual design revisions in order to improve the performance under high-stress conditions and potentially the reliability of the waveguide device.

Résumé

L'absorption de lumière et le passage de courant dans un dispositif opto-électronique produisent de la chaleur qui peut entraîner une augmentation importante de la température interne. Les conséquences potentiellement néfastes sont multiples. Tout d'abord, les caractéristiques d'opération d'un dispositif seront altérées, par exemple, la longueur d'onde d'émission d'une diode laser ou la tension de commutation d'un modulateur optique. Une température élevée peut aussi provoquer une dégradation accélérée du dispositif et affecter sa fiabilité.

Pour le présent travail, on a utilisé un dispositif à guide d'ondes à usages multiples, comprenant des puits quantiques multiples et des électrodes métalliques. Ce dispositif peut être utilisé comme modulateur à électro-absorption ou électro-réfraction grâce à l'effet Stark à confinement quantique. Les techniques traditionnelles de mesure de température, telles la microscopie infrarouge ou la photoluminescence, sont ici inapplicables à cause de la géométrie particulière du dispositif. Pour étudier les problèmes thermiques, une technique expérimentale et un modèle thermique ont été développés, tous deux capables d'évaluer la température du dispositif. La technique expérimentale permet la mesure de la température de surface au moyen de cristaux liquides. Elle est abordable, rapide, versatile et facile à utiliser. Parallèlement au travail expérimental, un modèle thermique tridimensionnel du dispositif à guide d'ondes a été construit, pour obtenir la température dans sa région active. Le modèle tient compte du fait que l'absorption optique dans le guide d'ondes et la conductivité thermique des divers matériaux présents dans le dispositif varient tous deux avec la température. Le coefficient d'absorption optique, une donnée requise par le modèle, a été au préalable mesuré sur de larges plages de température et de tension. Quand les températures obtenues avec le

modèle sont comparées aux données expérimentales, on trouve que l'accord est en général bon, démontrant ainsi la validité du modèle.

Le modèle a démontré qu'un phénomène d'emballement thermique peut exister dans le dispositif lorsqu'il est soumis à des conditions de courant et de tension particulières. L'emballement thermique provient du fait que l'absorption optique augmente avec la température: la production de chaleur supplémentaire résultante augmente la température d'autant plus. Le cycle peut ainsi se répéter jusqu'à ce que la température soit suffisamment élevée pour endommager ou détruire le dispositif. Un autre accomplissement important du modèle et de la technique expérimentale a été de mettre en évidence l'interférence thermique existant entre la diode laser et le dispositif à guide d'ondes dans un dispositif hybride incorporant les deux. À cause de l'interférence thermique, la température est plus élevée dans le dispositif hybride que dans le dispositif à guide d'ondes seul, pour des tensions et de photocourants identiques. Ceci a été corroboré par une autre série d'expériences qui a montré que la tension et le photocourant provoquant la destruction subite du dispositif à guide d'ondes sont réduites dans un dispositif hybride, en raison de la chaleur générée par le laser.

Des dispositifs à guide d'ondes provenant de neuf pastilles, dont l'absorption optique et le comportement thermique ont été mesurés, ont été soumis à des température et tension élevées pour provoquer un vieillissement accéléré, de façon à évaluer leur fiabilité à long terme. On a évalué la corrélation entre le taux de défaillance durant ces tests et l'absorption optique, l'élévation de la température, la tension de destruction subite et d'autres données semblables, dans le but de trouver des indicateurs immédiats de la fiabilité. Une bonne corrélation a été trouvée entre l'absorption optique et l'élévation de température. Une corrélation raisonnable existe également entre l'absorption et la performance au cours des tests de vieillissement accéléré. Ceci suggère des modifications possibles au design du dispositif pour améliorer sa performance face à des conditions d'opération extrêmes et, ainsi, améliorer sa fiabilité.

Condensé français
Comportement thermique de dispositifs opto-électroniques à guides d'ondes

Les systèmes de télécommunication à fibres optiques font fréquemment appel à des dispositifs opto-électroniques pour accomplir diverses tâches telles la production de lumière, la modulation des signaux optiques et leur détection. Ces dispositifs, souvent composés de matériaux semi-conducteurs, sont très sensibles aux changements de température interne. Celle-ci influence profondément leur fonctionnement; de plus, une température interne élevée risque de provoquer une dégradation accélérée du dispositif. Étant donné que les puissances lumineuses utilisées dans ces dispositifs sont en augmentation constante, les problèmes reliés à l'échauffement interne prennent de plus en plus d'importance dans le contexte actuel. À cet effet, il est essentiel de bien caractériser cet échauffement et ses conséquences sur le fonctionnement et la fiabilité des dispositifs opto-électroniques.

Description des dispositifs opto-électroniques

Dans les systèmes de télécommunication actuels, dont les débits de transmission peuvent atteindre les centaines de milliards de bits par seconde, la lumière est habituellement produite par une diode laser polarisée en continu, alors que la modulation du signal optique est accomplie par un second dispositif, le modulateur. Ces deux dispositifs utilisent une géométrie de type guide d'ondes. Le passage du courant et l'absorption de lumière dans ces dispositifs y engendrent un échauffement interne pouvant être considérable. À cause de la variation de la bande interdite du semi-conducteur avec la tempé-

rature, cette dernière affecte profondément les propriétés des dispositifs opto-électroniques. Par exemple, dans une diode laser, l'efficacité interne et la longueur d'onde d'émission varient toutes deux avec la température. Typiquement, dans un guide d'ondes, l'indice de réfraction et l'absorption optique varient tous deux avec la température. Une haute température pourra également causer un vieillissement prématuré du dispositif et affecter sa fiabilité à long terme.

De façon à quantifier l'échauffement interne, de nouvelles techniques doivent être développées; celles-ci doivent être peu dispendieuses, versatiles, posséder de bonnes résolutions spatiale (~1 μm) et en température (~1°C) et ne pas requérir de préparation élaborée des échantillons. Malheureusement, les techniques traditionnelles ne peuvent pas être appliquées à ce problème. Par exemple, la microscopie infrarouge possède une résolution spatiale insuffisante, et toutes les méthodes utilisant une sonde optique (photoluminescence, spectroscopie Raman, etc.) sont inapplicables puisque les régions d'intérêt sont recouvertes d'électrodes métalliques opaques. Ce document présente une technique novatrice utilisant des cristaux liquides pour mesurer la température à la surface de ces dispositifs.

Les dispositifs utilisés pour ce travail sont des dispositifs à guide d'ondes contenant des puits quantiques multiples et pouvant accomplir plusieurs fonctions. Les couches semi-conductrices y forment une jonction *p-i-n* qui permet d'établir un champ électrique dans les puits quantiques lorsqu'elle est polarisée en inverse. À cause de l'effet Stark à confinement quantique, ceci engendre un changement de l'indice de réfraction et du coefficient d'absorption optique dans le guide. Selon la grandeur des tensions appliquées, le dispositif peut être utilisé comme un modulateur d'intensité à électro-absorption ou comme un modulateur de phase à électro-réfraction. Deux variantes du dispositif ont été utilisées: dans la première, l'électrode recouvrant le guide est presque carrée (220 x 200 μm), alors que dans l'autre, elle est longue, fine et confinée au-dessus de l'arête formant le guide (600 x 2 μm). Enfin, pour certaines utilisations, il est utile de

joindre une diode laser au dispositif à guide d'ondes, pour disposer d'une source lumineuse intégrée; dans ce cas, on parle de configuration **hybride**.

Méthode de mesure de température à cristaux liquides

La méthode expérimentale présentée dans ce chapitre utilise la transition entre les phases nématique et isotrope d'un cristal liquide (CL) pour mesurer la température à la surface d'un dispositif opto-électronique. Dans la phase **nématique**, toutes les molécules du CL ont leur axe principal orienté dans la même direction, et le CL est biréfringent, alors que dans la phase **isotrope**, l'orientation de chaque molécule est aléatoire et il n'y a pas de biréfringence. Cette transition, qui se produit à une température connue, peut être observée au moyen d'un microscope possédant deux filtres polarisant croisés: un près de la lampe et un dans l'oculaire. Le dispositif recouvert de cristal liquide apparaît en clair, alors que les régions où la température de surface dépasse la température de transition seront sombres. Il est possible d'ajuster la puissance optique injectée dans le guide d'ondes de façon à ce que la tache sombre rapetisse jusqu'à ne devenir qu'un fin point noir, sur le point de disparaître : dans ce cas, la température maximale retrouvée à la surface du dispositif est égale à la température de transition du CL.

La technique est utilisée de la façon suivante : des tensions variant de 5 à 9 V sont appliquées au dispositif à guide d'ondes, la puissance optique est ajustée comme indiqué ci-dessus et le **photocourant** (courant généré par l'absorption de lumière) à ce point est enregistré. Pour élargir la plage de température pouvant être étudiée de la sorte, trois cristaux liquides sont utilisés, dont les températures de transition sont 42, 58 et 73°C. Le résultat est une série de courbes sur un graphique donnant la température maximale à la surface en fonction du photocourant et de la tension. On y voit que la température augmente avec ces deux quantités, puisque la puissance électrique dissipée sous forme de chaleur est donnée par le produit de celles-ci. Cependant, la relation entre la température et le photocourant est super-linéaire et non pas linéaire: la raison en est qu'à mesure que la température croît, le coefficient d'absorption dans le guide augmente aussi, de

sorte que la lumière est complètement absorbée dans une plus courte portion du guide. La production de chaleur étant confinée dans une plus petite région, la température augmente d'autant plus rapidement.

Ces mesures ont été réalisées sur des dispositifs seuls (pour lesquels la lumière provenait d'un laser externe) et hybrides, provenant de la même pastille. Sur les dispositifs hybrides, la température mesurée est significativement plus élevée que sur les dispositifs seuls, pour des courant et tension similaires, à cause de l'échauffement additionnel provenant du laser avoisinant. Il s'agit là de la preuve de l'existence d'une **interférence thermique** entre le laser et le dispositif à guide d'ondes. Des mesures faites sur des dispositifs à électrode étroite ont également montré que l'élévation de température varie significativement d'une pastille à l'autre mais peu entre les dispositifs provenant d'une même pastille. On croit que ces différences proviennent de différences entre l'absorption optique dans le guide d'une pastille à l'autre.

Bien que la méthode à CL ait fourni des résultats très satisfaisants, il subsiste des problèmes ayant trait à l'obtention d'un film mince (~ 5 μm) et uniforme à la surface du dispositif. Ces problèmes n'ont pas été complètement résolus à ce jour; bien qu'ils compliquent les mesures, la qualité des résultats n'en a pas souffert.

Mesures de tension de défaillance subite

Si la tension électrique appliquée à un dispositif est augmentée progressivement pendant que la puissance optique est maintenue constante, il advient un point où une destruction subite du dispositif se produit. Cette destruction survient suite à un échauffement excessif causant des dommages importants au dispositif. La mesure de la tension menant à la destruction subite constitue une indication de la robustesse du dispositif à ce type de défaillance. De telles mesures ont été effectuées sur des dispositifs à guide d'ondes à électrode étroite, en utilisant soit un laser intégré comme source lumineuse, soit un laser externe.

Après que la mesure ait été faite sur un grand nombre de dispositifs, le résultat est une série de points sur un graphique courant – tension, où chaque point correspond à une condition de défaillance. Ces points définissent l'ensemble des conditions pouvant causer la destruction immédiate des dispositifs. La conclusion la plus importante de ces expériences est que les défaillances subites surviennent à des courants et tensions moins élevées dans les dispositifs hybrides. Ceci est dû à l'échauffement engendré par le laser qui vient s'ajouter à celui déjà présent dans le guide d'ondes, augmentant ainsi la température interne des dispositifs. Cela signifie que l'interférence thermique entre le laser et le dispositif à guide d'ondes risque aussi de réduire la robustesse du dispositif dans des conditions menant à des températures internes élevées, et ainsi d'affecter potentiellement la fiabilité du dispositif.

Mesures d'absorption dans le guide d'ondes

Il est impératif de connaître le coefficient d'absorption dans le guide d'ondes en fonction de la température et de la tension appliquée, pour le travail de modélisation présenté au prochain chapitre. Deux séries de mesure ont été nécessaires. Dans un premier temps, on a calculé le coefficient d'absorption dans le guide sous une électrode longue de 600 μm, à partir de la mesure du photocourant et de la puissance optique à la sortie du guide, sur des plages de 0 à 10 V et de 10 à 70°C. L'atténuation maximale pouvant être mesurée de cette façon est d'environ 40 dB; une seconde série de mesure est nécessaire pour élargir la plage de conditions étudiées. Pour cela, un dispositif arborant une géométrie planaire, semblable à celle d'une photodiode, a été utilisé. Le photocourant y a été mesuré en fonction de la tension à des températures allant jusqu'à 220°C. Il est possible de combiner le résultat des deux ensembles d'expériences pour obtenir le coefficient d'absorption dans le guide sur des plages de 10 à 220°C et de 0 à 10 V.

Ces expériences montrent que l'absorption varie presque linéairement avec la température aux tensions élevées (près de 10 V), alors qu'elle augmente exponentiellement aux basses tensions (moins de 3 V) jusqu'à 180°C. Aux basses températures, l'absorption

augmente rapidement avec la tension, mais autour de 160°C, elle est virtuellement indépendante de la tension. L'absorption a également été mesurée sur des dispositifs provenant de plusieurs pastilles, ce qui permet d'étudier les différences d'une pastille à l'autre. Des différences significatives ont été trouvées, qui pourraient expliquer les différences observées d'une pastille à l'autre au cours des mesures de températures avec la méthode de cristaux liquides.

Enfin, la dépendance de l'absorption face à la longueur d'onde a été étudiée. Cette analyse révèle que la température et la longueur d'onde ont des influences semblables sur l'absorption optique.

Modélisation thermique

La méthode de CL ne fournit que la température à la surface des dispositifs, alors que c'est la température interne qui régit le fonctionnement du dispositif. La façon la plus simple d'obtenir celle-ci est de construire un modèle thermique du dispositif, donnant la température interne en fonction de la tension appliquée et de la puissance optique (ou du photocourant). Ce modèle a été créé avec l'aide du logiciel *Algor*, qui utilise un algorithme d'éléments finis pour calculer le profil de température dans le dispositif pour diverses combinaisons de tension et de photocourant. L'originalité de ce modèle est qu'il est inhomogène, à cause des multiples matériaux constituants, et non-linéaire, à cause de la dépendance en température du coefficient d'absorption et de la conductivité thermique du semi-conducteur.

La conductivité thermique des divers semi-conducteurs et l'expression de sa dépendance envers la température ont été trouvées dans la littérature scientifique sur le sujet. Pour tenir compte de cette dépendance, le modèle fait appel à la méthode de transformation de la température, conçue par Kirchoff. De même, plusieurs itérations dans le modèle sont nécessaires pour résoudre le problème de la dépendance en température de l'absorption optique et de celle de la génération de chaleur qui s'ensuit. Le résultat de cette analyse

est un profil de température tridimensionnel dans le dispositif pour une combinaison donnée de photocourant et de tension. L'ensemble des combinaisons courant – tension a été étudié de cette manière, pour des dispositifs seuls ou hybrides, possédant une électrode étroite ou large. Ces résultats peuvent être présentés efficacement sous la forme de cartes de températures donnant la température maximale à l'intérieur de la région active du dispositif en fonction du photocourant et de la tension, au moyen d'une échelle de couleur. Les prédictions du modèle peuvent être comparées directement avec les résultats expérimentaux pour vérifier la validité du modèle.

Le modèle montre que la température interne augmente de façon superlinéaire avec le courant et aussi avec la tension. Il existe certaines combinaisons courant – tension pour lesquelles aucune solution stable n'est trouvée avec le modèle : ceci est dû à un phénomène d'**emballement thermique**. Le passage d'un photocourant échauffe la région active, ce qui augmente la température interne et, par conséquent, le coefficient d'absorption; ceci confine encore plus l'échauffement et augmente localement la température. Ce cycle peut se répéter jusqu'à ce que la température soit suffisamment élevée pour endommager le dispositif: on parle alors d'emballement thermique. Sur les graphiques, ceci se manifeste par une soudaine augmentation de la température quand le photocourant dépasse un certain seuil.

Le modèle confirme également la présence d'une interférence thermique entre le laser et le dispositif à guide d'ondes dans les dispositifs hybrides. Une comparaison des résultats du modèle et de ceux obtenus expérimentalement montre un bon accord entre les deux, démontrant la validité du modèle. Le seul écart important est que le modèle prédit que l'emballement thermique se produit sous des conditions plus faibles (courant ou tension plus petits) que ce qui est observé expérimentalement. Ceci pourrait être le résultat de la grandeur finie des éléments, qui pourrait causer des erreurs importantes dans les conditions ou l'absorption de lumière est concentrée dans une très petite région. Enfin, le modèle montre que l'électrode large mène à des températures internes plus

basses qu'une électrode étroite, pour des courants et tensions semblables, à cause du fait que l'électrode large est mieux en mesure d'extraire la chaleur de la région chaude.

Comparaison des quantités électro-optiques

Une façon typique d'évaluer la fiabilité à long terme de dispositifs à semi-conducteurs est de les placer dans des conditions de stress thermique, électrique et optique élevés, de façon à provoquer un vieillissement accéléré. Il est alors possible d'étudier les mécanismes de dégradation sur des périodes de temps bien inférieures au temps de vie de vingt ans prescrit habituellement pour ces dispositifs. Cette méthode permet aussi de rejeter des lots de dispositifs qui sont sujets à une dégradation trop rapide. Le coût associé à ces tests est cependant élevé, puisqu'ils s'étendent habituellement sur plusieurs mois, et il serait utile de posséder des indicateurs immédiats de la performance d'un lot de dispositifs aux tests de vieillissement accéléré, de façon à éliminer les mauvais lots avant même qu'ils ne subissent ces tests.

Les données recueillies au cours de ce travail se prêtent très bien à la recherche de tels indicateurs. Pour ce faire, les mesures de l'élévation de température et de l'absorption optique ont été comparées entre elles et avec les résultats des tests de vieillissement accéléré. Une série de mesures supplémentaire a également permis d'ajouter à cette liste la tension donnant lieu à une destruction subite du dispositif, le courant de fuite et la tension engendrant un changement de phase de la lumière à la sortie du guide d'ondes de π radians. Cette tension est notée V_π, et est importante si le dispositif est utilisé comme modulateur de phase. En utilisant les données recueillies sur chaque pastille, la corrélation pour chaque paire de variables a été évaluée. Les résultats de cette étude montrent que l'absorption mesurée sur chaque pastille exhibe une bonne corrélation avec l'élévation de température, ce qui s'explique par le fait que la première constitue la cause de la seconde. Ces données montrent aussi une bonne corrélation avec V_π, compréhensible parce que l'absorption et le changement d'indice de réfraction sont liés par les relations de Kramers-Krönig. Aucune corrélation claire n'est observée entre ces

variables et la tension de défaillance instantanée et le courant de fuite. Quant aux résultats des tests de vieillissement accéléré, on peut observer une faible corrélation avec l'absorption dans le guide. Ceci n'est pas suffisant pour affirmer que l'absorption est un bon indicateur de la performance des dispositifs au cours des tests de vieillissement accéléré, mais suggère qu'une façon d'améliorer cette performance serait de modifier le design de ces dispositifs de façon à réduire l'absorption. Cette étude doit cependant être étendue à un plus grand nombre de pastilles pour soutenir cette affirmation.

Conclusion

La technique de cristaux liquides et le modèle thermique développés au cours de ce travail ont tous deux démontré leur utilité pour l'étude des problèmes reliés à l'échauffement interne dans les dispositifs opto-électroniques. La preuve de l'existence de l'interférence thermique entre le laser et le dispositif à guide d'ondes dans les dispositifs hybrides et l'étude du phénomène de l'emballement thermique constituent des exemples de résultats tangibles de ces techniques. Ces outils, maintenant arrivés à maturité, sont disponibles pour participer à des investigations de plus grande envergure, telle la recherche d'indicateurs de la performance des dispositifs au cours des tests de vieillissement accéléré.

Table of Contents

List of Figures

List of Tables

List of Acronyms and Symbols

EDFA	Erbium-Doped Fiber Amplifier
FEA	Finite-Element Algorithm
IC	Integrated Circuit
GPIB	General Purpose Interface Bus
HPVee	Hewlett-Packard Vee (graphical programming language)
LC	Liquid Crystal
MEMS	Micro-Electro-Mechanical Systems
MQW	Multiple Quantum Wells
OCE	Output Coupling Efficiency
PECVD	Plasma-Enhanced Chemical Vapor Deposition
PL	Photoluminescence
QCSE	Quantum-Confined Stark Effect
TEC	Thermo-Electric Cooler
WDM	Wavelength Division Multiplexing

V	Voltage	α	Absorption coefficient
I	Current	λ	Wavelength (in vacuum)
L	Optical power	η	Internal Efficiency
P	Electrical power	n	Exponent
T	Real Temperature	w	Active region width
θ	Transformed temperature	t	Active region thickness
σ	Thermal conductivity	e	Electronic charge
q	Heat per unit volume	h	Planck's constant
v	Volume	c	Speed of light
x, y, z	Space variables		

List of Appendices

Introduction

Everyone now acknowledges the importance of information in the modern world. The recent years have been the scene of a major revolution in the way information is acquired, transferred and treated. At the center of this revolution is the phenomenal growth of the Internet, which now provides a way for people all around the world to communicate freely, without regard to the physical distance separating them. To sustain the rapid growth of the telecommunication networks, pressure has been put on the industry to come up with new equipment capable of ever-increasing transmission rates. The manufacturers have answered this demand with a multitude of new components and technologies. The result is that one single optical fiber can now transmit hundreds of billions of bits of information per second over distances of hundreds, even thousands of kilometers. The components needed for high-speed transmission often make use of semiconductors to achieve different functions, such as light emission, modulation, routing and detection. Because they conduct electricity and guide light at the same time and present a good similarity with microelectronic integrated circuits, they are called **optoelectronic** components.

The data rate and optical powers transmitted over optical fibers have steadily increased over the years. The capacity and reach of optical fiber links have grown accordingly. This has unfortunately raised a number of new concerns. For example, one common detrimental side effect of increasing the optical power in optoelectronic components is to raise the temperature inside the devices because of the increased internal heating. The consequences of the temperature change are numerous and varied. In laser diodes, temperature has a strong influence on the efficiency, the wavelength of emission and the long-term reliability of the device; these issues have been studied extensively [1]. In

non-light-emitting devices such as optical modulators and switches, both the device operation and its reliability are affected by temperature; because these components are relatively new, little effort has been devoted to the study of thermal issues until now. It is nonetheless important to develop a good understanding of these issues, in order to continue to produce efficient and reliable optoelectronic components for optical fiber communications.

New tools need to be developed to study the temperature increase in optoelectronic devices under various operating conditions, and, reciprocally, how temperature affects the device operation. Two such tools were developed in the course of this work and are described in this document. The first one is an experimental technique that uses liquid crystals to measure the temperature on the surface of an optoelectronic chip. It is precise, simple and inexpensive, but has one serious drawback: it does not reveal the temperature inside the device, which would constitute the most important information, since the operation of the device is affected mainly by the internal temperature. An efficient way of obtaining this information is to construct a thermal model of the device. With a computerized model, a complete three-dimensional temperature profile in the device can be obtained for any combination of operating conditions (current, voltage, optical power, etc.). The advantage of proceeding with both an experimental technique and a model is that it is possible to compare the predictions of the model with experimental data to assess the validity of the model.

The two techniques are considered to be characterization tools, now mature enough so that they can take part in more comprehensive investigations. Two examples of such applications are given in this document: the activation energy estimation for the long-term degradation of the waveguide device (chapter 5), and the correlation of electro-optic properties, temperature rise and device lifetime under high-stress conditions (chapter 6). These investigations could produce information useful not only for research purposes, but also to commercial interests.

This document is divided in six chapters. The first explains the role played by optoelectronic devices in optical fiber telecommunications and the importance of thermal issues, and describes the samples on which the experiments have been carried out. The second chapter describes the liquid-crystal technique and shows the results of the measurements. The third chapter then presents the results of blow-up experiments performed on waveguide devices, which provide additional insight into the thermal issues arising in these devices. The fourth chapter describes the measurements of the optical absorption in the waveguide; this data is required to proceed with thermal modelling, which is the subject of the fifth chapter. The last chapter combines the data obtained from each set of experiments to investigate the existence of early indicators of the performance of the waveguide devices in aging tests. Even though all chapters are meant to be independent, the results from each set of experiments will be put in relation with each other as they are presented.

Chapter 1
Optoelectronic Components in Optical Fiber Communications

The ever-increasing traffic on telecommunication networks and the extremely rapid growth of the Internet have fueled over the past years the demand for high-bandwidth, cheap telecommunications links. At the same time, the advent of new technologies and components developed for optical fiber communications, such as fiber-based amplifiers and optical modulators, have permitted the industry to feed the demand with new systems capable of higher-speed and longer-distance communications. For example, in 1998, Nortel's best system is capable of delivering 160 billions bits of information per second in one single optical fiber. As the optical power and the data rate continue to increase, the manufacturers of these systems are faced with new problems. Among them, the increased heating generated in optoelectronic components is becoming a source of great concern, and the industry is devoting growing efforts to address this issue.

This first chapter gives an overview of how optoelectronic components are used in optical fiber systems. It also explains how high temperatures affect them and reviews the existing methods of measuring the temperature in optoelectronic devices. Finally, the devices on which the experiments have been performed are described in detail.
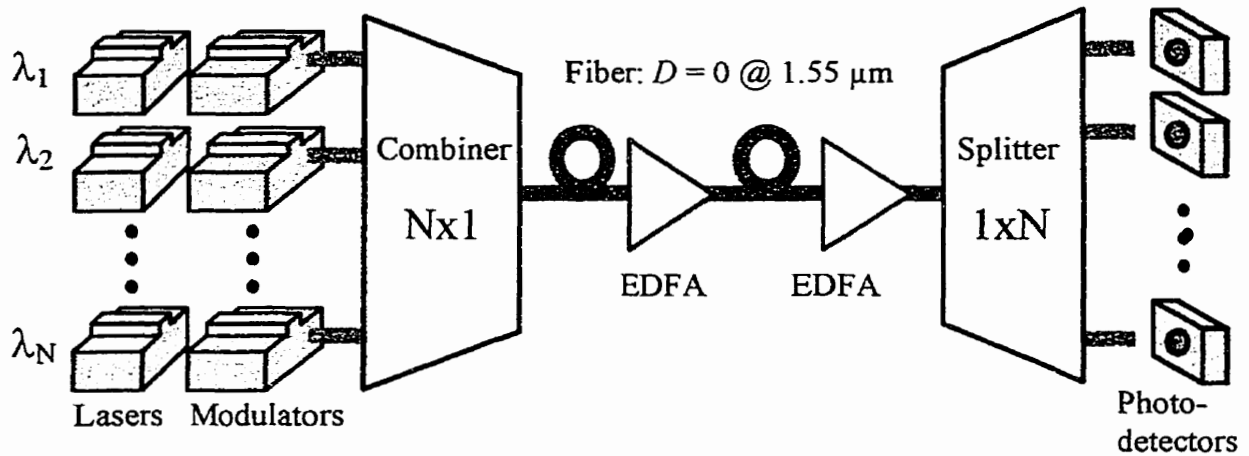
Fig. 1.1 – **Modern Optical Fiber Telecommunication Link**

1.1. Use of Optoelectronic Components in Optical Fiber Communication Systems

In a traditional optical fiber link, the light source is usually a laser diode, and intensity modulation is achieved through direct laser current modulation. Light is guided through a standard, non-dispersion-shifted single-mode fiber. On the other side of the fiber, a photodetector converts the optical signal back into electrical current; it is usually a simple p-i-n photodiode or an avalanche photodiode. The maximum data rate and distance achieved with this scheme are typically 2.5 Gbit/s over 100 km.

In recent years, new devices have been developed, such as the Erbium-Doped Fiber Amplifier (EDFA), optical modulators and optical wavelength combiners and splitters, which revolutionized optical fiber communications. The advent of the EDFA reduced the use of expensive repeaters to regenerate optical signals, and increased the reach of transmitters at a low cost. Another innovation is Wavelength-Division Multiplexing (WDM), where multiple optical signals at closely spaced wavelengths are injected and carried in one single fiber. The main advantage of WDM is that one single EDFA placed in series with the fiber can amplify all channels simultaneously, since the gain in the EDFA covers a relatively large spectrum, typically from 1525 to 1565 nm [2]. It is

now possible to increase enormously the capacity of transmission of already laid fiber by upgrading conventional systems to WDM. Actual commercial systems now possess typically up to 16 channels at 2.5 or 10 Gbit/s each. New high-performance systems also use dispersion-shifted fibers, where the core structure has been modified so that the zero of dispersion is moved from 1.3 μm to 1.55 μm. Dispersion is no longer a limitation in this case, and with EDFA, the transmission distance is virtually limitless. The industry is looking forward to increase the number of channels to up to 128 or more in a near future, with transmission rates eventually up to 40 Gbit/s per channel.

Figure 1.1 shows what a modern fiber link looks like. On the transmitter side, a set of laser diodes are DC-biased, all emitting light at slightly different but very stable wavelengths. Intensity modulation is achieved by high-speed optical modulators, which are capable of faster switching than lasers. The modulators also resolve the problem of the laser **chirp**: the wavelength of emission of a laser diode changes with the drive current, because of the varying carrier density in the active region. This is the cause of problems when the laser current is modulated at high frequencies. The optical signals are then injected in a single dispersion-shifted fiber. Approximately every hundred of kilometers, an EDFA amplifies the signal. On the receiver side, a wavelength splitter separates the channels, each one being sent to a distinct high-bandwidth *p-i-n* photodiode.

Many optoelectronic components exist in this system. The laser diodes, modulators and photodetectors all rely on III-V semiconductors, most often of the $In_{1-x}Ga_xAs_yP_{1-y}$ system, to create a bridge between light and electricity. Both the laser and the modulator are waveguide devices. The main advantage of a waveguide configuration is the increased efficiency over bulk devices, since electro-optic effects are confined to a smaller region; the electrical capacitance associated with such devices can also be considerably smaller, allowing faster operation. Eventually, photodetectors could also be made in waveguides to achieve ultra-high speed operation. Aside from these components, many novel optoelectronic devices are entering the market. Among them are integrated cou-

plers, optical cross-point switches and semiconductor-based wavelength combiners and splitters that are expected to replace the ones made of fibers and filters.

1.2. Effect of Temperature

Temperature has a strong influence on optoelectronic devices, mostly because it affects the band gap of the semiconductor material. This can have various consequences, depending on which device is considered. In laser diodes, the heat generated by the passage of current modifies the internal efficiency and the wavelength of emission, which can have adverse consequences in WDM systems. In active but non-light-emitting devices, such as optical modulators and switches, the heating is usually the result of the absorption of light or of the passage of current. For example, in an electro-absorption modulator, a photocurrent is generated when light is absorbed, which heats up the active region of the device. High temperature has two kinds of effects. First, it can significantly affect the operation of the device, since most electrical and optical properties of a semiconductor, such as the absorption coefficient and the refractive index, change with temperature. This will modify the operation characteristics of the device, such as the propagation loss in the waveguide or the switching voltage of a modulator. There is also a possibility of an accelerated aging of the device, which could reduce its service life. The specification for the service life of any optoelectronic component is most often in excess of 20 years, making them very sensitive to aging issues.

One way of testing the reliability of optoelectronic devices is to observe the degradation they suffer when they are submitted to high temperature (100 – 200°C) and optical and electrical stresses for long periods of time. From these high-stress tests, it is possible to verify that the devices are not subject to premature degradation or failure. To fully understand the significance of the results of these tests, it is essential to understand how temperature affects the device, and also to know exactly the internal temperature during the test. Thus, thermal issues are deeply involved in reliability testing, providing one more argument for the importance of this study.

1.3. Methods of Temperature Evaluation

A large part of this study has been devoted to the development of methods of evaluating the temperature inside a waveguide device under different conditions of operation. One way to proceed is to construct a thermal model of the device. However, an experimental technique is also needed to validate the model predictions. What is needed is a technique that can directly measure the temperature in waveguide devices while light is injected into the waveguide and electrical contact is established with a voltage source. Methods of temperature evaluation have been already developed for microelectronic integrated circuits; the situation in optoelectronic devices is more complicated, because of the need to inject light into the waveguide. The requirements for the technique are as follows:

* Low cost;

* Versatility, or the potential to be used on different optoelectronic devices (lasers, modulators, optical switches, etc);

* High spatial resolution, in the order of 1 μm, as the waveguide width is usually around 2 μm;

* Good temperature resolution, 1°C or better;

* No requirement for complicated sample preparation;

* Possibility of bringing electrical probes and tapered fibers (for light injection) close to the device.

However, a literature review of all the techniques available for direct temperature measurements on this kind of device shows that most of them are not suitable for the task exposed here. The following is a list of the most frequent techniques mentioned in the literature, and why they can not be used in this case:

* *Infrared Microscopy*: this technique is relatively simple and not very expensive; the black-body thermal radiation emitted by the sample surface is measured to produce a temperature map of the device [3,4]. Infrared microscopy does not work very well on reflective metal surfaces, which is a problem in the case of waveguide devices, which are usually covered by gold electrodes. The spatial resolution is also a problem; the best resolution reported is 5-10 μm, due to the long wavelengths used, which is insufficient for the needs of this study.

* *Photoluminescence (PL) Peak*: one can deduce the temperature of a semiconductor material by looking at the wavelength corresponding to the peak intensity of the PL [5]. The PL peak wavelength gives, in a first approximation, the band gap of the semiconductor, which varies with temperature. Once this dependence is known, the internal temperature can be found accurately. To obtain the temperature in the active region of a device employing multiple quantum wells, one has to look at the PL associated with the wells. The spatial resolution of this technique is sufficient; however, it can not be used because the gold electrodes that cover the waveguide and the backside of the chip prevent light from reaching the active region or coming out of it through the device surface. Since the top electrode must be kept in place for electro-optic effects to take place, it would be necessary to etch windows in the backside electrode. This is a very complicated process, incompatible with the basic requirement for little sample preparation and versatility of the technique.

* *Photoreflectance Measurements*: in a laser diode, it is possible to measure the temperature at the facet by looking at the change in reflectance on the semiconductor surface with an optical probe [6]. This technique can not be used on the waveguide devices used for this work, where the exposed facets lie far from the hot region. Even if the device were cleaved in such a way that the facets would be near the hot region, the change in geometry would certainly alter the temperature profile.

* *Raman Spectroscopy*: the Raman spectrum can also give information about the temperature of a semiconductor material [6,7]. However, this technique also requires an exposed hot surface of semiconductor material, and is not suited for this task.

One method that can be utilized successfully for the present task is the *Liquid Crystal Technique*, used extensively on integrated circuits. Although it can only measure the surface temperature of the chip, that is, on the gold electrode covering the waveguide, it is a simple, low-cost technique that can be easily adapted to study a wide range of devices. It also requires a minimum of sample preparation. The spatial resolution of the technique is determined by the microscope used to observe the sample, and is less than one micron. The temperature resolution also compares advantageously to that of other techniques. The liquid-crystal technique will be described in detail in chapter 2.

1.4. Description of the Waveguide Devices

The experiments described in this document have been carried out on one type of device. It is a ridge waveguide device, covered by a gold electrode. By applying a voltage to the device, electro-optic effects are induced, which change the refractive index and the absorption coefficient in the waveguide. The device could serve as a modulator for example, using either electro-absorption or electro-refraction to achieve intensity or phase modulation. Figure 1.2 shows the cross-section of the ridge and the material composition. The semiconductor structure is grown in a MOCVD reactor on an n-doped InP wafer. The active region, which also acts as the guiding layer, is composed of 20 undoped InGaAsP quantum wells. An InGaAs layer has been placed under the active layer to absorb the stray light that could escape the guiding layer, while another one on top of the ridge serves as a cap layer to ensure good electrical contact with the gold electrode covering the waveguide. The ridge is about 2 μm wide and 3 μm high, and comprises the multiple quantum wells (MQW); this structure acts as a single-mode waveguide. The sides of the ridge are covered with PECVD-grown SiO_2 and SiN_x. Two
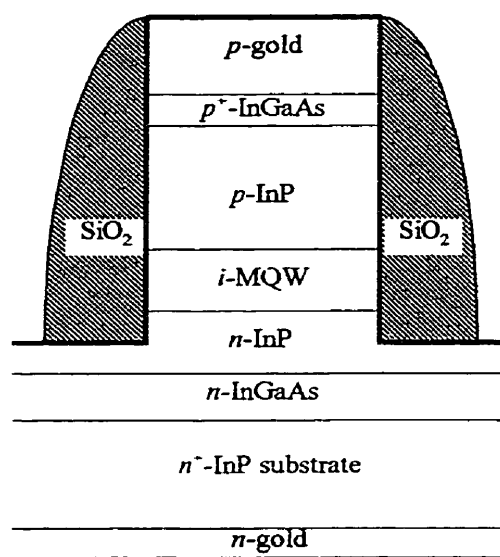
Fig. 1.2 — **Cross-Section of the Waveguide Device**
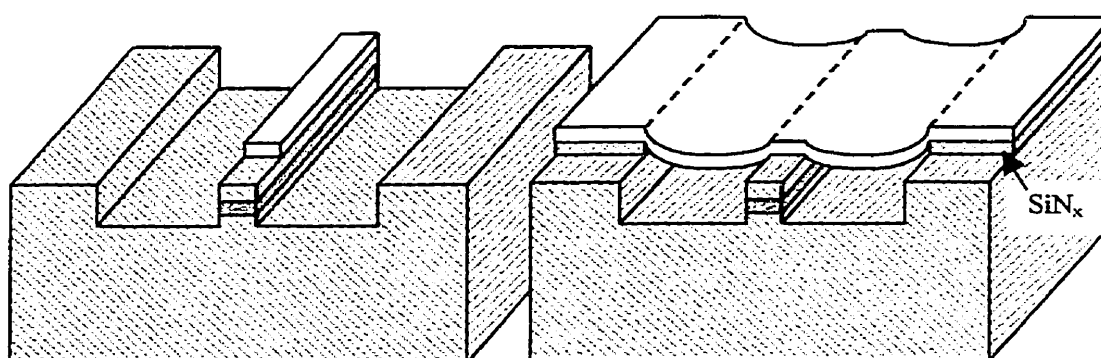
Fig. 1.3 — **Narrow-Electrode (left) and Large-Pad (right) Devices**

different geometries exist for the electrode covering the ridge, as shown in figure 1.3. The first is a large rectangular electrode, 220 μm-long (in the direction of the ridge) by 200 μm-wide, with air bridges connecting the section covering the ridge to the surrounding pad. The second type of electrode used is narrow and 600 μm-long, and covers only the ridge itself. The purpose of the two designs will be explained shortly. The gold electrode rests on two thin layers of platinum and titanium that act as an adhesion layer and a diffusion barrier respectively. The backside of the chip is entirely covered by a NiGeAu electrode for n-side electrical contact.
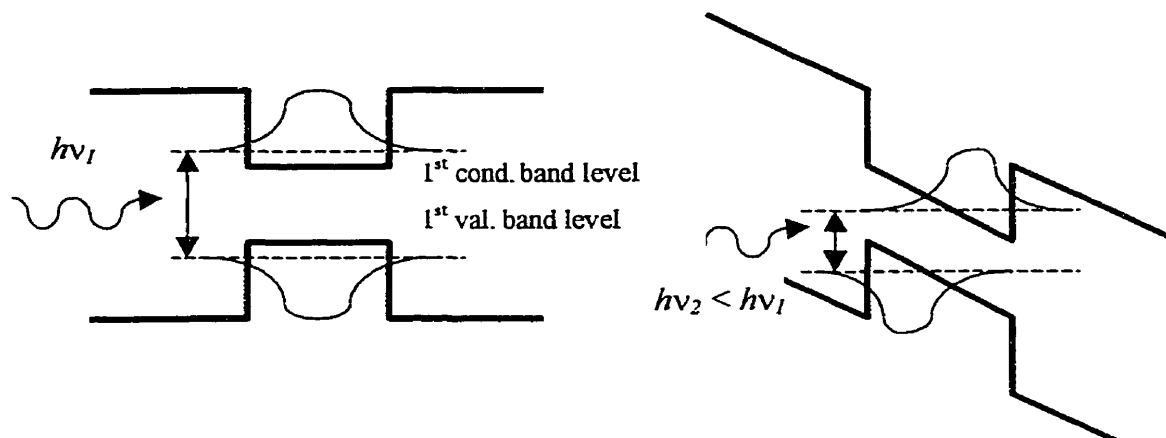
Fig. 1.4 – Explanation of the Quantum-Confined Stark Effect
Left: E = 0; Right: E ≠ 0

The doping in the semiconductor layers forms a *p-i-n* junction within the ridge; when the junction is reverse-biased by grounding the *n*-side electrode and applying a negative voltage to the top, *p*-side electrode, a perpendicular electric field appears across the quantum wells. Because of the quantum-confined Stark effect (QCSE), the electric field modifies the effective band gap in the wells, which results in changes in the refractive index and the absorption coefficient in the waveguide. The QCSE is briefly explained by figure 1.4: the presence of an electric field bends the conduction and valence bands, which reduces the effective band gap. When a photon is absorbed, it generates a hole – electron pair, both rapidly swept away by the electric field. The current generated by this process is called the **photocurrent**. It is the passage of this current, more than just the absorption of light, that heats up the active region.

The device can fulfill two functions. With a large enough voltage, all the light can be absorbed over the length of the electrode, and the device can serve as an electro-absorption modulator. If only a moderate voltage is applied, the absorption is small but the refractive index still changes sufficiently so that the device can be used as a phase modulator or, when placed in a Mach-Zehnder interferometer, as an intensity modulator. For high-speed modulation, the long and narrow electrode design must be used, because its long length maximizes the net electro-optic effect. In contrast, a large rectangular
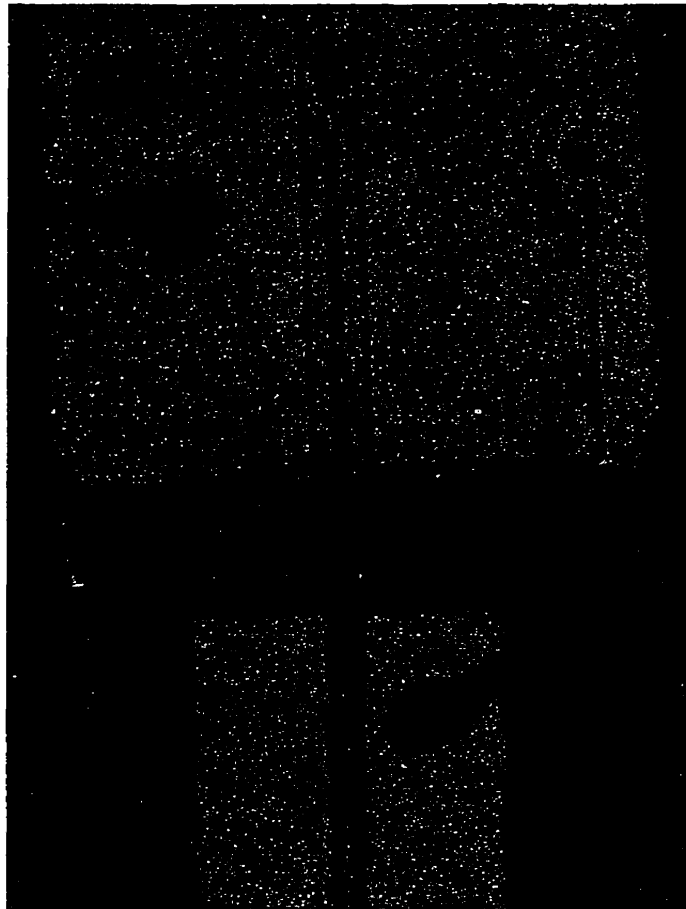
Fig. 1.5 – The Hybrid Device

pad is better suited for dissipating the large amount of heat produced when light is absorbed, and is capable of sustaining high voltage and photocurrent without damage. However, the large area results in a large electrical capacitance, incompatible with high-speed modulation, and the device would better serve as a D.C. variable attenuator for large optical signals.

For certain experiments, it is useful to have a light source adjacent to the waveguide device, to remove the need for an external light source and the troublesome operation of using a lens assembly or a tapered fiber to couple the light into the waveguide. A laser diode can be attached to the waveguide device for that intent. These so-called hybrid devices are built by approaching the laser and the waveguide device so that the two facets touch each other, and gluing the devices together with transparent epoxy. The

result can be observed in the picture shown in figure 1.5, where the laser is seen on top and the waveguide device on the bottom, with the large gold pad clearly visible. The whole operation is time-consuming, so this kind of device is used only when having an external light source is impractical. Otherwise, when the waveguide device stands alone, it is referred to as a **discrete** device.

All the samples were glued to aluminum nitride (AlN) chip **carriers**, to facilitate the handling of the small and fragile chips. The carriers are small rectangular pieces of ceramic, roughly 9 x 6 x 1 mm. The chips are glued to the carriers using either a gold-tin soldering alloy (for discrete devices) or a silver-based, electrically conducting epoxy (for hybrid devices). The latter is more stable at high temperatures, and reduces the risk of cracking of the butt-joint during high-temperature tests. The device contact pads are connected to large gold contact pads on the carriers with fine gold wires, making the electrical connections to the device easy to establish. The metal electrodes are exposed to air.

Chapter 2
Liquid-Crystal Temperature Measurements

The liquid crystal (LC) technique has been selected as the method of choice for measuring the temperature on the surface of optoelectronic devices because of its simplicity, low cost, versatility and good spatial and temperature resolutions. In this chapter, the general properties of LC are reviewed and the technique itself and the setup are described in detail. Finally, a collection of the most significant results is presented and discussed.

2.1. Properties of Liquid Crystals

All LC share one property: the molecules composing them have an ellipsoidal geometry. Along the major axis, electronic properties such as polarizability are different, causing the LC to be anisotropic. The arrangement of the molecules with respect to each other is responsible for the peculiar optical properties of the LC. Many physical phases exist in a LC, each corresponding to a different molecular arrangement:

- The **solid phase**: all molecules are oriented along a common axis and their positions are fixed and follow a regular ordering;

- The **smectic phase**: all molecules are oriented along a common axis, and are arranged in planes; however, their positions within each plane are random;

- The **cholesteric phase**: similar to the smectic phase, but the orientation of the molecules changes slightly from plane to plane, following a helical pattern;

Smectic   Cholesteric   Nematic   True-liquid
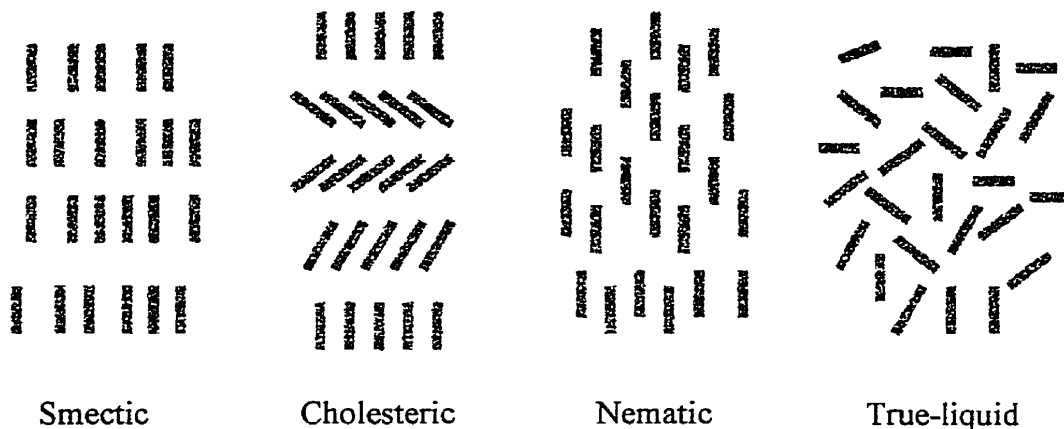
Fig. 2.1 – **Liquid Crystal Phases**

- The **nematic phase**: all molecules are oriented along a common axis, but their positions are completely random;

- The **isotropic phase** (true liquid): the molecules' positions and orientations are both random.

It is possible that a given LC may not exist in all of these phases. The arrangement the LC molecules adopt is usually determined by temperature. The temperature at which the transition from one phase to another takes place can be known very accurately. It was reported that the transition occurs over a very short range of temperature, as small as 1 mK [8].

In all except the isotropic phase, the anisotropy of the LC induces birefringence. In the cholesteric phase, the LC also exhibits optical activity (rotation of the plane of polarization as light travels in the medium). It is important to note that the long-distance ordering of the LC molecules is limited to small domains, and that within each domain all molecules are aligned along the same direction. The light is scattered at the interface between the domains, conferring a translucent milk-like appearance to the LC. When the temperature is increased so that the LC enters its isotropic phase, these domains cease to exist and the liquid becomes clear: for this reason, the transition temperature between the nematic and the isotropic phases is called the **clearing point** of the LC.

2.2. Technique

LC's have been used for more than thirty years to perform thermal investigations in semiconductor devices, mainly in microelectronic integrated circuits (IC) [3,8-13]. The main role of the LC technique is usually to locate failures in IC, such as shorts, which generate a large amount of heat; there are also reports of its use for temperature mapping of IC and Micro-Electro-Mechanical Systems (MEMS) [9]. To the author's best knowledge, no one has reported any work involving the use of the LC technique for thermal investigations on optoelectronic devices.

The technique developed for the purpose of this work uses the transition from the nematic to the isotropic phase of the LC to measure the temperature on the surface of an optoelectronic chip. A thin layer of LC is first deposited on the surface of the device, which is subsequently connected to a voltage source, with light injected into the waveguide. The transition in the LC can be observed with a microscope containing two crossed polarizing filters (that is, with their transmission axis forming a 90° angle). In the microscope, the background appears dark, whereas the areas of the device covered with LC is bright, since the LC, birefringent in its nematic phase, changes the polarization of light. As the device heats up during normal operation, it is possible that the temperature on some areas of the device surface exceeds the clearing point, so that the LC locally reverts to its isotropic phase. A dark spot can then be seen in the microscope, since the polarization of the light reflected on the device surface is not affected by the isotropic LC. If the operating conditions are adjusted so that the dark spot is reduced in dimension to the point where it almost vanishes, the peak temperature on the surface of the chip is known to be exactly the clearing point of the LC.

Obtaining a thin film of LC of uniform thickness on a chip is not a trivial task. Some authors report the use of wetting agents, such as lecithin in pentane [11] or Freon-TF [13], others put a thin plane glaze on top of the LC-covered chip [9]. Another possibility is simply to heat the LC past its clearing point, as it is less viscous in its true liquid form,
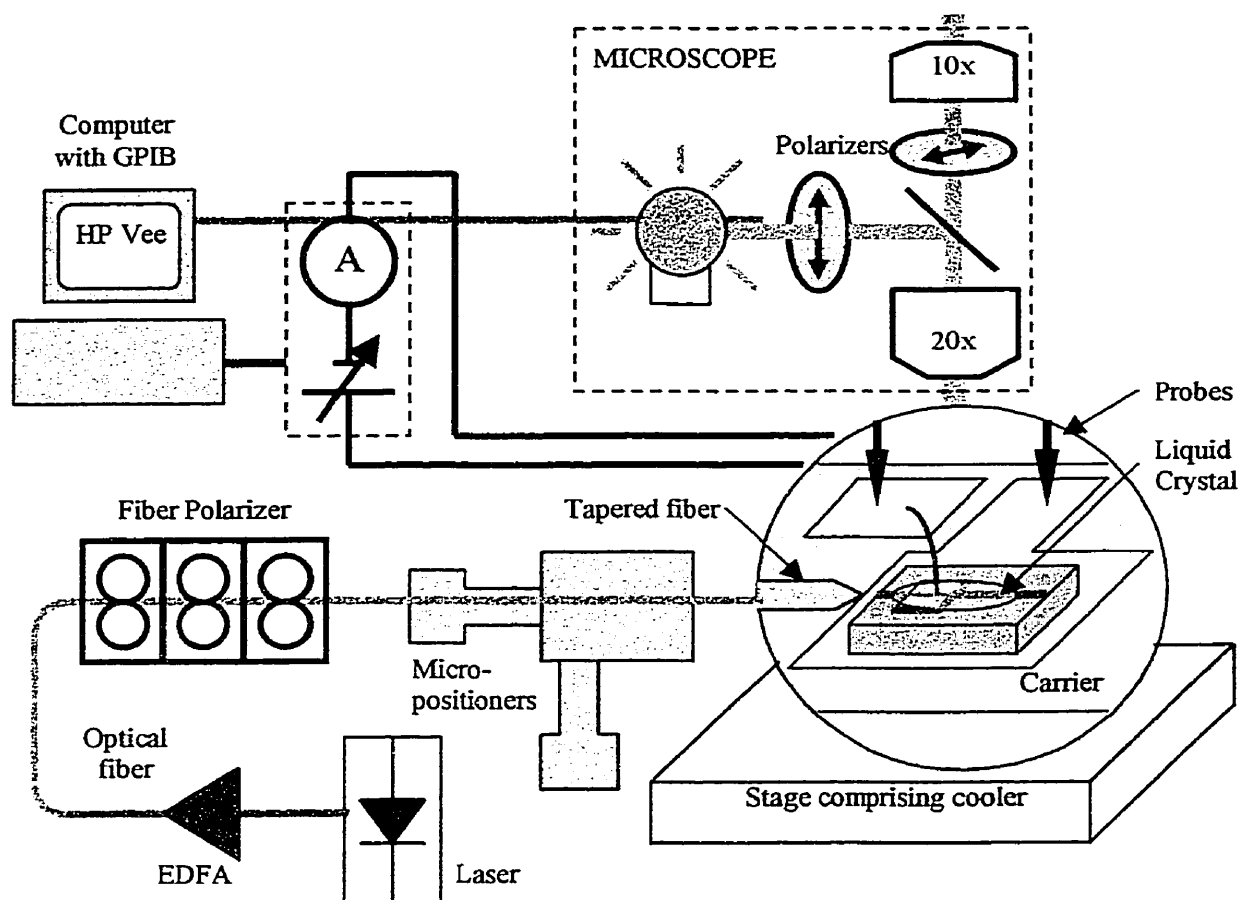
Fig 2.2 – Setup Used for Liquid-Crystal Measurements

and it spreads more easily on the sample [3]. The latter procedure has been retained. A discussion of the efficiency of this method follows in a subsequent section.

The technique can be used in a variety of ways. Even if only one LC mixture is available, there is a multitude of ensembles of conditions (voltage, optical power, photocurrent, stage temperature) for which the peak temperature on the device corresponds to the LC clearing point. In optoelectronic devices, however, the electro-optic properties are strongly affected by temperature, and it is desirable to maintain the stage temperature constant. For the purpose of this work, the stage temperature was maintained at 25 or 30°C, while large ranges of voltage and optical power (which, together, determine a unique photocurrent) were investigated. To extend the temperature range that can be

researched, three LC mixtures were used, with clearing points of approximately 42°C, 58°C and 73°C; the information concerning the LC is located in appendix A.

2.3. Description of Setup

Figure 2.2 depicts the setup used for the LC measurements. At the center of this setup is a twin-eyepiece microscope with long-distance objectives (total magnification: 100x or 200x). This microscope contains a lamp, next to which was placed a polarizing filter; a second filter is located in the right eyepiece. Under the objective, the sample sits on a small aluminum plate, which is glued to a thermo-electric cooler (TEC) that uses the Peltier effect to heat or cool the sample. A thermistor attached to the top of the TEC provides feedback to the TEC driver. A set of spring-loaded probes can be lowered on the sample carrier to establish electrical contact. The electrical equipment includes a digital multimeter (used as an ammeter), a dual variable power supply and a laser diode controller (combining the TEC driver and a precision current source). The optical equipment comprises a laser diode emitting at 1556 nm, an EDFA, a paddle-type fiber polarizer and an optical power meter, all connected with standard single-mode fiber. Light is injected into the waveguide through a tapered fiber (with a conical tip), since it is impossible to use lenses due to the fact that the devices are located in the center of relatively large carriers. The fine alignment of the tapered fibers is achieved with electro-striction actuators. The entire setup is located on a pneumatic optical table. Finally, a computer controls the whole station through a GPIB bus, with the aid of the software *HPVee*. A more detailed description of the equipment can be found in appendix B.

2.4. Methodology

The block diagram in figure 2.3 shows the entire procedure followed during the LC temperature measurements.

LC MEASUREMENTS

SETUP PREPARATION

Clean sample :
- 30 s Acetone
- 30 s Propanol

Adjust polarization to get TE mode

- Select one of three LC :
  Clearing points : **42, 58, 73°C**
- Apply LC on device

Measure exact clearing point of last LC (~74°C)

- Place sample on stage
- Contact probes

LEGEND :

☐ Regular Operation

▱ Loop

▣ Computer Operation

- Heat stage up to clearing point of LC
- Record clearing point
- Set stage temperature at **30°C**

Align tapered fiber for light injection (for discrete devices)

Set voltage at **9 → 5 V; 0.5 V** steps

Increase optical power to observe a dark spot on the waveguide

- Clean the sample again
- Repeat with a different LC

Measure photocurrent and record all information in file

Fig. 2.3 – **Block Diagram Describing the Liquid-Crystal Measurement Procedure**

Prior to the deposition of the LC on the device surface, the samples are cleaned successively with room-temperature acetone and iso-propanol. To put LC on the samples, a droplet of LC is first "attached" to a hook-shaped probe tip from a syringe; the probe is then lowered on the sample until the drop spreads on its surface. The high surface tension of the LC is usually great enough to hold it to the top surface of the sample. It is often necessary to remove the excess LC with a piece of cleaning paper ("Kim Wipes") rolled into a fine tip, so that only a thin layer of LC remains on the chip. With this procedure, a thin film of LC can be obtained, with a thickness not exceeding 5 μm, as was verified with a high-resolution microscope.

The LC-covered sample is then placed under the microscope, and the electrical probes are put in contact with the carrier pads. To measure the clearing point of the LC, the TEC temperature is raised up to the point where the whole chip turns black because of the transition of the LC from the nematic to isotropic phase. The clearing point, taken to be the temperature when the first changes are seen in the LC, is recorded. This procedure helps spreading the LC to get a uniform film, since the viscosity is much reduced in the isotropic phase. The stage is then cooled down back to the temperature selected for the measurements.

When an external light source is needed, the next step is to adjust the polarization to have the light coupled into the TE mode of the waveguide. The fiber is placed in front of a large-area photodetector covered by a polarizing filter, with its transmission axis vertical, and the polarizing paddles are moved to a position giving maximum extinction. Horizontal polarization, corresponding to the TE mode of the waveguide, is then achieved. The tapered fiber is then brought near the device facet and aligned with the micropositioners. The best alignment is found by maximizing the photocurrent, at a given voltage, in the waveguide device.

A practical way of conducting these experiments is to have the computer take charge of the electrical equipment and data collection, leaving to the operator the single task of

looking at the sample in the microscope and observing the transition in the LC. The *HPVee* program written for this purpose sets the voltage applied to the waveguide electrode at values from 9 to 5 V, with a 0.5 V interval. The operator increases the laser current (in hybrid devices) or the EDFA current (for discrete devices) until a dark spot appears on the ridge. The hot spot is always located near the front edge of the electrode covering the waveguide, where the light enters and where the optical power is the greatest. The operator then "activates" the computer program, which measures the photocurrent, the laser or EDFA current, and the exact temperature of the cooler; it then sets the voltage to its next value. All data is written to a file, along with general information on the device under test (wafer designation, device identification, etc.). The fact that the measurements are taken over a period of time of several seconds ensures that the steady-state temperature is measured; no transient can be observed with this technique.

The samples are removed from the stage and cleaned again and the entire procedure is repeated for every LC mixture available for the measurements. To check the adequacy of the cleaning procedure mentioned above, cleaned samples were observed through the microscope, to confirm the absence of any trace of LC. One change to the procedure is that for the highest clearing point LC, it is impossible to measure the clearing point in the manner explained above, because the TEC can not reach temperatures over 70°C. The clearing point of that LC was measured on a hot plate at the beginning of each day of experimentation, and the temperature at which the clearing point was found was recorded and used for all subsequent measurements.

2.5. Results

Figure 2.4 is a set of photos showing the dark spot as seen in the microscope. Photo A shows the large-pad device covered with LC with no external bias on the pad; for photos B to D, a voltage of 7.0 V was applied, and the optical power was increased progressively. The dark spot clearly extends as the power increases, meaning that the region where the temperature exceeds the LC clearing point grows bigger.
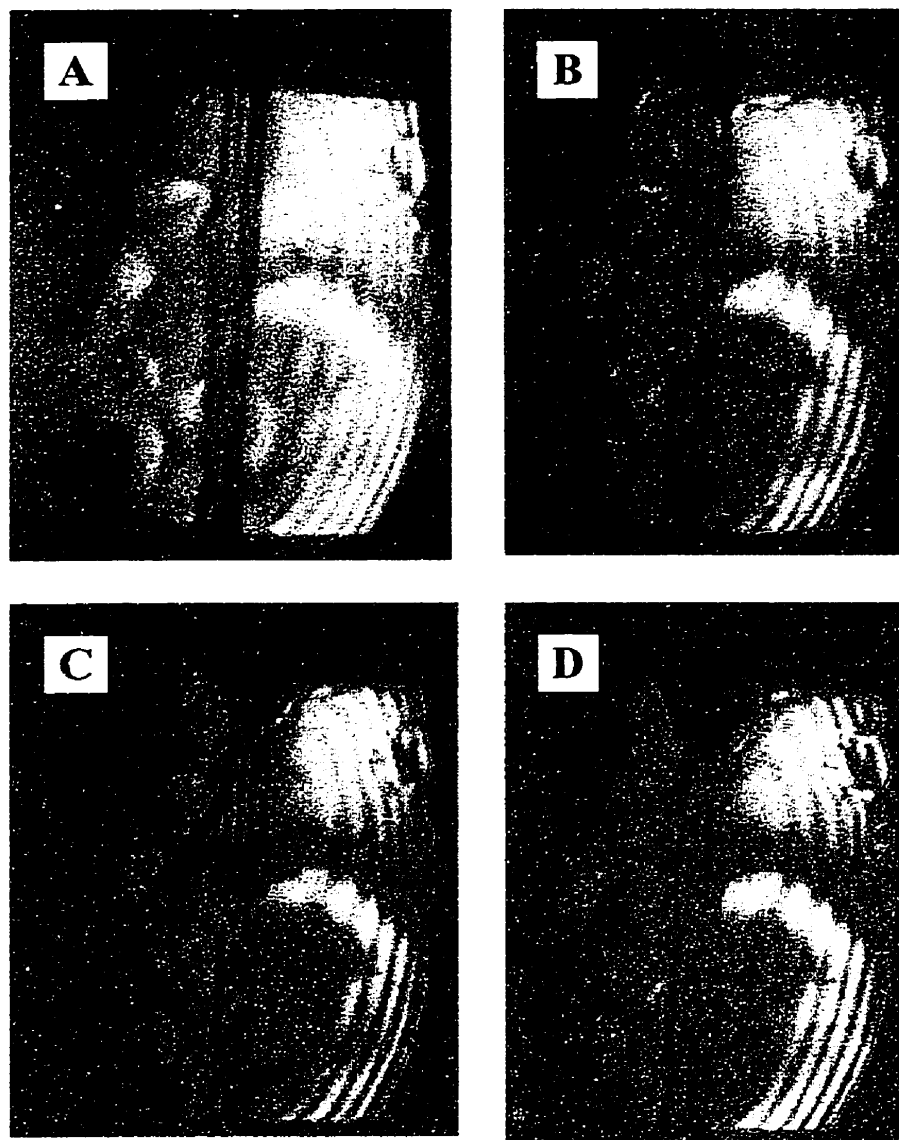
Figure 2.4 – Temperature Measurements using Liquid Crystals
These photographs show a large pad covered with liquid crystal; in (A), no bias is applied,
while in (B), (C) and (D), the device was biased at 7.0 V, with increasing optical powers.
Light enters from the top. The dark spot is seen at the top edge of the pad.

Two sets of results are shown here: the first set was obtained on the large pads of hybrid
and discrete devices, all originating from the same wafer, designated R2-1444. The
quantum wells on that wafer are designed for operation at a wavelength of 1544 nm,
requiring the use of a tunable laser with the discrete devices, because the available laser
only emits at 1556 nm. Otherwise, the lasers present in hybrid devices were selected to
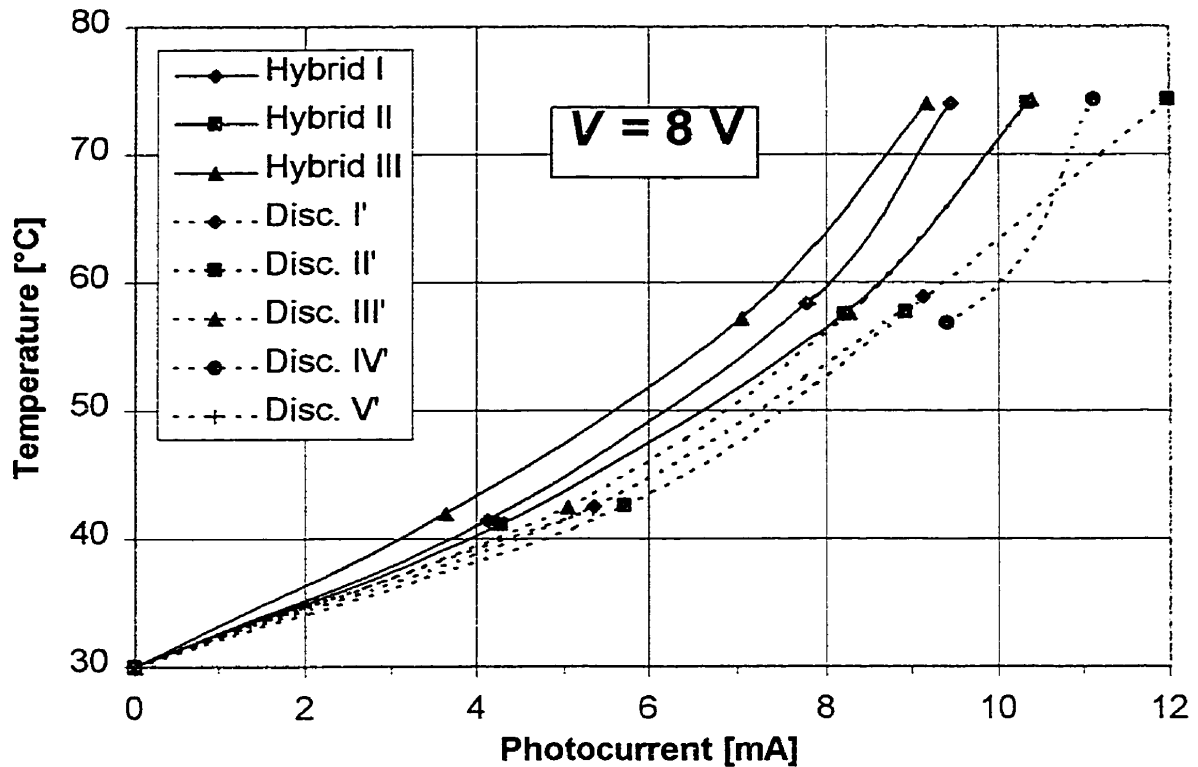
Fig. 2.5 – Liquid-Crystal Measurements on Large-Area Pads, at 8 V

emit at this wavelength. A second series of experiments was realized on narrow-electrode devices, coming from nine different wafers. The primary goal of these experiments is to compare how the temperature corresponding to given conditions of operation varies from wafer to wafer.

The numerical results of all the temperature measurements presented in this chapter are given in appendix C.

2.5.1. Large-Pads Devices

The results of the liquid-crystal measurements are presented in graphs that show the peak temperature on the surface of the device as a function of photocurrent, with separate curves corresponding to different voltages. Measurements were carried out on large pads on 5 discrete and 3 hybrid devices; the missing points are the results of measure-
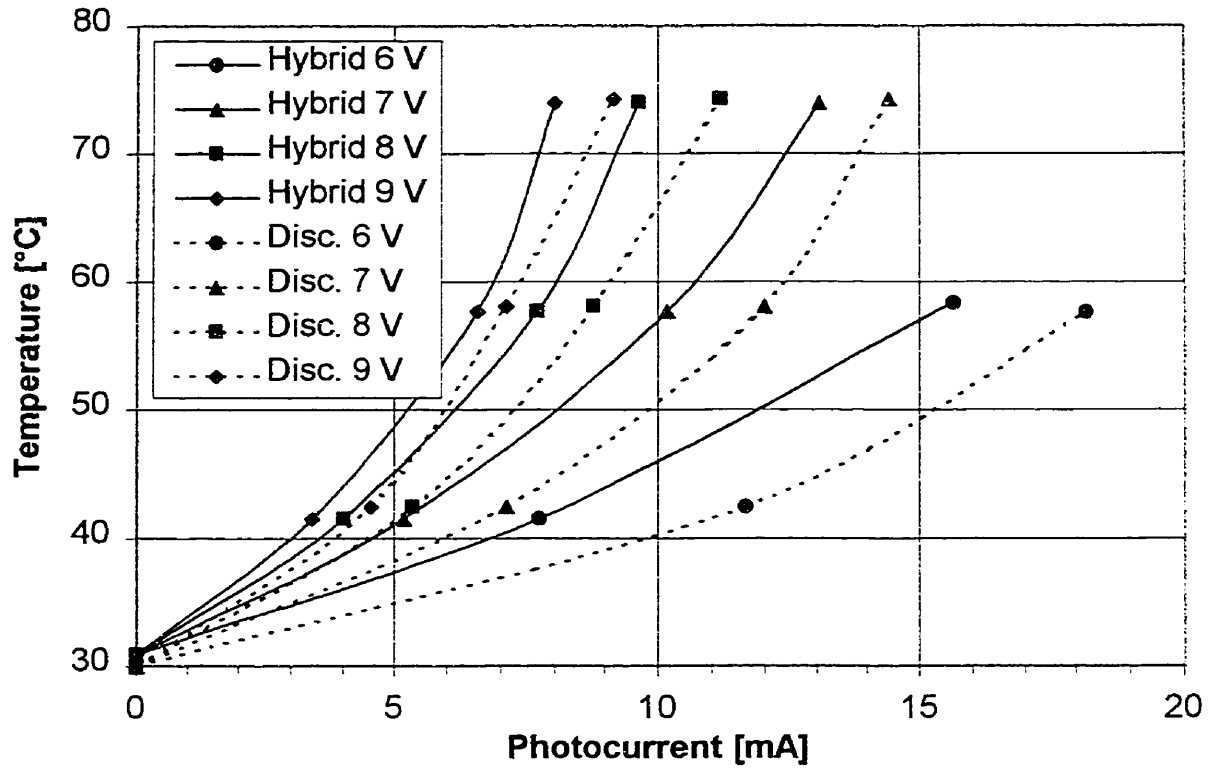
Fig. 2.6 – **Averaged Liquid-Crystal Measurements on Large-Area Pads**
This graph shows the average of results obtained from several devices originating from the same wafer.

ments that were later found to be incorrect. Figure 2.5 shows the data obtained on all devices at 8 V.

Since the results obtained on all devices of the same type (hybrid or discrete) are similar, it is convenient to present only the average of the measurements. Figure 2.6 shows the average temperature rise as a function of photocurrent at all voltages.

2.5.2. Narrow-Electrode Covered Waveguide

The temperature rise was also measured on narrow-electrode discrete devices on two samples coming from each wafer of a set of nine. The laser wavelength was always 1556 nm, except for R2-1510 (1547 nm) and R2-1444 (1538 nm), which had a different quantum well composition. Figure 2.7 shows all the results obtained at 8 V from only
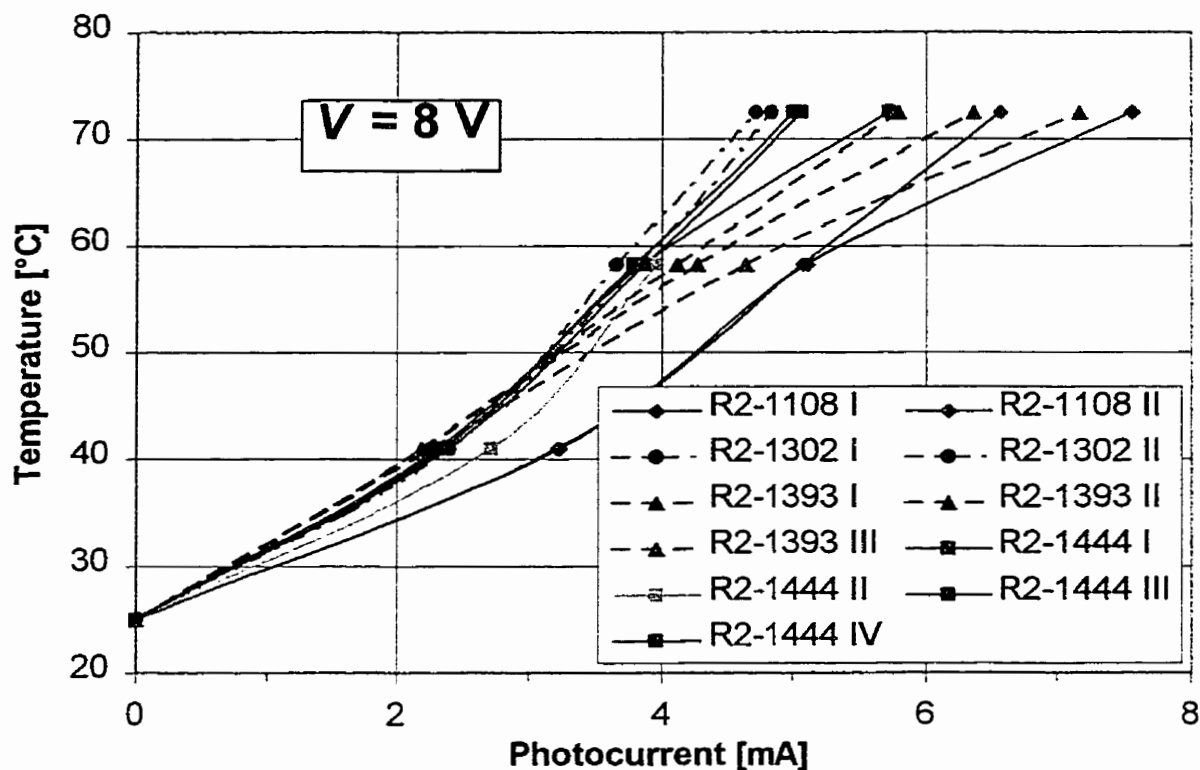
Fig. 2.7 – **Liquid-Crystal Measurements on Narrow-Electrode Devices, at 8 V**

four wafers, to prevent from overcrowding the graph. It can be seen that the behavior of the two devices coming from the same wafer is most often similar; the temperature rise can then be averaged on the devices coming from the same wafer. The results are presented in figures 2.8 (at 9 V) and 2.9 (at 7 V), which provide a good overview of the entire data. Note that at low voltages (down from 7 V), there are missing data points because the maximum optical power delivered by the combined laser and EDFA is not sufficient for the temperature on the device to reach the clearing point of the last LC.

2.6. Problems with the LC Technique

The LC technique is simple, inexpensive and possesses good spatial and temperature resolution. One important problem has been encountered however: it is difficult to obtain a thin and uniform LC layer on a sample. This problem is accentuated by the
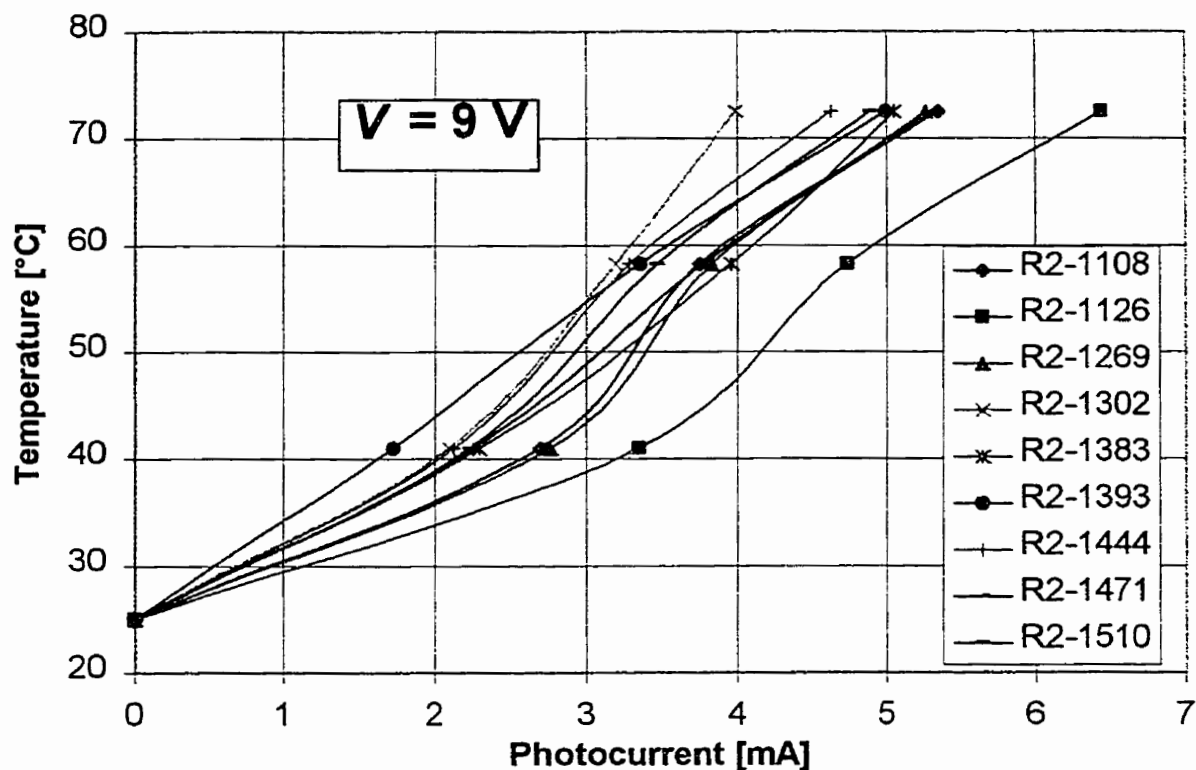
Fig. 2.8 – Averaged Liquid-Crystal Measurements on Narrow-Electrode Devices, at 9 V
The results of the measurements performed on devices coming from the same wafer were
regrouped and averaged to give one single curve per wafer on this graph.

presence on the device of a complex topography, including a ridge, trenches and gold wires. The LC must be kept thin, otherwise the measurements will be inaccurate because the temperature could then differ significantly from the bottom to the top of the LC layer. Note that the LC is a mixture of organic liquids that are not good heat conductors. When a thin layer of LC is deposited on the sample surface, the LC usually moves up the gold wires, and sometimes retracts from the top of the ridge. Heating the stage past the clearing point of the LC, as mentioned in reference 3, is of no help when this happens. Wetting agents have not been retained as a solution, because of the requirement for uncommon and potentially toxic chemicals, which can also alter the characteristics of the LC, even when used in small amount [8]. This situation does not happen with microelectronic IC, which usually have a more planar surface.
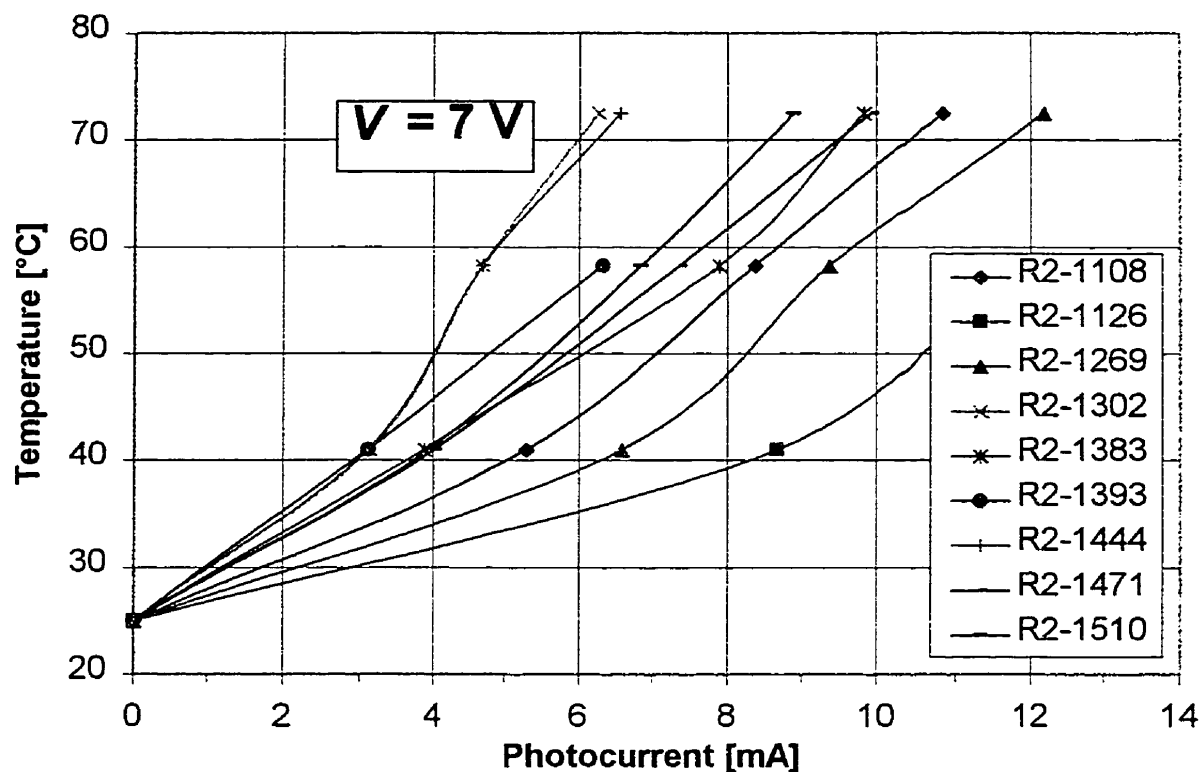
Fig. 2.9 – Averaged Liquid-Crystal Measurements on Narrow-Electrode Devices, at 7 V
The results of the measurements performed on devices coming from the same wafer were regrouped
and averaged to give one single curve per wafer on this graph.

It is nonetheless possible to obtain good results with the technique despite the problems mentioned in this section, but it requires applying the exact amount of liquid needed on the device, removing the excess with a piece of cleaning paper when necessary. In some cases, it is necessary to clean the sample and to repeat the whole operation again before a satisfactory LC coating is obtained. Unfortunately, this requires an extensive "training" of a new operator before accurate and reproducible results can be obtained with the LC technique. Further investigations have not provided a way to definitely solve this problem.

2.7. Discussion

The precision of the measured temperature is estimated to be 1°C. The thermo-electric cooler can maintain a temperature within 0.1°C of the set value, however, it is impossible to measure the clearing point of the LC with such a precision. Simultaneously, the error made when measuring the photocurrent is estimated to be 0.1 mA, due to the difficulty associated with observing the LC transition on the sample. In particularly bad cases, when the contrast is unusually poor and because of the problems mentioned in the previous section, the uncertainty on the measurement could increase, possibly up to as much as 0.5 mA.

The graph in figure 2.6 gives a good overview of the how temperature rises in the waveguide device. As the voltage and photocurrent increase, the temperature increases in a super-linear fashion. Voltage has the greatest effect on the temperature, since it determines absorption (see chapter 4) and also has a direct influence on the total heat generated in the MQW layer (the latter is given by the $I \times V$ product). The upward curvature of the temperature curves is explained by the fact that as temperature rises, absorption in the waveguide increases so that the heating is also more localized, which results in an additional rise in temperature. This graph also shows another crucial result: the temperature increases faster with photocurrent on hybrid devices than on discrete devices. This happens because the heat generated in the laser is conducted along the ridge to the waveguide device, thereby raising the internal temperature. This increases the absorption occurring in the waveguide and raises the temperature even further. This constitutes a clear demonstration of a thermal cross-talk between two optoelectronic devices, where the heat produced by one device affects the operation of another neighboring device. This is of major importance for the optoelectronic industry, which is looking forward to integrate multiple devices on a common substrate; in this context, thermal cross-talk issues are expected to arise more frequently.

On figure 2.7, it can be seen that the temperature measured on the two devices coming from the same wafer is similar, and that places much confidence in the validity and the

reproducibility of the measurements. In some cases, such as for the two samples from wafer R2-1108, the 73°C points differ, probably because of an erroneous measurement (one possible cause being a poor uniformity of the LC film on the device). Again, by averaging the data over all devices originating from the same wafer, it is possible to get a clearer picture of the situation, and to look for differences between wafers. Some wafers exhibit an unusually high temperature increase, such as R2-1302 and R2-1444, or unusually low, for R2-1126. It is interesting to study the origin of these differences. In chapter 4, the optical absorption will be measured on each of these wafers, and this data will be correlated with the temperature increase and other electro-optic properties in chapter 6.

Conclusion

Precise and reproducible measurements of the peak temperature found on the surface of waveguide devices have been performed with the LC technique, despite the problems with obtaining a thin uniform LC layer on the samples. Although the technique could probably be further improved, it is now "mature" enough to be used as a regular characterization tool for optoelectronic devices. Its simplicity and versatility ensure that it can be readily applied to other devices, such as optical switches, laser diodes, detectors, etc.

One important piece of information that can not be acquired from this technique is the internal temperature in the active region of the device. This information is important since it determines the absorption in the waveguide, and could eventually lead to accelerated degradation of the device if it is high enough. Thus, the active region temperature probably constitutes the most important information from a reliability point of view. An efficient way of knowing the internal temperature in waveguide devices that does not require complex sample preparation is to construct a thermal model. Chapter 5 will describe that work. At that time, the modelling results will be compared to the LC measurements.

Chapter 3
Instantaneous Blow-up Experiments

The instantaneous blow-up test is a standard procedure in the reliability assessment process on several optoelectronic devices. During this test, light is injected into the waveguide and the voltage is increased up to the point where the device suffers a catastrophic failure, while the optical power is usually adjusted to maintain a constant photocurrent. The failure is believed to be the result of overheating in the waveguide, which eventually leads to critical damage to the device. The blow-up voltage is an indication of the robustness of the device to catastrophic failure, and can be used to screen out weak lots of devices. Instantaneous blow-up tests identify the voltage-current combinations leading to device failure; this information helps to understand the respective influence of voltage and photocurrent on the temperature increase in the device. Finally, the instantaneous blow-up tests can also provide information related to the thermal cross-talk in hybrid devices, which was already described in chapter 2.

3.1. Samples and Setup

Blow-up experiments have been carried out on samples that differ from the ones described in chapter 1 in two aspects. First, they have not been cleaved out individually yet, but are still in a "bar" form. A bar is a row of devices on a wafer, where all the waveguides lie side by side, with an anti-reflection coating deposited on the facets. Secondly, they are composed of a laser diode and a waveguide device integrated monolithically on a common substrate, whereas the laser and the waveguide device are simply glued together in the hybrid device described in chapter 1. The bar is not attached to any carrier; this could result in slightly different thermal properties of the device. The main
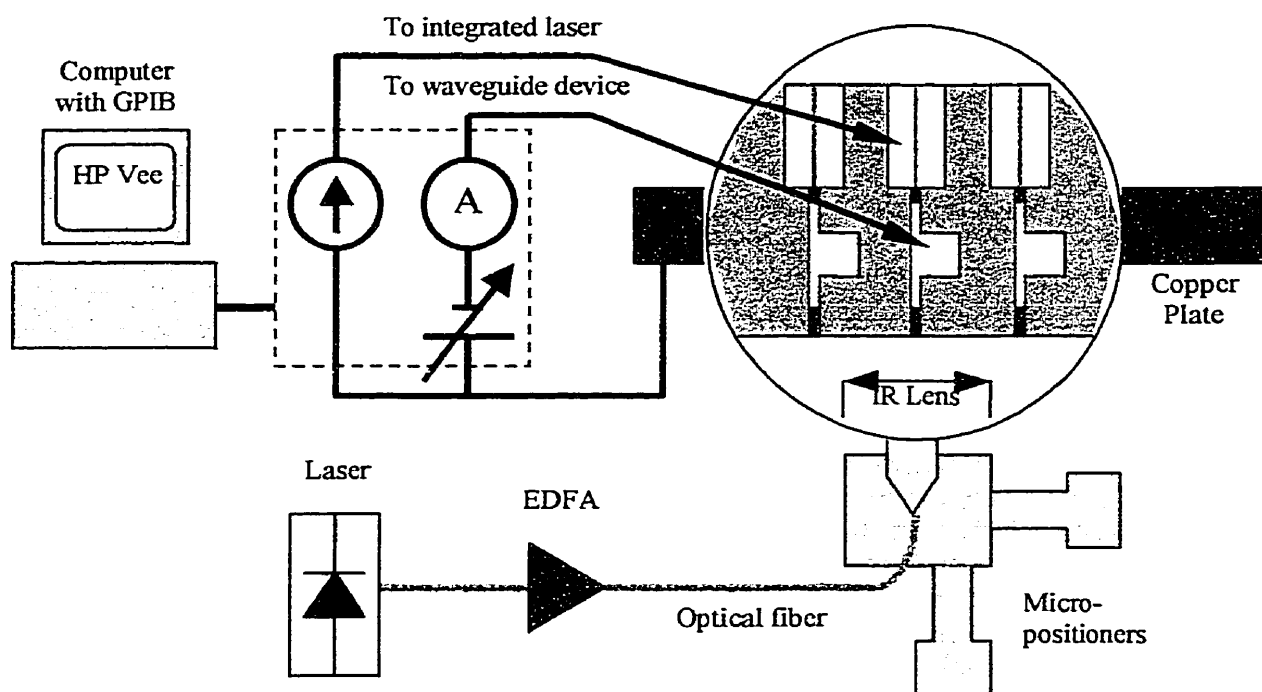
Fig. 3.1 — Setup Used for Instantaneous Blow-up Experiments

advantage of performing tests on bars instead of on individual devices is that one has access to a large number of devices with a minimum of manipulation: the electrical probes simply have to be moved from one device to another.

Because the samples are in a bar form, the test station designed for LC measurements can not serve for this experiment. The station used is depicted in figure 3.1. The bar is placed on a copper stage, whose temperature is maintained at all times at 25°C, and is held in place by vacuum. By observing through a low-magnification microscope, a set of probes can be lowered on the contact pads of the waveguide device and the laser diode. When an external light source is required, the light of a laser diode emitting at 1556 nm, amplified by an EDFA, is coupled into the waveguide through an infrared lens. A polarizing filter has been attached to the lens, to ensure TE polarization. The electrical equipment consists of a variable power supply, an ammeter and a computer that controls the station through a GPIB bus.

3.2. Test Methodology

Figure 3.2 is a block diagram showing the procedure followed during the course of the blow-up experiments.

Since one goal of these experiments was to investigate the effect of the laser heating on the blow-up conditions, two sets of experiments were realized, using the integrated laser and an external laser as the light source. The first step is to lower the probes on the contact pads of the waveguide device and the laser. The laser is then biased for the remainder of the test at a constant current (175 mA), selected to obtain maximum optical power. The computer sets the initial voltage on the waveguide device electrode at 5 V, subsequently increments the voltage by 0.1 V every second and monitors the photocurrent. A blow-up of the waveguide manifests itself as a sudden reduction of the photocurrent: the blow-up voltage and the last measured photocurrent (before the blow-up) are then recorded in a file. The probes are then moved on to the next device, and the entire procedure is repeated. Because the efficiency (and output optical power) of the integrated laser varies significantly from device to device, a broad range of photocurrent is measured at blow-up. The procedure when using the external laser is basically the same, except that the lens needs to be realigned manually each time a new device is tested. Two values of the EDFA current have been used (220 and 290 mA), which, when combined to the changing coupling efficiency from device to device, also produced a broad range of photocurrent and voltage combinations resulting in blow-up.

3.3. Results

These tests were carried out on three bars, originating from different wafers. Because of the differences in wafer characteristics, it is not advisable to compare results obtained on different wafers if one desires to observe differences between blow-up conditions when the integrated or the external laser is used. For this reason, the results are presented
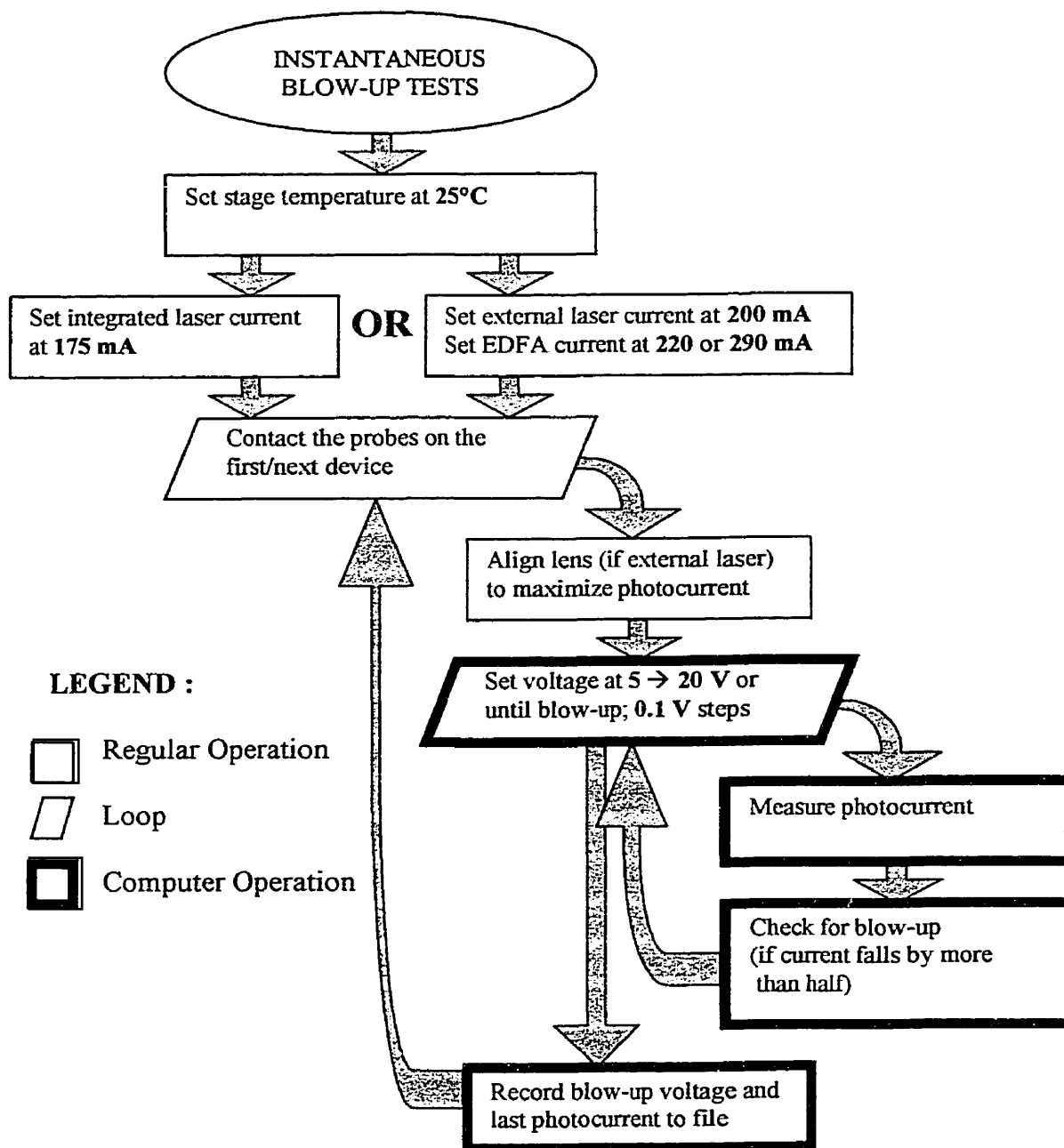
Fig. 3.2 – **Block Diagram Explaining the Instantaneous Blow-up Experiments**

separately for each bar, in figures 3.3, 3.4 and 3.5. Note that the solid and dashed lines on the graphs are only a guide to the eye and do not represent a statistical fit to the data.
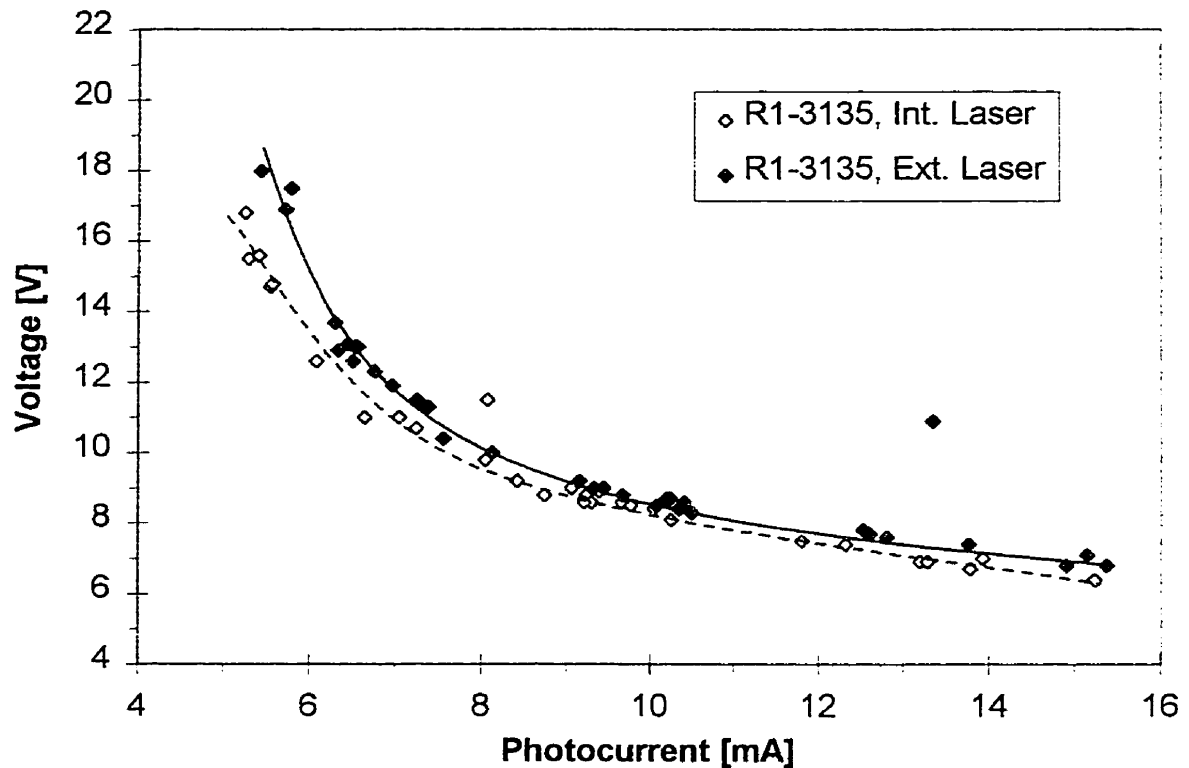
Fig. 3.3 – Instantaneous Blow-up Experiments on Wafer R1-3135

3.4. Discussion

The instantaneous blow-up data clearly demonstrates that the presence of the integrated laser heating lowers significantly the photocurrent and voltage that a device can stand before suffering a catastrophic failure. The reason is that, for the same given voltage and current, the internal temperature is expected to be higher when the integrated laser is used, because of the heat generated in the laser. This effect is obvious on wafers R1-3135 and R1-3144, but not as clear on R1-3143. This experiment thus constitutes another proof of the existence of a thermal cross-talk between the laser and the waveguide device.

The curves drawn on the graphs delimit the domain of photocurrent and voltage combinations where the devices suffer instantaneous failure. The set of conditions that lead to
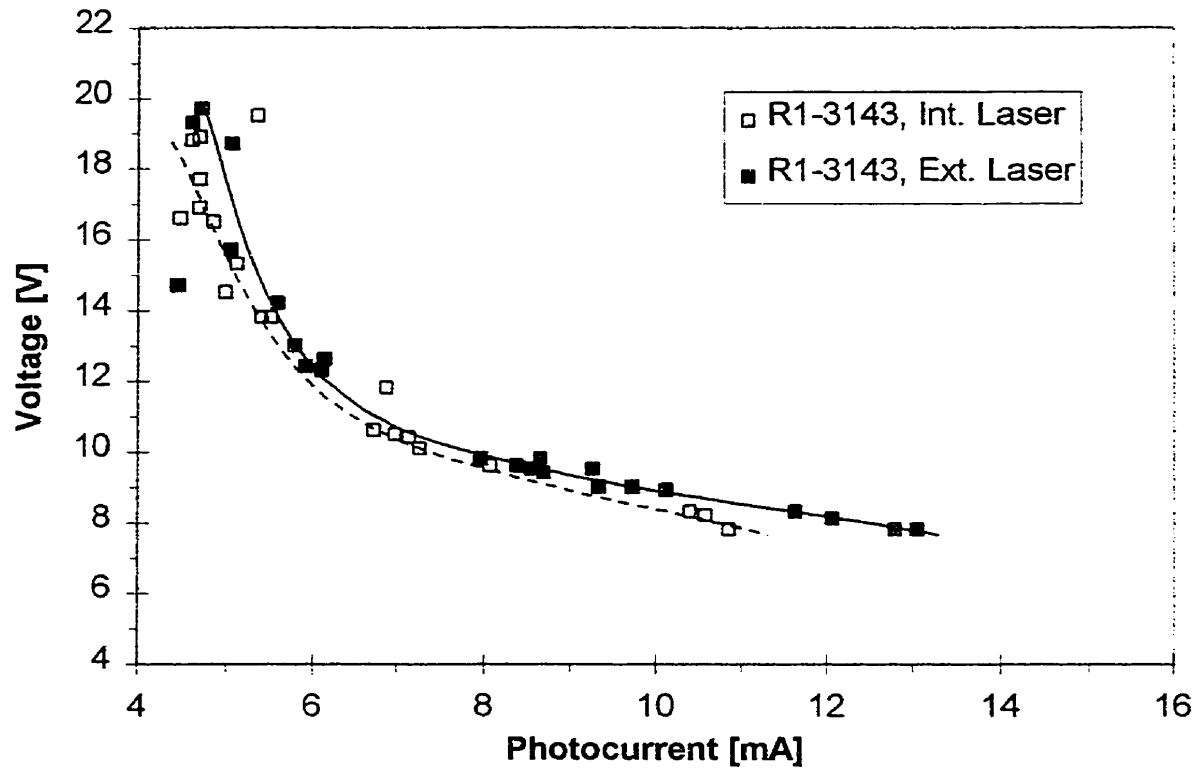
Fig. 3.4 – Instantaneous Blow-up Experiments on Wafer R1-3143

blow-up appears to follow roughly a constant $I \times V$ curve. This result is expected, since the $I \times V$ product gives the electrical power dissipated in the active region in the form of heat, and the blow-up is believed to be a direct consequence of overheating in the waveguide device. In fact, a power regression of the type $V_{bu} = A\ I_{bu}^{-r}$ (with A a constant) performed on this data gives an exponent ranging from 0.8 to 1.2 depending on the wafer. This type of regression, however, does not describe well the data, because the "curvature" of the I-V curve does not correspond to an $I \times V^r = Cst$ curve, as can be seen on figure 3.5 (where $r = 1.2$). The deviation could be explained partially by the fact that absorption increases with voltage: at higher voltages, the heat is confined to a smaller region and the electrical power required for the device to blow up is reduced.

Finally, differences in the conditions leading to blow-up on different wafers can be observed by comparing the different graphs. For example, at a photocurrent of 10.0 mA,
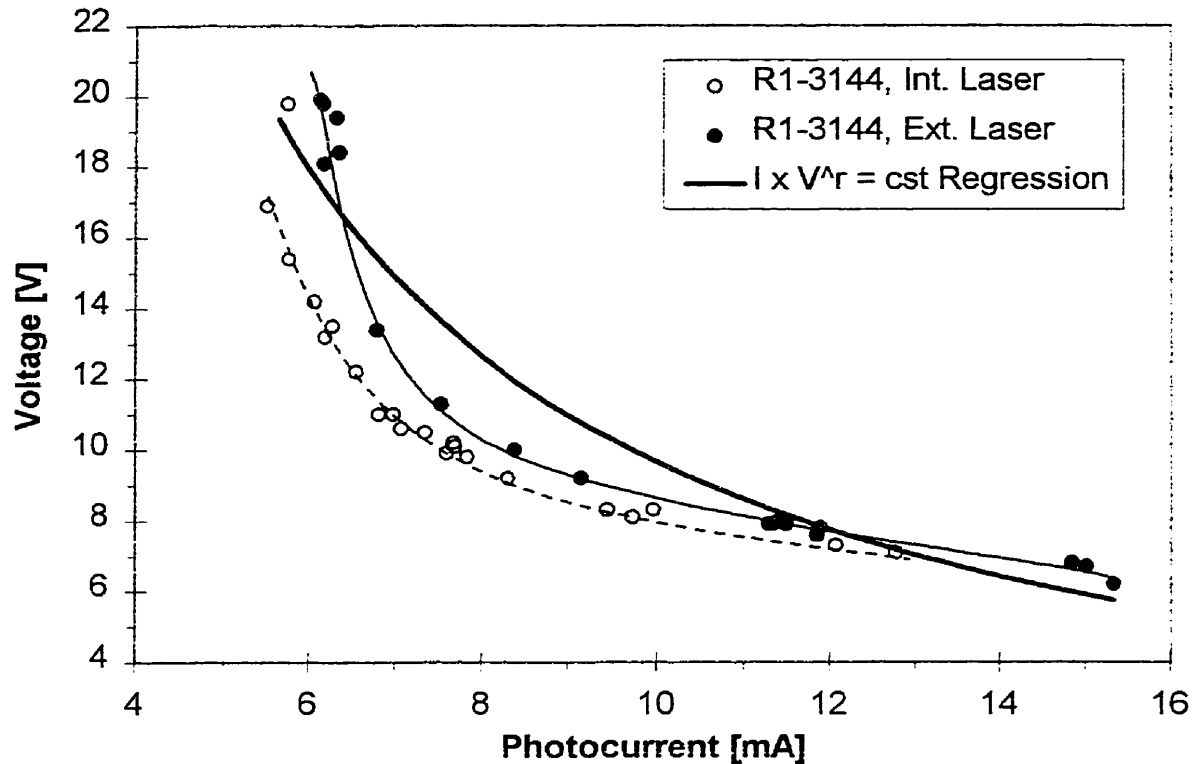
Fig. 3.5 – **Instantaneous Blow-up Experiments on Wafer R1-3144**

devices coming from R1-3135 and R1-3143 can stand about the same voltage before blowing up, while device failure occurs on R1-3144 at a slightly lower voltage. This could be explained by differences in optical absorption in the waveguide between wafers.

Conclusion

Instantaneous blow-up experiments are commonly performed to evaluate the robustness and the resistance to failure of a batch of devices. This data is believed to be linked to the reliability of the device, and these experiments also help to screen out weak lots of devices. The most interesting conclusion of the work presented in this chapter is that the presence of a neighboring laser causes a significant reduction in the photocurrent and voltage that a device can handle before catastrophic failure occurs. This confirms that a

thermal cross-talk exists between the laser and the waveguide device, and raises the question of the impact this could have on the reliability of the device. No clear answer can be given at this moment, but this issue needs to be addressed eventually if mono-lithic integration of optoelectronic devices is to become more common in the future.

Chapter 4
Absorption Measurements

Thermal modelling of the waveguide device requires a precise knowledge of the optical absorption occurring inside the MQW and how it changes with voltage and temperature. Measuring the absorption loss in the waveguide as a function of voltage and temperature is a straightforward task; however, for reasons that will be explained shortly, it is impossible to cover a large temperature range in this manner. A second set of experiments, using an alternate type of device, is necessary. The final goal of this work is to obtain the absorption coefficient in the waveguide as a function of voltage and temperature over ranges of 0 to 10 V and 20 to 220°C.

The first section of this chapter defines the absorption coefficient and explains the causes of its dependence on voltage, temperature and wavelength. The experiments performed on waveguide devices and on large-area devices, which resemble *p-i-n* photodiodes, are described in the following sections, and a graph showing the absorption coefficient over the full ranges of temperature and voltage is presented. The dependence of absorption with respect to wavelength was also studied, even though it has no direct impact on the remainder of this work. The results are shown in a summarized form and discussed.

4.1. Definition of the Absorption Coefficient

As light travels along the waveguide, a fraction is absorbed in the MQW and in the other materials composing the waveguide, and another part is scattered out of the waveguide.

The sum of these losses is the **propagation loss**. The remaining optical power in the waveguide at position x is given by:

$$L(x) = L_0 \exp\left(-\int_0^x \alpha(x')dx'\right) \qquad \{4.1\}$$

where L_0 is the optical power at the entrance of the waveguide and α is the **absorption coefficient**, which can vary along the length of the waveguide. This "effective" absorption coefficient is specific to the geometry of the waveguide and to the unique propagating mode sustained by the waveguide, and is not the absorption coefficient of the bulk material. As the applied voltage or the temperature change, the scattering loss and the absorption in the materials surrounding the MQW should not vary significantly, and are assumed to remain constant. However, in the MQW, the absorption is strongly dependent on both temperature and voltage. The electric field in the MQW (determined by the applied voltage) influences absorption because of the quantum-confined Stark effect, as explained in chapter 1; temperature also has a strong influence on the absorption coefficient, because the band gap decreases as temperature increases. This has little effect on the absorption taking place in InP or InGaAs, because the band edge lies far away from the photon energy at a wavelength of 1556 nm. However, the quantum well composition is adjusted so that the band gap lies close to the photon energy: in this case, a small change in the band gap, induced by a temperature variation may result in a large change of absorption in the MQW.

When the propagation loss is measured in the waveguide, the measured loss is the sum of the loss due to absorption in the MQW and in the other materials, the scattering loss and the coupling losses at both ends of the waveguide where the light is coupled to tapered fibers. For reasons that will be explained in the next section, it is impossible to distinguish between the scattering loss, coupling losses and absorption in materials other than the MQW: the only loss that can be measured accurately is the absorption in the MQW that gives rise to a photocurrent. Thus, the absorption coefficient measured in these experiments refers only to the absorption loss in the MQW. However, the com-

bined scattering losses and absorption in the other materials is not expected to be very large: previous work done at Nortel indicates that the combined losses in the waveguide are about 2 to 3 dB/mm in an unbiased device. This value is low enough so that this simplification should not have any significant impact on the remainder of this work.

4.2. Direct Measurements of Absorption in the Waveguide

When the absorption loss is measured directly in the waveguide, the device is reverse-biased, so that an electric field appears across the MQW, in a direction perpendicular to the propagation of light. Light is injected into the waveguide and the intensity of the light exiting the device and the photocurrent generated in the process are measured and recorded. When the measurement is repeated at different voltages and temperatures, the absorption coefficient can be obtained for any combination of these variables. This section describes the experiments and shows the results of the measurements performed on waveguide devices.

4.2.1. Description of Setup

The test station used to measure absorption in the waveguide is the one on which the liquid-crystal measurements are carried out, with the addition of a computer-controlled optical power meter. The samples are the narrow-electrode devices described in chapter 1. Light is injected into the device and collected out of it by two tapered fibers. The optical power is usually delivered by a laser diode emitting at a wavelength of 1556 nm; when a different wavelength is required, a tunable laser source is used.

4.2.2. Test Methodology

Figure 4.1 shows a block diagram describing the test procedure. The first step is to adjust the polarization to couple light in the TE mode of the waveguide; the procedure

was already explained in chapter 2. For the whole duration of the measurements, the external laser current is set at 75 mA, at which point the photocurrent does not exceed 0.5 mA; according to the thermal model to be presented in chapter 5, the internal temperature increase at 8 V resulting from this current should be less than 3°C. The current is delivered by a precision current source, ensuring current stability within 0.01 mA. Once the sample is in place under the microscope and the probes are contacting the carrier pads, the temperature of the stage holding the device is first set at 10°C, and a voltage of 10 V is applied on the waveguide electrode. The precision of the thermo-electric cooler is about 0.1°C, and it takes from a few seconds to a minute to achieve a stable temperature. The input fiber is then aligned manually using the micropositioners: optimal alignment is achieved when the photocurrent in the device is maximized. The voltage is then reduced to 0 V and the output fiber is aligned by maximizing the optical power measured in the fiber. The voltage is then scanned across a range of 0 to 10 V and the photocurrent and optical power at each voltage are measured and recorded by the computer. The stage temperature is subsequently increased to 15°C and the whole operation is repeated, including the realignment of both fibers (necessary because of the thermal expansion of the stage and the sample). The highest temperature at which measurements are carried out is 60°C (70°C in some instances); past that point, the presence of convection air currents over the stage cause the fibers to move, inducing a large noise in the measurements.

In many but not all devices, the leakage current was also measured; this is the current flowing through the device in the absence of light in the waveguide. For these measurements, the same procedure is executed, without injecting light into the waveguide.

4.2.3. Data Processing

Obtaining the absorption coefficient from the tests described above requires some elaborate calculations. First, the leakage current must be subtracted from the total measured current, to find the photocurrent:

WAVEGUIDE ABSORPTION MEASUREMENTS

- Place sample on stage
- Contact probes

Adjust polarization to have TE mode

Set laser current at 75.0 mA

Set temperature at 10 → 70°C; 5°C steps

- Set $V = 10$ V
- Align input fiber to maximize photocurrent

- Set V = 0 V
- Align output fiber to maximize output power

Set voltage at 0 → 10 V; 0.5 V steps

- Measure photocurrent
- Measure output power
- Record results in file

LEGEND :

☐   Regular Operation

▱   Loop

▣   Computer Operation

Fig. 4.1 – Block Diagram Describing the Absorption Measurements

$$I_{ph} = I_{tot} - I_{leak} \qquad\qquad \{4.2\}$$

However, in most cases where the leakage current was measured, it was found to be only a small fraction of the total current. The leakage current is usually in the microampere range, or around 1 % of the total current. In this case, it can be neglected, and the measured current is assumed to be equal to the photocurrent. In the few devices where the leakage current was found to be greater (100 μA in the worst case), it was measured over the full temperature and voltage ranges and subtracted from the total current.

The next step is to evaluate how well the light coming out of the waveguide is coupled in the output fiber. This is given by the output coupling efficiency (*OCE*), defined as the ratio of the optical power collected by the output fiber, $L_{out,f}$, to the power inside the waveguide at the output facet, $L_{out,wg}$, so that

$$L_{out,f} = OCE \; L_{out,wg}$$
$$= OCE \left(L_{in,wg} - I_{ph} \left(\frac{h\,c}{e\,\lambda} \right) \right) \qquad\qquad \{4.3\}$$

Equation 4.2 assumes an internal quantum efficiency of 100%: this means that every absorbed photon generates an electron-hole pair that contributes to the photocurrent. This is justified by the intense electric field present in the MQW, which rapidly sweeps away charge carriers, leaving no time for recombination processes to occur. Note that the factor $hc / e\lambda$ is the ratio of the charge of an electron to the energy of a photon, and establishes the correspondence between photocurrent and optical power absorbed. At 1556 nm, this factor equals almost exactly **1.25 A/W**, meaning that the absorption of 1 mW of light generates a photocurrent of 1.25 mA in the device. Because the optical power coupled in the waveguide, $L_{in,wg}$, is unknown at this moment, the *OCE* is calculated from the variations in output power and photocurrent with respect to voltage:

$$L_{out.f}^{V_1} - L_{out.f}^{V_2} = OCE \left(L_{out.wg}^{V_1} - L_{out.wg}^{V_2} \right)$$

$$= OCE \left(\frac{h\,c}{e\,\lambda} \right) \left(I_{ph}^{V_2} - I_{ph}^{V_1} \right) \qquad \{4.4\}$$

$$\Rightarrow OCE = \left(\frac{e\,\lambda}{h\,c} \right) \left(\frac{L_{out.f}^{V_1} - L_{out.f}^{V_2}}{I_{ph}^{V_2} - I_{ph}^{V_1}} \right)$$

where V_1 and V_2 can be any pair of voltage values. It is preferable to take these two voltages far apart, since this minimizes the effect of uncertainty and noise in the measurements. V_1 and V_2 were chosen to be 1 and 6 V, respectively. Following this, the total power coupled in the waveguide, $L_{in.wg}$, can be calculated as the sum of the light absorbed in the waveguide, obtained from the photocurrent, and the light exiting the waveguide:

$$L_{in,wg} = L_{out,wg} + I_{ph} \left(\frac{h\,c}{e\,\lambda} \right)$$

$$= \frac{L_{out.f}}{OCE} + I_{ph} \left(\frac{h\,c}{e\,\lambda} \right) \qquad \{4.5\}$$

The optical power in the waveguide is assumed to be different every time temperature changes, since the alignment is readjusted. For each temperature used in the test, the value of $L_{in.wg}$ used for further calculations is the average of the values of $L_{in.wg}$ calculated for every voltage. This value is close to 0.4 mW, since the laser current was chosen in order to have a maximum photocurrent of around 0.5 mA. Note that, in equation 4.5, $L_{in.wg}$ does not include the light that has been scattered out of the waveguide or the light absorbed in materials other than in the MQW, because such losses do not generate a photocurrent. Even if the optical power in the input fiber was known, there is no way to distinguish between the input coupling loss, the scattering loss and the absorption loss in other materials. This justifies the previous claim that the only loss that can be accurately measured in these experiments is the absorption loss in the MQW.

The last step is to compute the loss in the waveguide due to absorption in the MQW, for all combinations of voltage and temperature. The absorption coefficient, α, can be obtained in the same manner.

$$Loss = -10\log\left(\frac{L_{out,wg}}{L_{in,wg}}\right) = -10\log\left(\frac{L_{out,f}}{OCE \times L_{in,wg}}\right)$$

$$\alpha = \frac{1}{l}\ln\left(\frac{L_{out,f}}{OCE \times L_{in,wg}}\right)$$

{4.6, 4.7}

where l is the length of the electrode covering the device, which is 600 μm. Note that the absorption loss and the absorption coefficient are proportional to each other, the scaling factor being $(\ln 10) / (10\, l)$ m^{-1}/dB.

4.2.4. Results

Absorption measurements were performed on two devices coming from each of a set of 9 wafers (only one device was available for R2-1510). Figures 4.2 and 4.3 show typical examples of the results obtained on a single device: the absorption loss is plotted as a function of voltage in the former, and of temperature in the latter. In all cases, the two devices coming from the same wafer have similar absorption curves, and the absorption loss was averaged on the two devices to study the differences between wafers. Figure 4.4 presents the absorption measured on all wafers at 5 V.

4.2.5. Discussion

In figure 4.2 and 4.3, the measured absorption loss increases rapidly with voltage and temperature until it reaches about 40 dB. Past that point, the curves seem to enter a "saturation" regime. This is an artifact of the measurement method, since the experiments described in the next section demonstrate that the absorption loss should continue to increase rapidly beyond 40 dB. The reason why it is impossible to measure losses
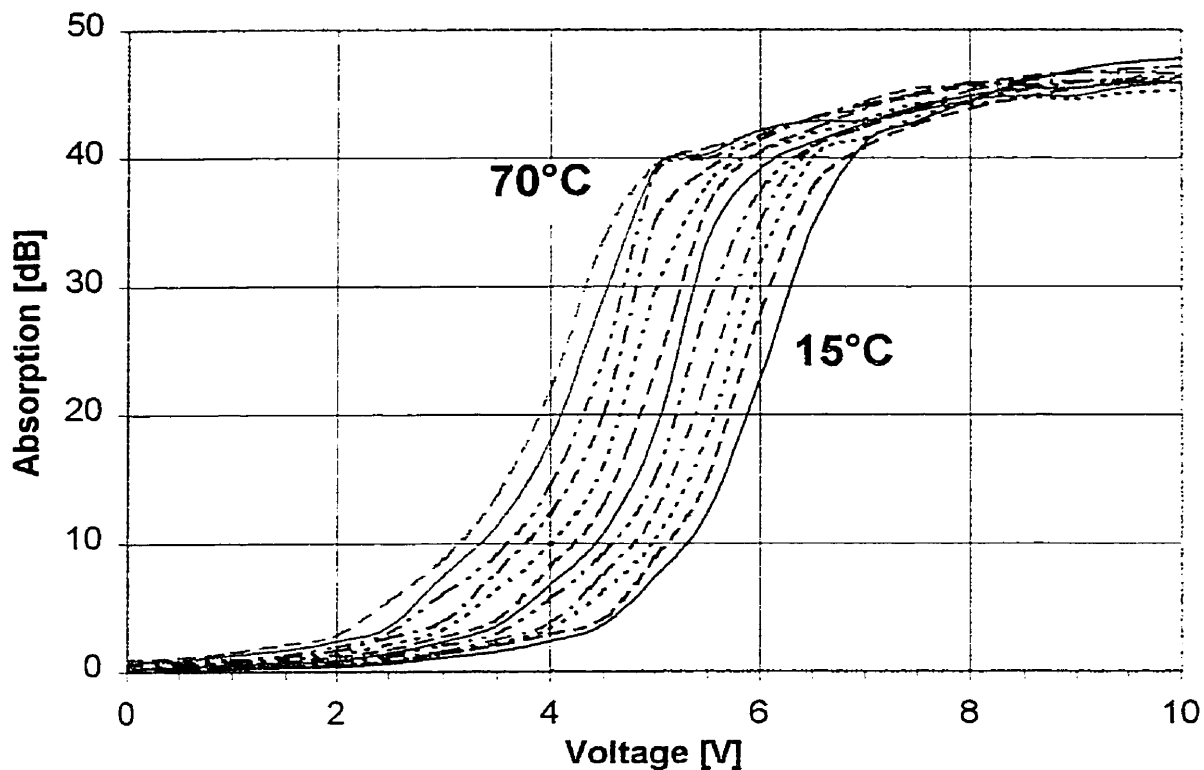
Fig. 4.2 – Absorption vs. voltage and temperature in a 600 μm Waveguide on Wafer R2-1444

exceeding 40 dB in this experiment is that the optical power at the exit of the waveguide is too small to make accurate measurements. The only way to raise this limit is by injecting more light in the waveguide; this is however not desirable because it could lead to excess heating in the device, causing the internal temperature to differ significantly from the stage temperature.

These results show that absorption rapidly changes with both voltage and temperature. For example, at 6 V, absorption more than doubles (4 dB increase) when temperature goes from 20 to 25°C, a change not unlikely to happen in normal lab conditions. This demonstrates the necessity of fine temperature control when testing optoelectronic devices.

The difference in absorption between wafers can be best observed at a moderate voltage (4 – 6 V), before the 40 dB limit is reached. It is believed that the absorption character-
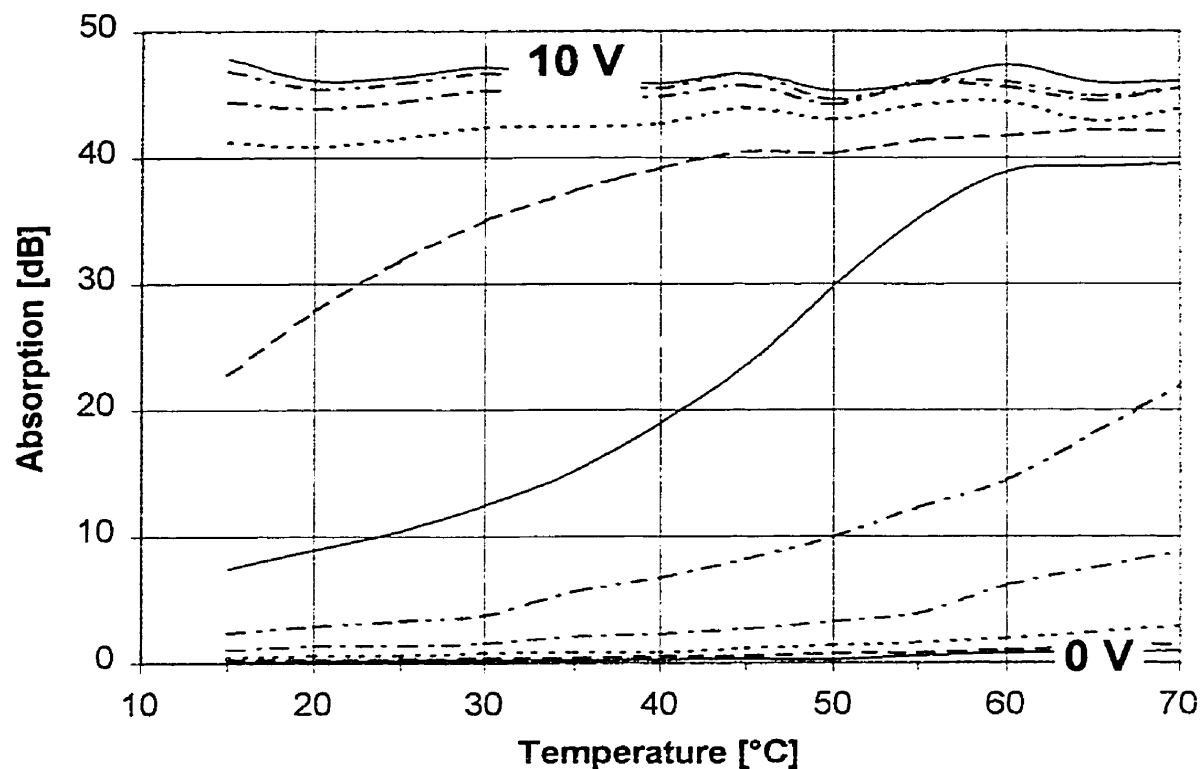
Fig. 4.3 – Absorption vs. voltage and temperature in a 600 μm Waveguide on Wafer R2-1444

istics are common to all devices coming from the same wafer, since absorption should be determined by the exact composition and thickness of the semiconductor layers grown on the wafer. This is verified by the experiments, as in all cases the two devices coming from the same wafer have similar absorption curves. The absorption curves measured on different wafers are further discussed in the next section.

4.3. Large-Area Detector-Like Device

When the absorption loss is 40 dB or above, virtually all light (99.99%) is absorbed over the length of the device. However, as the absorption coefficient continues to increase, the light is also absorbed over a shorter and shorter length of the device, causing the local temperature to continue to rise with increasing voltage. So it is still important to
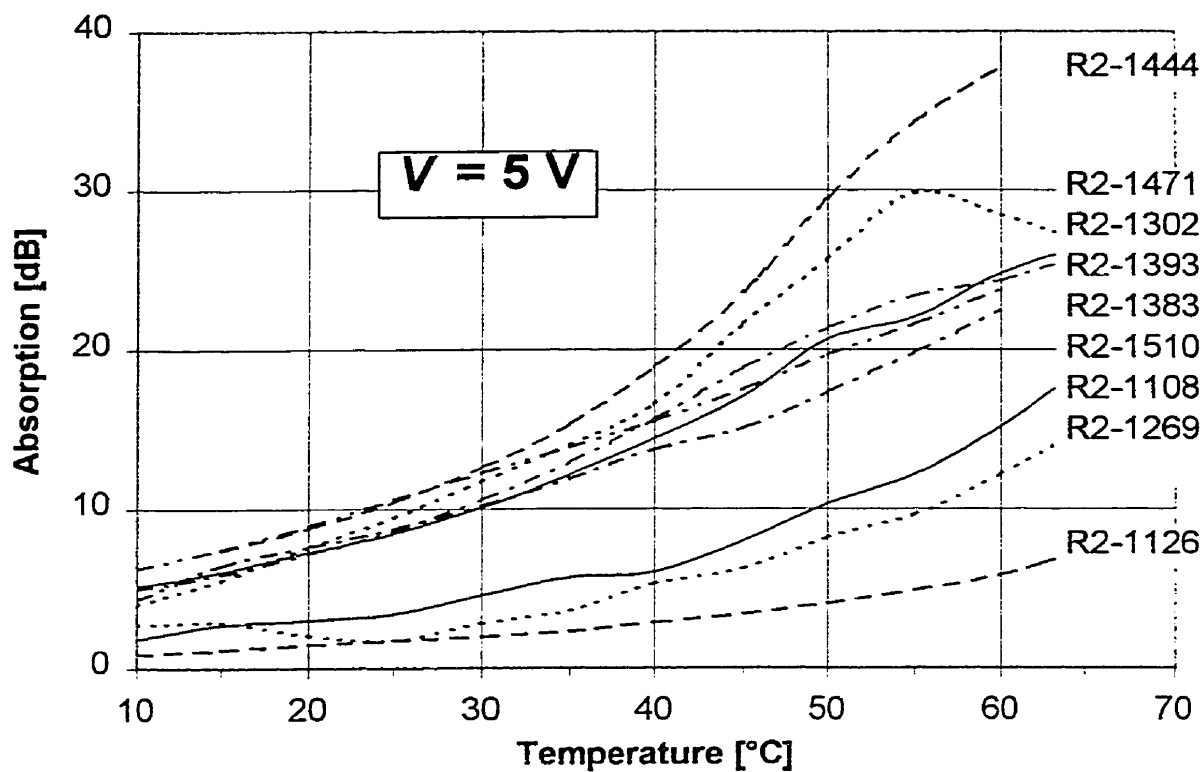
Fig. 4.4 – Comparison of the Absorption Curves on All Wafers, at 5 V

know what the absorption coefficient is in the waveguide at high voltages and temperatures, where the absorption loss exceeds 40 dB.

A second set of measurements was performed on an alternate device to obtain the absorption coefficient at high temperatures and voltages. It is a test device found on the same wafers, resembling a *p-i-n* photodiode (see figure 4.5). The device consists of a rectangular electrode deposited on top of the semiconductor layers, the same layers found in the ridge of the waveguide device; a circular window (diameter: 150 μm) is opened in the electrode. When light is injected through this window, a fraction is absorbed as it crosses the MQW vertically, giving rise to a photocurrent when the *p-n* junction is reverse-biased. This current can be measured by establishing an electrical contact with the top, *p*-side electrode and the bottom, *n*-side electrode. The absorption in the device can then be deduced from the photocurrent. Since the MQW thickness is

only 0.35 μm, the absorption is much smaller than in the 600 μm-long device, and measurements can be performed even in very high voltage and temperatures conditions without running into the problems mentioned in the previous section. The use of the large-area device also simplifies the measurement procedure, because it removes the need to maintain a precise alignment of the tapered fiber. A hot plate was used to heat the devices up to 220°C. Once the photocurrent is measured at every possible combination of voltage and temperature, the results of these measurements can be combined with the waveguide measurements to obtain the absorption coefficient over the full range of temperature and voltage.

4.3.1. Description of Setup

The setup used for the absorption measurements on large-area devices is shown in figure 4.5. The device is wire-bonded to an alumina (Al_2O_3) carrier and placed on a hot plate. A thermal paste was used to insure a good thermal contact between the carrier and the hot plate. A thermocouple monitors the temperature. The light is delivered to the device by means of a standard fiber with a cleaved facet. The optical source was a laser diode emitting at 1556 nm. The station also consists of a variable voltage source, a digital ammeter and a computer that controls the whole operation.

4.3.2. Procedure

Figure 4.6 shows a block diagram describing the procedure of the absorption measurements on the large-area devices. Because of the geometry of the device, the polarization of incoming light is irrelevant. The sample is placed on the hot plate, and two probes are put in contact with the carrier contact pads, which are connected to the p-side and n-side electrodes of the device. The hot plate is then heated up to 220°C, a temperature where the device does not seem to suffer any degradation, and the fiber is placed in front of the window in the top electrode. The computer then measures the photocurrent as a function of voltage from 0 to 10 V, with a step of 0.5 V, every time the temperature drops by 5°C.
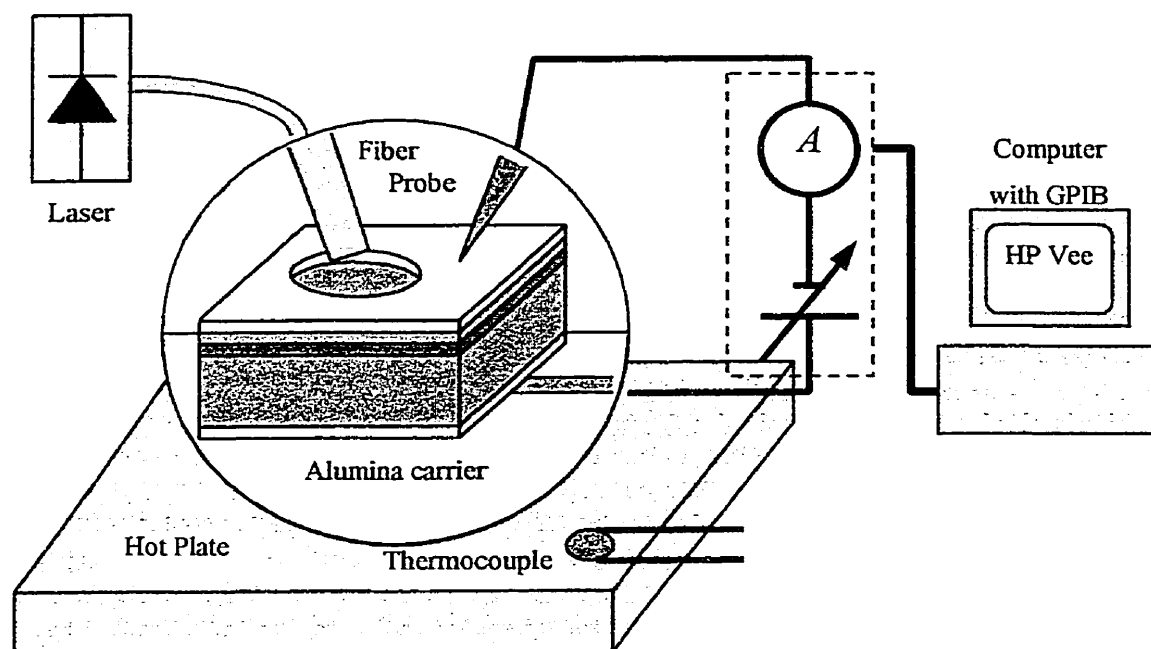
Fig. 4.5 – Setup Used for Measurements on Large-Area Devices

The procedure is repeated until the temperature comes down to 25°C. Throughout the experiment, the fiber is continuously realigned manually to insure that it remains over the window. Because of the finite time needed to measure the photocurrent at each voltage and the fact that the temperature drops continuously, the temperatures associated with the measurements are only precise within 1°C.

Because of the large area of the device, the leakage current could represent a significant fraction of the total current measured. The leakage current was measured on most devices, by repeating the procedure described above, without illumination. The device was rejected if the leakage current was found to be more than 10% of the total current.

4.3.3. Data Processing

Under certain assumptions, the photocurrent measured in the large-area device is proportional to the absorption coefficient, and the latter can be obtained by simply multiplying the photocurrent by a scaling factor. These assumptions are that the leakage current is negligible and that the MQW thickness is much smaller than the absorption
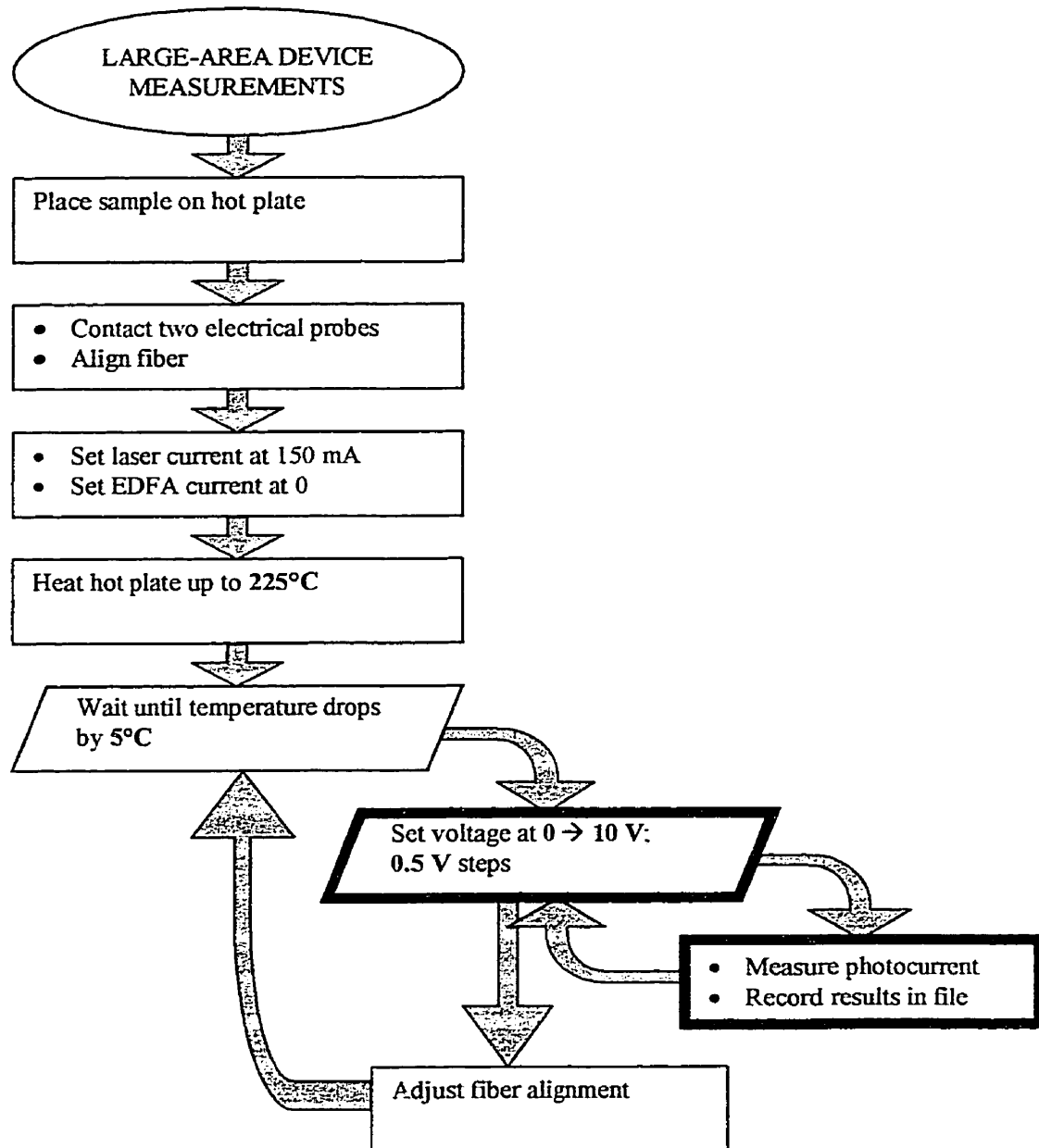
Fig. 4.6 – **Block Diagram Describing Measurements on Large-Area Devices**

length, α^{-1}. The former was already verified experimentally to be true. The latter can be confirmed by observing that the optical power in the fiber is set at approximately 3 mW, while the maximum photocurrent measured is 0.2 mA; this corresponds to only about 5% of absorption, meaning that the absorption length is much greater than the MQW thickness. Under these conditions,

$$I_{tot} = I_{ph} + I_{leak.} \approx I_{ph}$$

$$= \gamma \left(\frac{e\,\lambda}{h\,c}\right) L_0 \left(1 - e^{-\alpha\,t}\right)$$

$$\approx \gamma \left(\frac{e\,\lambda}{h\,c}\right) L_0 \left(1 - (1 - \alpha\,t)\right) \quad \text{since} \quad \alpha\,t \ll 1 \qquad \{4.8\}$$

$$= \gamma \left(\frac{e\,\lambda}{h\,c}\right) L_0\,\alpha\,t$$

t is the MQW thickness and the factor γ represents the fraction of the light in the fiber that reaches the MQW, and differs from unity because of the reflection on top of the device and absorption in the p-doped InGaAs cap layer underneath the gold electrode. Instead of evaluating directly this factor, the scaling factor between photocurrent and absorption coefficient is obtained by calculating the ratio of the photocurrent measured in large-area devices and the absorption coefficient obtained from the waveguide measurements. The ratio is averaged over the whole range where the two sets of data overlap (0 – 6 V, 30 – 60°C), excluding the conditions where the absorption in the waveguide exceeds 40 dB. A typical value of the ratio is 5×10^8 m^{-1}/A. The photocurrent is then multiplied by this factor and combined with the waveguide data to obtain the absorption coefficient, α (V, T) over the full ranges of 0 – 10 V and 10 – 220°C.

In this discussion, we assume that the absorption measured in the waveguide device and in the large-area device are proportional to each other. This is true only if the absorption taking place in materials surrounding the MQW and still generating a photocurrent is negligible. Since the geometry of the optical modes is completely different in the two devices, this absorption should have different effects in the two cases, and the two values of the absorption could be no longer proportional. The absorption occurring outside the MQW in the waveguide device is very small, as already mentioned. In the large-area device, some absorption takes place in the two InGaAs layers, but this should not generate a significant photocurrent, since these layers are heavily doped and not depleted of

carriers. Thus, the assumption that the absorption in the two devices are proportional to each other is justified.

4.3.4. Results

Figure 4.7 shows typical results of the photocurrent measurements on one sample from wafer R2-1444, where the photocurrent is plotted as a function of temperature and voltage. The small kinks in the curves are due to measurements where the optical fiber was slightly misaligned. This data was combined with the waveguide measurements already presented in figure 4.3 to obtain the absorption coefficient over the full temperature range: the result is shown in figure 4.8. It is also instructive to compare the measurements performed on different wafers; figure 4.9 shows the photocurrent measured on devices coming from different wafers as a function of temperature, at a constant voltage of 7 V. Finally, figure 4.10 shows the absorption calculated on the same wafers, again at 7 V.

4.3.5. Discussion

Interesting features appear in the absorption graphs. First, on figure 4.8, the absorption curves corresponding to different voltages meet together around 160°C, meaning that at that temperature, absorption is virtually independent of voltage, in stark contrast with the situation prevailing at lower temperatures. Another important observation is that at 10 V, absorption is almost a linear function of temperature; at low voltages (less than 3 V), the absorption increases with temperature following an exponential behavior (this was verified by performing statistical regression on the data) up to approximately 180°C, after which the rate of variation of absorption with temperature decreases. Eventually, the absorption is expected to level off at even higher temperatures, when the band gap in the MQW is reduced far below the photon energy. Unfortunately, it is impossible to extend the measurements to higher temperatures, because of the damage sustained by the devices, manifesting itself in the form of sudden increases in the leakage current.
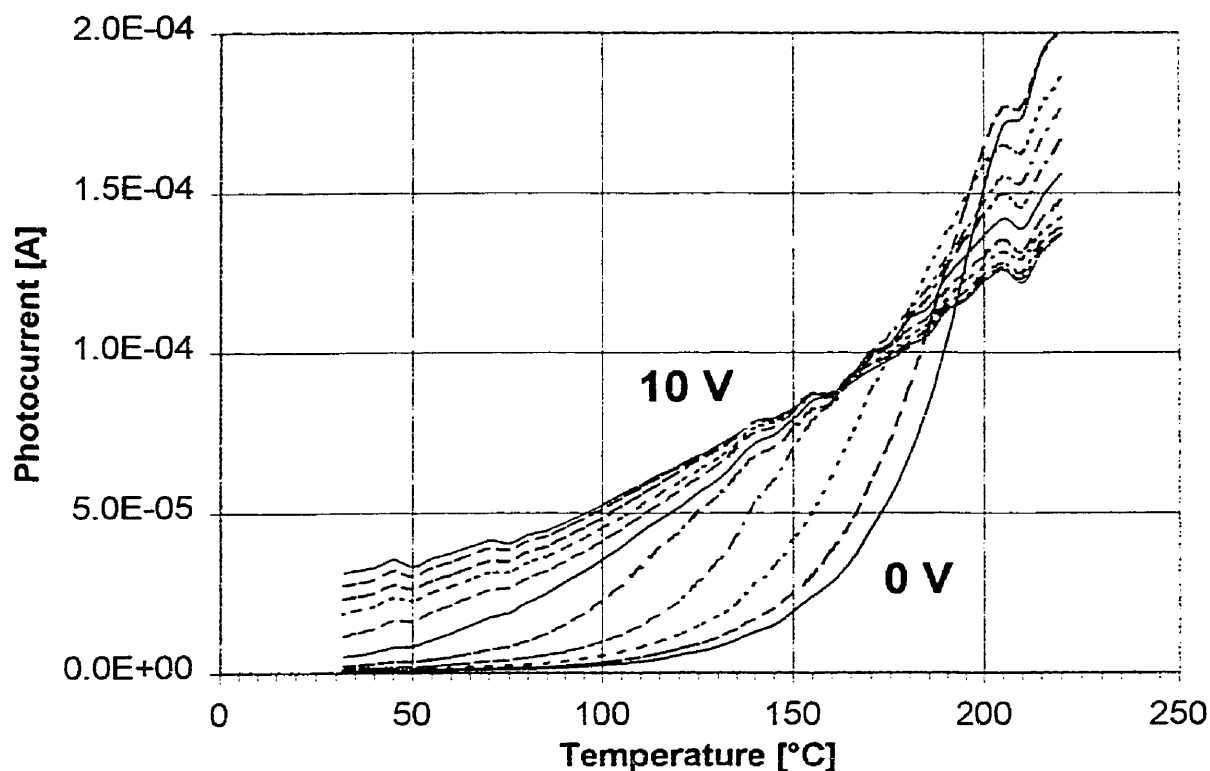
Fig. 4.7 – Measurements on a Large-Area Device from Wafer R2-1444

A comparison of the photocurrents measured on large-area devices shows only modest differences between wafers. When the waveguide data and the large-area device data are merged together, the agreement between them is good over the voltage and temperature ranges where they overlap: no important discontinuity is seen at the point of junction. Surprisingly, a comparison of the absorption curves measured on different wafers, in figure 4.10, reveals differences more important than when the photocurrents were compared in figure 4.9. The curves also do not follow the same ordering in the two graphs, meaning that a higher photocurrent does not correspond necessarily to a higher absorption. For example, wafer R2-1471 shows a small photocurrent, but yet a higher absorption loss than the others. This signifies that the differences observed between the absorption curves in figure 4.10 originate from differences in the waveguide measurements. The reason for the lack of correlation between photocurrent and waveguide absorption is not known exactly at this moment. One possible cause would be a differ-
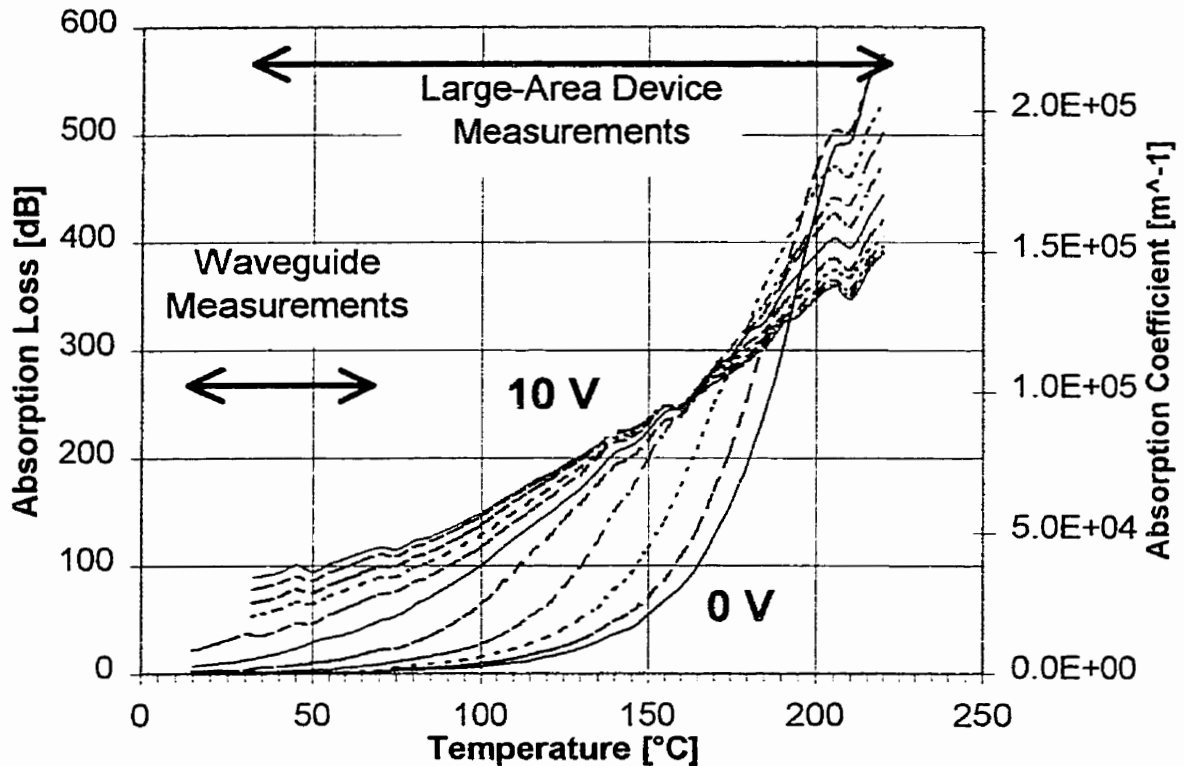
Fig. 4.8 – **Absorption in the Waveguide on Wafer R2-1444**
This graph combines the results obtained on waveguide devices and large-area devices;
the absorption loss is given for a waveguide length of 600 μm.

ence in optical confinement between wafers: this would result in a different absorption loss suffered by the optical mode in the waveguide, but would not impact the photocurrent measurements.

For further work, namely thermal modelling in chapter 5, only the absorption curves measured on wafer R2-1444 were retained, since they resemble the majority of the curves measured on other wafers and look realistic.

4.4. Absorption Coefficients

The curves giving the absorption coefficient on wafer R2-1444 were fitted to fifth-order polynomials for further investigations. Lower-order polynomials were also used where
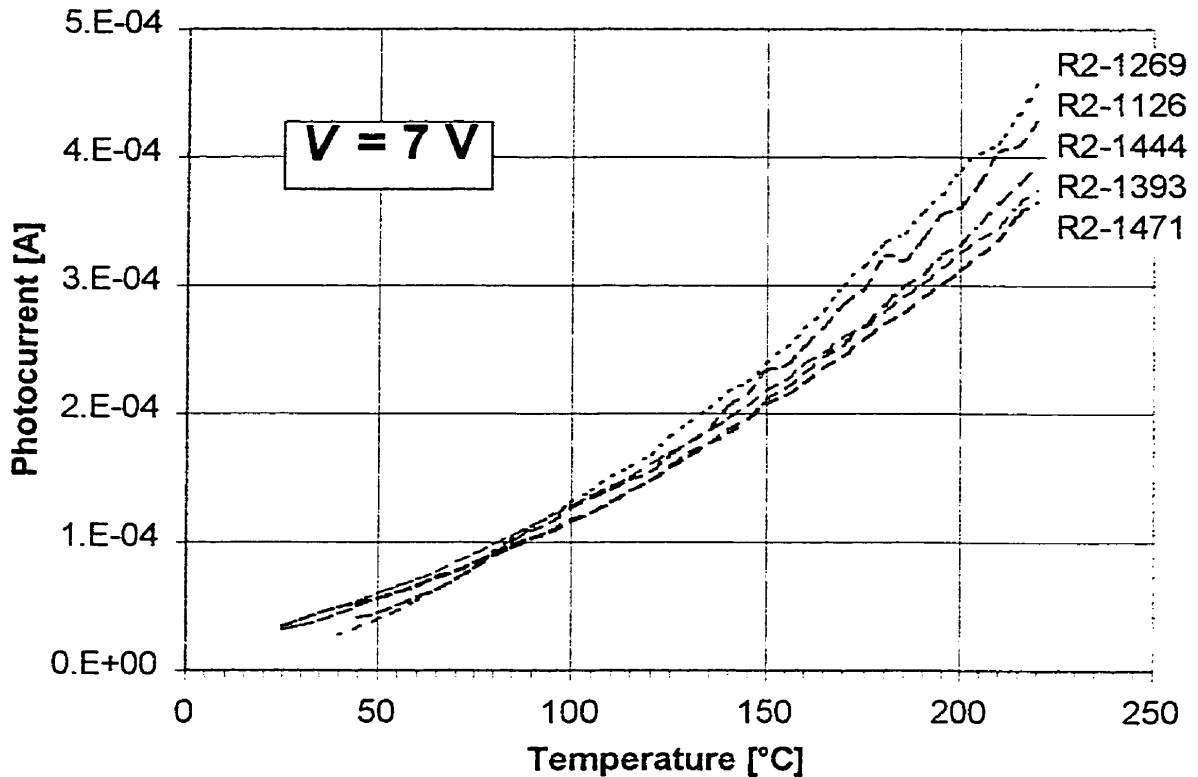
Fig. 4.9 – Comparison of the Photocurrent Measured on Several Wafers, at 7 V

they could accurately describe the absorption data. Because during thermal modelling the voltage is usually set to a known value whereas the temperature in the device is at first unknown, each polynomial gives the absorption coefficient as a function of temperature for one voltage. The result is a table of polynomial coefficients, which is given in appendix D. Under 5 V, the polynomial fits are only accurate up to about 70°C, since polynomials could not be well fit over the full temperature range; otherwise the fits are accurate up to 250°C. This table of coefficients can easily be exported to other software, such as a spreadsheet application, for further work.

4.5. Wavelength-Dependent Absorption

The absorption coefficient strongly depends on wavelength in a semiconductor, especially when the photon energy is close to the band gap energy. This is the situation
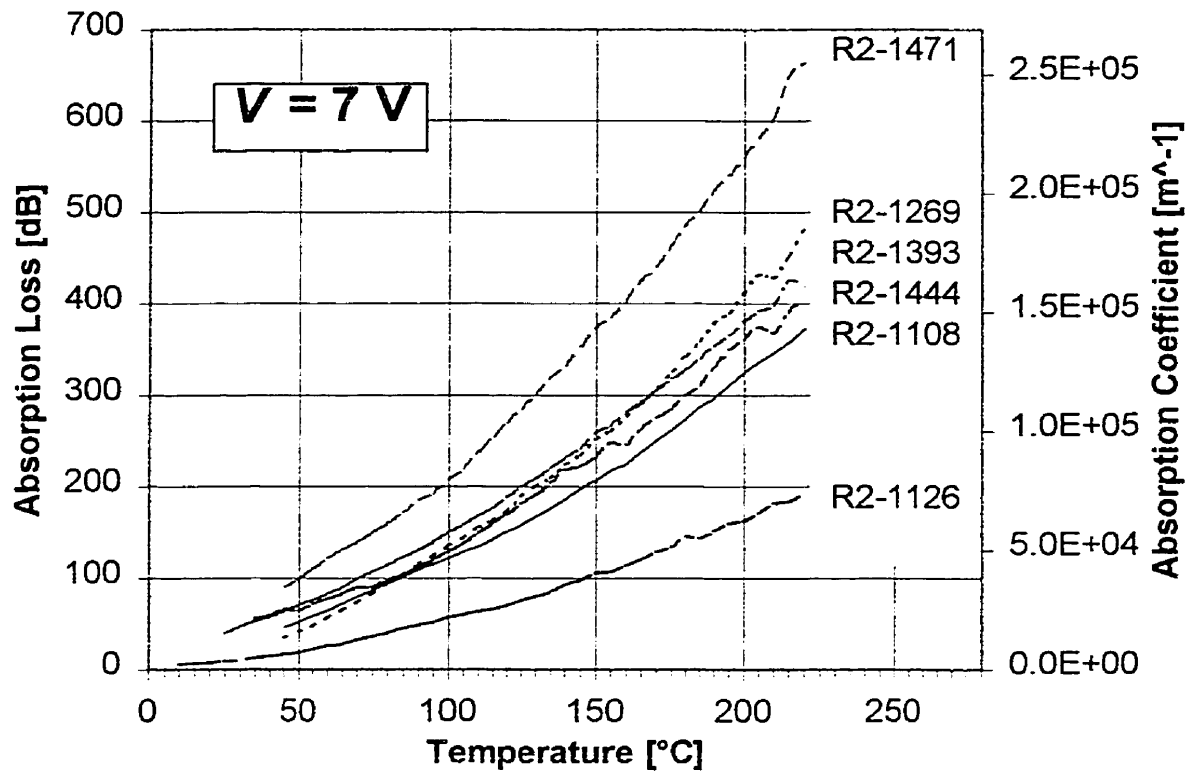
Fig. 4.10 – Comparison of the Absorption Measured on Several Wafers, at 7 V

prevailing in the MQW present in the waveguide device, which is then very sensitive to changes in wavelength. Many telecommunication systems have a way to monitor and adjust the wavelength of emission of the laser source to ensure that it remains constant over time, so this is not expected to cause major problems for the operation of the waveguide device. However, it is still instructive to look at the dependence of absorption on wavelength, to understand the behavior of absorption. This section describes the experiments carried out to study the dependence of absorption with respect to wavelength, voltage and temperature.

The experiments consisted of repeating the measurements performed on large-area devices while using different wavelengths. All measurements were carried out on samples from wafer R2-1393. Because the procedure has already been described, only the results are presented here, in figures 4.11 and 4.12. These graphs show the photocurrent
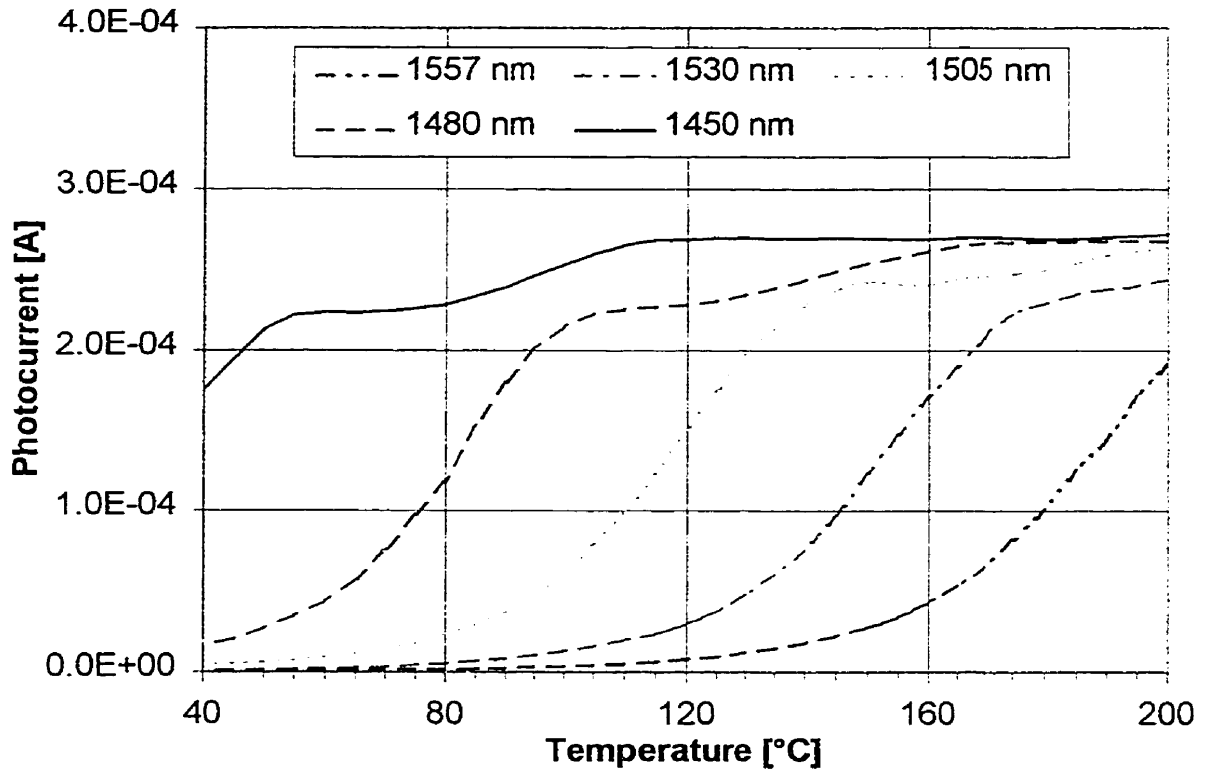
Fig. 4.11 – Photocurrent in Large-Area Device at Different Wavelengths, at 1 V

measured in the devices at 1 and 5 V, when five different wavelengths were used, ranging from 1557 nm (the nominal wavelength for the operation of the device) to 1450 nm. The two graphs indicate how the absorption curves evolve with increasing voltage. On the other hand, waveguide measurements at short wavelengths are almost impossible since the waveguide then becomes opaque to the light, even in the regions not covered by the gold electrode. In such conditions, very little light reaches the output facet, even when the device is not biased, forbidding any accurate absorption measurement. The only experimental data available is then the photocurrent measured in large-area devices.

Because the optical power in the fiber was kept constant at 3 mW when the wavelength was changed, it is possible to compare directly the different photocurrent curves to look at the variation in absorption with respect to wavelength. In both graphs, it can be seen that a reduction in wavelength causes the whole absorption curve to be displaced on the
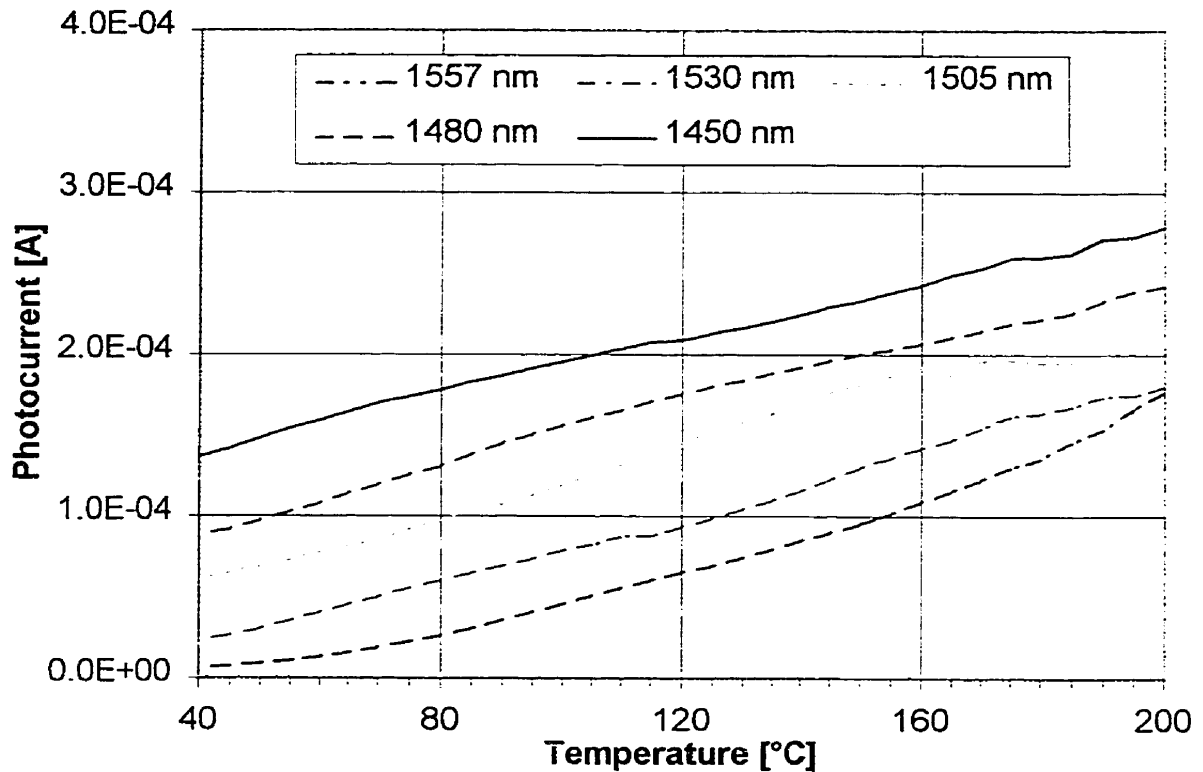
Fig. 4.12 – Photocurrent in Large-Area Device at Different Wavelengths, at 5 V

temperature axis towards lower temperatures. Thus, increasing the temperature in the device or reducing the wavelength have virtually the same effect on the absorption coefficient in the MQW. The main effect of raising the internal temperature is to reduce the band gap in the MQW, which impacts the absorption in the same way as increasing the photon energy. However, changing the applied voltage has a totally different impact on absorption, since this completely changes the shape of the curves, as can be observed by comparing figures 4.11 and 4.12.

Conclusion

Absorption measurements provide much information useful in itself, by indicating the respective effects of voltage, temperature and wavelength on the absorption occurring in the waveguide. These measurements also demonstrate that temperature has a great

influence in optoelectronic devices using electro-absorption. However, the most important utilization of this data is for the thermal modelling work presented in the next chapter.

Chapter 5
Thermal Modelling

The liquid crystal technique reveals only limited information about the temperature in the waveguide device. It gives the temperature and the location of the hottest point of the device surface, but tells nothing about the internal temperature or the temperature profile outside the hot spot. Another limitation is that it is not practical to study the behavior of the device close to conditions that lead to instantaneous blow-up, unless one accepts to sacrifice a large number of devices. Developing a thermal model of the waveguide device is perhaps the only way to circumvent these difficulties. The model's main parameters are the applied voltage and the optical power in the waveguide, from which a complete, three-dimensional temperature profile in the whole device can be produced.

In the beginning of this work, a simple model was constructed; it was implemented using the C++ programming language. This model used finite differences to compute the steady-state temperature profile along the length of the ridge of the narrow-electrode device for any combination of voltage and optical power. The simplicity of the model allowed fast calculations, however, it severely limited its versatility: the model could not be adapted to the large-pad geometry, nor could it include the effect of the laser heating in the hybrid configuration. Finally, the thermal conductivity had to be fixed at a constant value, and was not allowed to vary with temperature. To remedy these problems, a second model was developed using a commercial software package, *Algor*, which uses a Finite-Element Algorithm (FEA) to compute a three-dimensional temperature profile in a device of arbitrary geometry. The *Algor* model is more complex and calculations are much slower; however, it does not suffer any of the limitations of the original model.

The results obtained from the first model played an important role in understanding the thermal issues in the waveguide device at the early stage of this work; however, it serves no purpose to present them here. The predictions of the *Algor* model are more precise, comprehensive and reliable, and no additional information can be extracted from the earlier model.

Several thermal models of optoelectronic devices, almost exclusively laser diodes, can be found in the literature [14,15]. Their primary intent is often to study the facet degradation, usually the principal cause of failure of GaAs-based lasers. These models do not use a FEA to compute the temperature at the facet, but take into account many complex physical processes, such as absorption of light at the facet, carrier generation, recombination and transport, etc.; these processes are all potentially influenced by temperature. These models are thus inherently non-linear, that is, the temperature does not vary linearly with the power dissipated in the device. On the other hand, FEA are often used in thermal models of mechanical or electrical systems, and such models usually have fixed thermal loads and are linear. The originality of the model described here comes from two aspects. First, thermal issues have rarely been studied in optoelectronic devices other than laser diodes. Second, the model is non-linear for two reasons: the thermal conductivity strongly depends on temperature, and so does the heat generation in the device, since absorption changes with temperature. After an extensive literature search, no other instance of a non-linear thermal model of any optoelectronic device other than a laser diode has been found.

This chapter describes in detail the *Algor* model and explains how it is used to study thermal issues in the waveguide device. The modelling requires the knowledge of the thermal conductivity of the different semiconductor materials present in the device. Obtaining this data is not a trivial task, and the question is addressed in some depth. The modelling results are then presented and discussed. The final product of this analysis can be expressed conveniently by temperature maps that give the internal and surface temperatures on the chip for all combinations of voltage and photocurrent. The model

predictions are finally compared with the temperatures measured with the liquid-crystal technique, to assess the validity of the model.

5.1. Thermal Conductivity of Compound Semiconductors

The evaluation of the thermal conductivity of thin semiconductor layers is far from a trivial matter, and considerable efforts have been devoted to this problem by many researchers [18-26]. The thermal conductivity of compound semiconductors depends on the exact composition, doping and crystalline quality of the sample and also exhibits a strong dependence on temperature: this all contributes to complicate the measurements and their interpretation. Moreover, measuring the thermal conductivity of epitaxial layers requires elaborate experimental manipulation, unlike the case for the electrical conductivity. No measurement of the thermal conductivity has been carried out for this work; instead, the literature on the subject has been reviewed extensively to obtain the required information.

5.1.1. Thermal Conduction in Semiconductors

Phonons are mainly responsible for the conduction of heat in semiconductors [16,17]. Unlike the case of metals, the electronic contribution is negligible except in the case of very highly doped samples (less than 1% for $n = 10^{18}$ cm^{-3} in GaAs [18]). Let us now consider how phonons conduct heat. The heat flux in a solid is determined by the total crystal momentum of the phonon gas. The thermal resistivity of a crystal arises from the fact that phonons are scattered by impurities, sample surfaces or in collisions with other phonons. In a perfect crystal, phonon-phonon collisions are the only source of scattering. Consider the law of conservation of crystal momentum for a collision involving three phonons:

$$\mathbf{k_1} + \mathbf{k_2} = \mathbf{k_3} \qquad \{5.1\}$$

where the indices 1 and 2 denote the colliding phonons, and 3, the single phonon resulting from the collision. In this so-called **normal** process, the total crystal momentum is conserved in the collision, and the total crystal momentum of the phonon gas is unaffected. There exists however another class of processes, called **umklapp** processes, where a reciprocal lattice vector needs to be added to equation 5.1, because the sum of the k_1 and k_2 lies outside the first Brillouin zone.

$$\mathbf{k}_1 + \mathbf{k}_2 = \mathbf{k}_3 + \mathbf{G} \qquad \{5.2\}$$

Umklapp processes do modify the total crystal momentum of the phonon gas, and thus limit the thermal conductivity of a crystal. In order for umklapp processes to represent a significant fraction of all phonon collisions, there must be an important number of phonon with a crystal momentum magnitude of the order of $\frac{1}{2} |G|$, otherwise the sum of the crystal momenta in a collision would never lie outside the first Brillouin zone. This means that the temperature must exceed the Debye temperature of the crystal, that is, the temperature where all the normal modes of the crystal are excited. At lower temperatures, the umklapp processes are "frozen out", and the thermal conductivity increases rapidly. At high temperatures, the probability of any phonon to undergo an umklapp collision is roughly proportional to the total number of phonons, which is proportional to the absolute temperature, according to the Bose-Einstein distribution. The thermal conductivity should then be inversely proportional to the absolute temperature:

$$\sigma \propto T^{-n} \qquad \{5.3\}$$

where n is equal to one in the absence of collisions implying more than three phonons. In real semiconductor crystals, the exponent n varies between 1 and 2, indicating that higher-order processes are also present.

5.1.2. Effect of Composition

In the $In_{1-x}Ga_xAs_yP_{1-y}$ system, the thermal conductivity is known with good accuracy and confidence only for the binary compounds. The conductivity of ternary and quaternary can not be evaluated by means of simple interpolation, however. In fact, the random distribution of atoms of different elements in both the valence III and V sub-lattices represents fluctuations in the periodicity of the lattice and is the source of heavy phonon scattering. The thermal conductivity of ternary and quaternary compound semiconductors is then much lower than that of binary compounds, by a factor as large as 20. Experimental data is available in limited amounts on ternary compounds [19-22] but is very scarce on quaternary [19]. The fact that the crystalline quality of the grown samples and the exact doping affect measurements complicates the interpretation of the results. In the best case, the precision of the measured values of the thermal conductivity does not exceed 10%.

Because of the lack of experimental data, several authors have developed elaborate models to find the room-temperature conductivity of compound semiconductors in the InGaAsP system, namely, Abeles [24], S. Adachi [19,20] and W. Nakwaski [22]. Each model uses slightly different assumptions but yields similar, although not identical, results. The values of the thermal conductivity used in this work come from Adachi's model.

It is important to note that doping also affects the thermal conductivity of a semiconductor. The values reported usually concern samples not doped intentionally, with residual doping of the order of 10^{16} to 10^{17} cm^{-3}. It has been reported that each decade in doping concentration exceeding 10^{15} cm^{-3} can reduce the conductivity by 7 to 8 % in Ge or GaAs [25]. However, the active region of the waveguide device is undoped, and most other materials composing the waveguide device are only lightly or moderately doped (less than 10^{18} cm^{-3}). For simplicity, the effect of doping has been neglected in the

model, since the changes induced on the conductivity are of the order of the uncertainty on its value.

5.1.3. Temperature Dependence of the Thermal Conductivity

The discussion up to this point was limited to the room-temperature value of the thermal conductivity. However, as mentioned earlier, the conductivity is strongly dependent on temperature. Since temperatures as high as 300°C are found in the model, this dependence can not be neglected. Experimental data on binary III-V semiconductors suggest that they all obey equation 5.3 in the temperature range 150 – 600 K; the exponent n is 1.55 for InP, 1.25 for GaAs, 1.20 for InAs and 1.30 for GaP [19]. The thermal conductivity can then be expressed as

$$\sigma = \sigma_0 \left(\frac{T}{T_0}\right)^{-n} \qquad \text{for } 150 \text{ K} < T < 600 \text{ K} \qquad \{5.4\}$$

where σ_0 is the conductivity at room temperature T_0. Adachi [19] and others [14] go further and suggest that the conductivity of ternary and quaternary semiconductors follows the same law, and suppose that the exponent should lie in the range 1.20 – 1.55. The only experimental data found on the dependence of the conductivity on temperature of ternary alloys concerns the InGaAs system [23]. The conductivity was measured at 300, 500 and 700 K, and the results indicate that the dependence is not as strong as Adachi suggests, but that the exponent in equation 5.4 should rather be approximately 0.8. Because of the very limited quantity of data shown, it was decided instead to follow Adachi's suggestion and to use an exponent of 1.375 for InGaAsP, midway between that of GaAs and InP for the ternary and quaternary alloys found in the device. The largest error made on the thermal conductivity, if the actual exponent was 0.8, would be 50% at 600 K, and would lead to an overestimation of the internal temperature. The overall impact on the modelling should not be very important, however, since only a small

portion of the device is composed of quaternary semiconductor. The model predictions would then constitute a worst-case scenario, useful from a reliability point of view.

Although only a limited amount of experimental data is available on the thermal conductivity of compound semiconductors, all the necessary information has been obtained, and it is now possible to proceed with the modelling itself.

5.2. Description of the Finite-Element Model

The first step in creating a thermal model with the software *Algor* is to draw the model, using the computer-assisted drawing program. The individual elements are defined by drawing a fine mesh over the device model, and the different materials are specified by assigning different colors to the drawing elements. The next step is to specify the thermal loads, that is, how heat is generated and extracted from the device. Thermal loads can exist in the form of heat generated inside a given volume, fixed-temperature boundaries (corresponding to a perfect heat sink) and convection boundaries. *Algor* then compiles the model and runs the FEA program. The result of the analysis consists of the temperature distribution in the device; it can be displayed on the screen as a map of the device, where temperature is given by a color scale, or exported to another software, such as a spreadsheet application, for further analysis.

5.2.1. Fundamentals

The equation describing heat conduction in a non-moving solid is [27]

$$\nabla \cdot (\sigma \ \nabla T) - \rho \ C_p \frac{dT}{dt} = q \qquad \{5.5\}$$

where σ is the thermal conductivity, a second-order tensor in the most general case, ρ is the density, C_p is the specific heat and q is the power dissipated in the form of heat per unit volume. Without further assumptions, all quantities can vary with position and

temperature at this stage. This discussion is limited to the case where all materials are isotropic; furthermore, only a steady-state solution is needed. However, the model is not homogeneous, since several different materials are present. The temperature dependence of both the thermal conductivity and the heat generation term also needs to be taken into account. Equation 5.5 then becomes

$$\nabla \cdot \left(\sigma \left(x, y, z, T \right) \nabla T \right) = q \left(x, y, z, T(x', y', z') \right) \qquad \{5.6\}$$

In this model, the heat generation term is a result of the passage of a photocurrent generated by the absorption of light; it is given by

$$q = \frac{dP}{dv} = \frac{V \, dI}{wt \, dx} = \frac{V}{wt} \left(-\eta \frac{dL}{dx} \right) = -\frac{V\eta}{wt} \left(\frac{-\alpha(V,T)\,L(x)\,dx}{dx} \right)$$

$$q \left(x, y, z, T(x', y', z') \right) = \frac{V\eta\alpha(V,T)L(x)}{wt} \qquad \{5.7\}$$

where v denotes a volume, V is the voltage, I the photocurrent, α (V, T) is the absorption coefficient, w and t are the active layer width and thickness respectively, η is the responsivity, which is 1.25 A/W at 1557 nm, as explained in chapter 4, and $L(x)$ is the optical power at a distance x from the waveguide entrance. This assumes that heat is generated uniformly in the cross-section of the active layer; this is not the exactly the case in the real device, since the optical mode does not have a uniform intensity over the active (and guiding) layer. This approximation has little impact on the model, since only a small fraction of the temperature gradient is found in the active layer. Since the light reaching distance x is determined by the total absorption occurring before x, both $L(x)$ and q (x,y,z) are affected by the entire temperature distribution, $T(x',y',z')$, and not only by the local temperature at point (x,y,z); this explains the presence of $T(x',y',z')$ in the argument for the heat generation term q in equation 5.6.

The reason to use a FEA to solve for the temperature distribution, $T(x,y,z)$, is that it is impossible to solve equation 5.6 analytically in a complex geometry, such as in the

waveguide device. Instead, the model needs to be broken down in small pieces having a simple geometry, such as a brick shape, where this equation can be solved easily. The temperature distribution in each element must satisfy boundary conditions to ensure that both temperature and heat flow are continuous across the boundaries, that is,

$$T_i(x,y,z) = T_j(x,y,z)$$

$$\sigma_i \frac{\partial T_i(x,y,z)}{\partial n} = \sigma_j \frac{\partial T_j(x,y,z)}{\partial n} \qquad \{5.8\}$$

across the boundary between any pair of elements i and j; n is a vector normal to the boundary surface. If the two elements are made of different materials, σ_i can differ from σ_j. Once equation 5.6 has been solved for all elements and the boundary conditions 5.8 are satisfied at all boundaries, the temperature profile in the whole device is obtained.

5.2.2. Non-Linearities and Inhomogeneities

The model is inhomogeneous and non-linear because of the temperature and position dependence of both the thermal conductivity σ and of the heat generation term q. The fact that the model is inhomogeneous poses no important problem, since *Algor* offers the possibility of considering multiple materials with different thermal properties. The non-linearity can be put in evidence by further developing equation 5.6 and is more complicated to treat. To simplify this argument, let us forget about the fact that thermal conductivity explicitly depends on position.

$$q(x,y,z,T)$$
$$= \nabla(\sigma(T)\nabla T)$$
$$= \nabla\sigma(T)\nabla T + \sigma(T)\nabla^2 T \qquad \{5.9\}$$
$$= \frac{d\sigma}{dT}(\nabla T)^2 + \sigma(T)\nabla^2 T$$

The procedure employed to treat the dependence of q on the temperature is to run multiple iterations of the model; at the beginning of each iteration, the heat generation along the waveguide is calculated based on the most recent temperature profile. This is explained further in a subsequent section. The temperature dependence of the thermal conductivity is approached differently. Although *Algor* does allow the conductivity to vary with temperature, this requires multiple iterations from the thermal processor, on top of the iterations required to account for the heat generation. The whole process then becomes very long and tiresome. An alternate, simpler and more elegant approach is to use a technique called the **temperature transformation** [27], first used by Kirchhoff. This technique has frequently been used for other thermal modelling work [14,15].

The technique requires an auxiliary variable, the transformed temperature, θ, to replace the real absolute temperature, T. The two are related by the equation

$$\theta = T + \frac{1}{\sigma_0} \int_{T_0}^{T} \sigma\,(T)\,dT \qquad \{5.10\}$$

where σ_0 is the thermal conductivity at temperature T_0. This allows a transformed temperature profile $\theta\,(x,y,z)$ to be computed using a constant conductivity σ_0. This profile is then converted back to absolute temperature with the reciprocal transformation. Since the conductivity of the semiconductor follows the law given in 5.4, the reciprocal transformation is

$$T = T_0 \left[\frac{(1-n)}{T_0} \left(\theta - \frac{n\,T_0}{n-1} \right) \right]^{\frac{1}{1-n}} \qquad \{5.11\}$$

for $n \neq 1$. Although this technique has been designed for homogeneous solids, it will give correct results in the case of a stack of different materials, if within each material the conductivity does not depend on position and if the temperature dependence of the conductivity is the same for all materials, that is, the exponent n is the same. For this to be true, the boundary conditions stated in equation 5.8 must be satisfied across all inter-

faces. Since equation 5.11 does not include any reference to σ, T will be continuous across all boundaries, as a consequence of the continuity of θ guaranteed by the fact that θ (x,y,z) is a solution of equation 5.6. The heat flow across a surface, to which $\mathbf{n}$ is a normal unit-length vector, is

$$-\sigma \, \nabla T \cdot \mathbf{n}$$

$$= -\sigma \, \nabla\theta \cdot \mathbf{n} \left(\frac{dT}{d\theta} \right)$$

$$= -\left[\sigma_0 \left(\frac{T}{T_0} \right)^{-n} \right] \nabla\theta \cdot \mathbf{n} \left[\frac{1-n}{T_0} \left(\theta - \frac{n\,T_0}{n-1} \right) \right]^{\frac{n}{1-n}} \qquad \{5.12\}$$

$$= -\left(\sigma_0 \nabla\theta \cdot \mathbf{n} \right) \left[\frac{1-n}{T_0} \left(\theta - \frac{n\,T_0}{n-1} \right) \right]^{\frac{-n}{1-n}} \left[\frac{1-n}{T_0} \left(\theta - \frac{n\,T_0}{n-1} \right) \right]^{\frac{n}{1-n}}$$

$$= -\sigma_0 \nabla\theta \cdot \mathbf{n}$$

This shows that the heat flow obtained from the transformed temperature is identical to the real heat flow. Since θ (x,y,z) is a solution of equation 5.6 when σ is constant, the heat flow is continuous across any interfaces, even if the thermal conductivity itself differs on both sides of it.

This technique requires using a single exponent n to describe the thermal conductivity of all the materials present in the model. A value of 1.4 was chosen, since it lies between the exponent associated with InP (1.55) and the value of 1.375 suggested by Adachi for InGaAsP. This approximation is not expected to have a significant impact on the results of the modelling, since the temperature transformation is not much affected by such small variations of n.
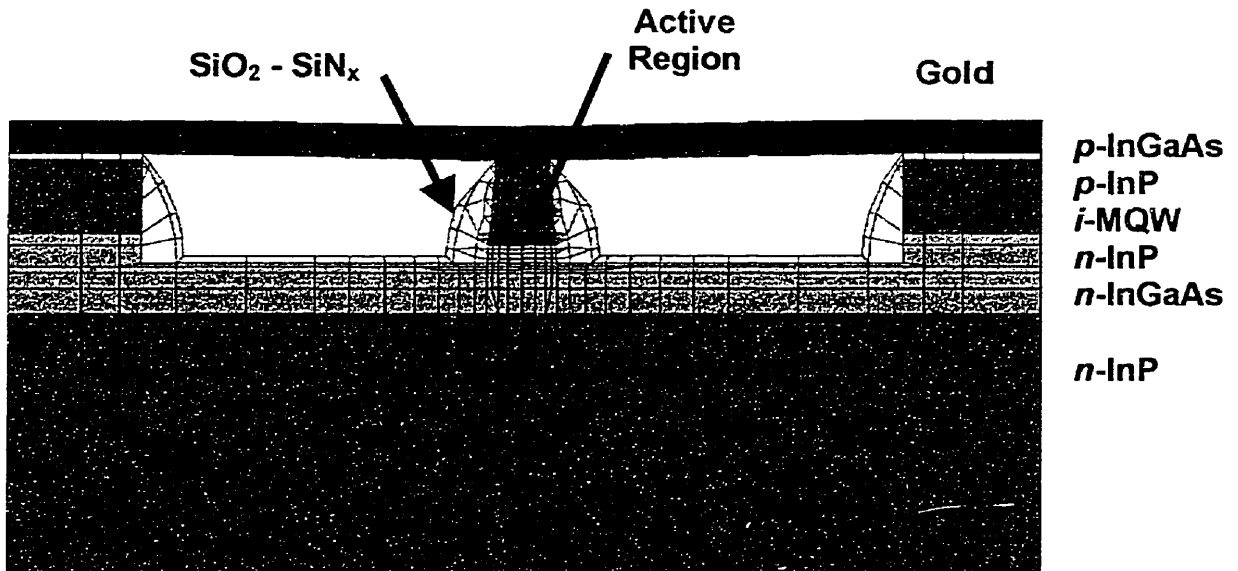
Fig. 5.1 – 2-D Model of the Waveguide Device
This figure shows a cross-section of the waveguide device, with an enlarged view of the ridge area: the gold pad is seen on top, forming a bridge over with the empty region shown as a white area in the center. Note that only one half of the device is modelled, because of symmetry.
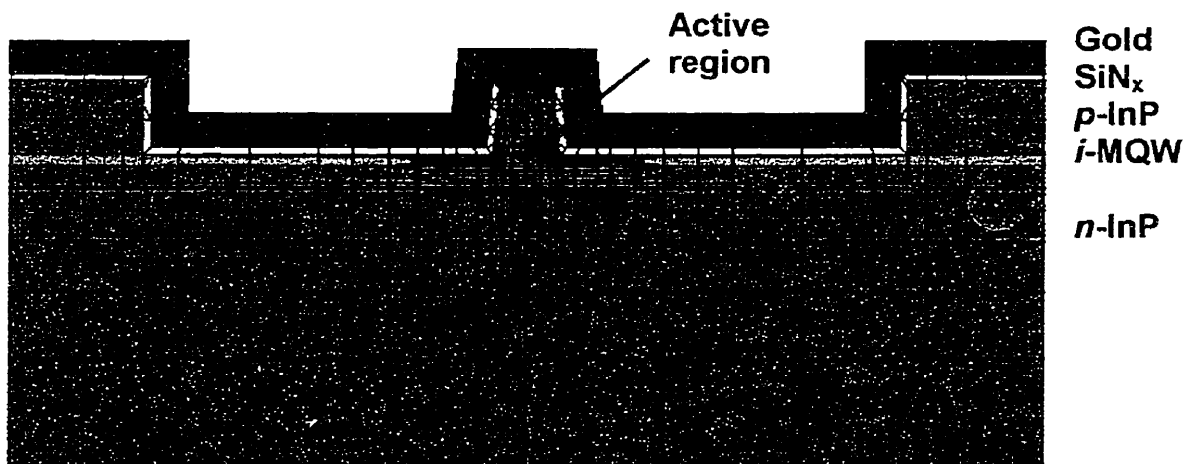
Fig. 5.2 – 2-D Model of the Laser Diode
This figure shows a cross-section of the laser diode, with an enlarged view of the ridge area: the conformal gold layer is seen on top. Note that only one half of the device is modelled, because of symmetry.
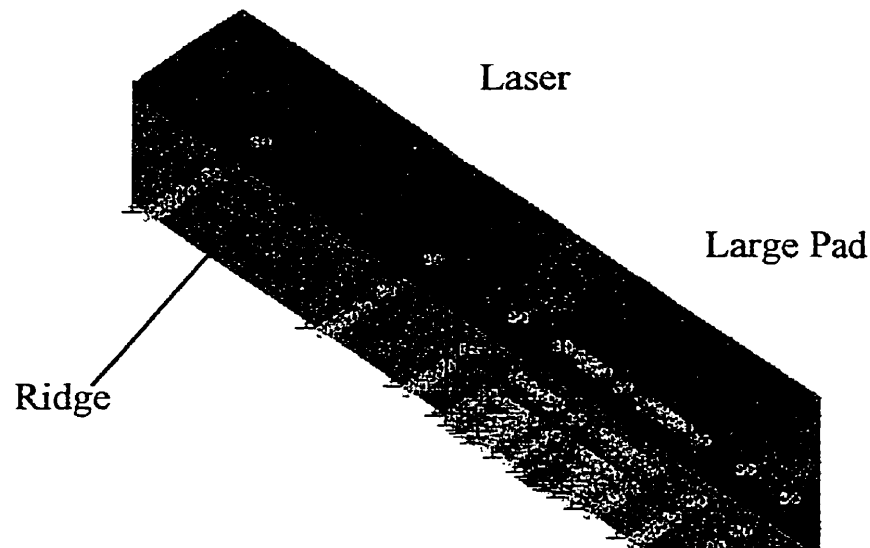
Fig. 5.3 – **Full 3-D Model of the Hybrid Device**
The laser pad can be seen on the top left area, and the pad covering the waveguide device
on the bottom-right. Only one half of the device is shown, with the ridge seen on the front side

5.2.3. Structure of Model

The first step in building a three-dimensional model of a waveguide device is to make a model of its cross-section, showing all the materials composing the device, including the top p-side gold electrode, dielectrics (SiO_2 and SiN_x) and silver epoxy as a soldering layer underneath the device. The plane model is shown in fig. 5.1; the large white areas in the middle are air gaps, over which lie the metal, forming a bridge. Each color denotes a different material. The dark blue layer inside the ridge is the active region, where the heat is generated. To account for the heat sink under the device, the bottom surface of the device is defined as a fixed-temperature surface, either at 25 or 30°C, depending on the type of device. The other device surfaces are thermally insulated, meaning that the heat flow is zero across these surfaces. In the narrow-electrode device model, the gold layer was deleted everywhere except on the very top of the ridge.

To create the three-dimensional model, the plane representation of the device is copied several times along the length of the waveguide, at intervals that define the length of the elements along the waveguide. The smallest element dimension is 2.5 μm, near the

Table 5.1 – Thickness of the Layers Composing the Waveguide Device

Material	Thickness [μm]
p-side gold electrode	1.0
SiN$_x$	0.2
SiO$_2$ (width)	1.0
p$^+$-InGaAs cap	0.2
p-InP	2.0
i-MQW	0.35
n-InP (in mesa)	0.55
n-InP (under mesa)	1.55
n$^-$-InGaAs	0.2
n$^+$-InP (substrate)	135
Silver epoxy	10

Table 5.2 – Room-Temperature Thermal Conductivities

Material	Conductivity [W/K.m]
InP	67.0 [20] †
In$_{.53}$Ga$_{.47}$As	4.77 [20]
MQW (InGaAsP)	4.91 [20]
Gold	318 [28]
SiN$_x$	1.60 [30]
SiO$_2$	0.138 [28]
Liquid crystal (benzene)	0.140 [29]
Silver epoxy	4 ‡

† The number in brackets indicate the reference from which comes the data.
‡ Obtained from measurements done at Nortel

front edge of the electrode, where the optical power is the greatest and where the highest temperature is likely to be found. Far from the front edge of the electrode, the elements are longer, up to 70 μm, since temperature is expected to be lower and the precision does not have to be as high. On the regions past the edges of the electrode, the gold layer is simply deleted. A second plane model of the laser cross-section was created, with a different material definition, to be included in the hybrid device model. The laser cross-section is shown in figure 5.2. Finally, the three-dimensional model is presented in figures 5.3, which shows an enlarged view of the junction region between the laser and the waveguide device. Tables 5.1 and 5.2 give the thickness of each layer and the room-temperature thermal conductivities of the materials present in the device.

Three versions of the model exist: the large-pad hybrid waveguide device, the discrete large-pad device and the discrete narrow-electrode device. Hybrid narrow-electrode devices were not modelled, since this configuration was never used in experiments.
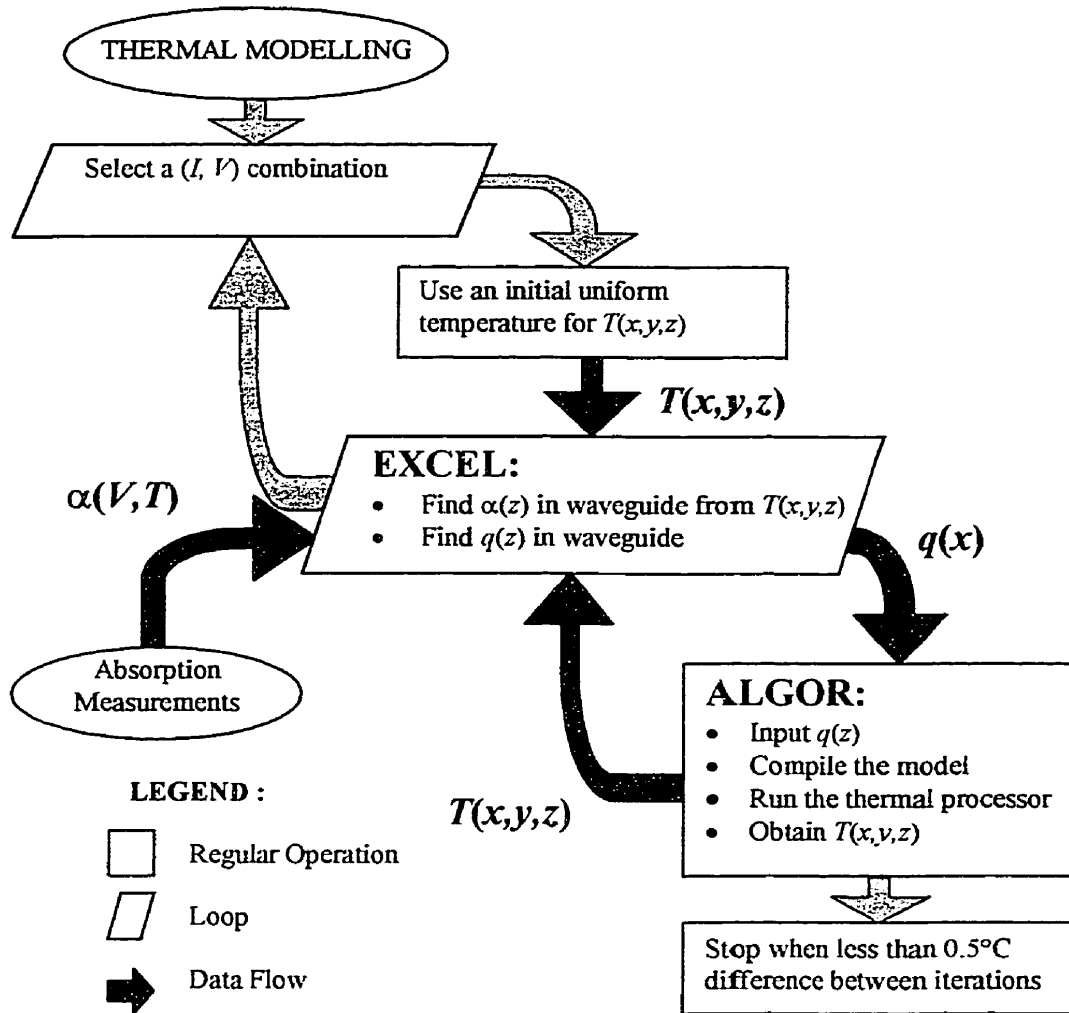
Fig. 5.4 – Block Diagram Showing the Procedure Followed for Thermal Modelling

5.3. Procedure

Multiple iterations are required to obtain the final temperature profile in the device. Each iteration involves two steps. The first one is to find how light is absorbed along the waveguide; this requires that the waveguide be divided into many "cells" having the length of the elements in the model. The absorption coefficient can be different in each cell, and is determined by the temperature inside the cell and the voltage; it is however assumed to be constant within one cell. An *Excel* spreadsheet computes the optical

Table 5.3 – **Effect of Liquid Crystal Thickness in 2-D Model**

Conditions [mW/μm]	LC Thickness [μm]	Max. Temp. in MQW [°C]	Max. Temp. at Gold Surface [°C]	Max. Temp. at LC Surface [°C]	Difference †
0.65	0	47.8	38.0	-	-
0.65	2	47.8	38.0	37.6	- 3 %
0.65	10	47.8	38.0	35.9	- 16 %
0.65	50	47.8	38.0	32.0	- 46 %

† Calculated as follows: $(T_{LC} - T_{surf.}) / (T_{surf.} - 25°C) \times 100 \%$

Table 5.4 – **Effect of Liquid Crystal in 3-D Model**

Conditions	LC Thickness [μm]	Max. Temp. in MQW [°C]	Max. Temp.at Gold Surface [°C]	Max. Temp. at LC Surface [°C]	Difference †
8 V, 5 mA	0	48.9	34.8	-	-
8 V, 10 mA	0	123	58	-	-
8 V, 15 mA	0	250	94	-	-
8 V, 5 mA	10	49.0	34.8	32.1	- 28 %
8 V, 10 mA	10	123	58	45	- 39 %
8 V. 15 mA	10	250	94	61	- 48 %

† Calculated as follows: $(T_{LC} - T_{surf.}) / (T_{surf.} - 25°C) \times 100 \%$

absorption and the heat generation in each cell, using the absorption data presented in chapter 4; an example of the content of the spreadsheet is presented in appendix E. Since absorption varies with temperature, a uniform temperature profile is used initially. The heat generated in each cell is subsequently entered in *Algor*. The next step is to run *Algor* to obtain the temperature profile in the device. This profile is then used to correct the absorption and the heat generation in each cell. The process is repeated until a steady-state, self-consistent profile is obtained (that is, when the temperature difference from one iteration to the next does not exceed 0.5°C at any location). This typically requires 5 to 10 iterations. The procedure is summarized in a block diagram in figure 5.4.

There are some voltage-current combinations for which the iterative process never converges; instead, successive iterations always yield increasing temperatures, meaning that
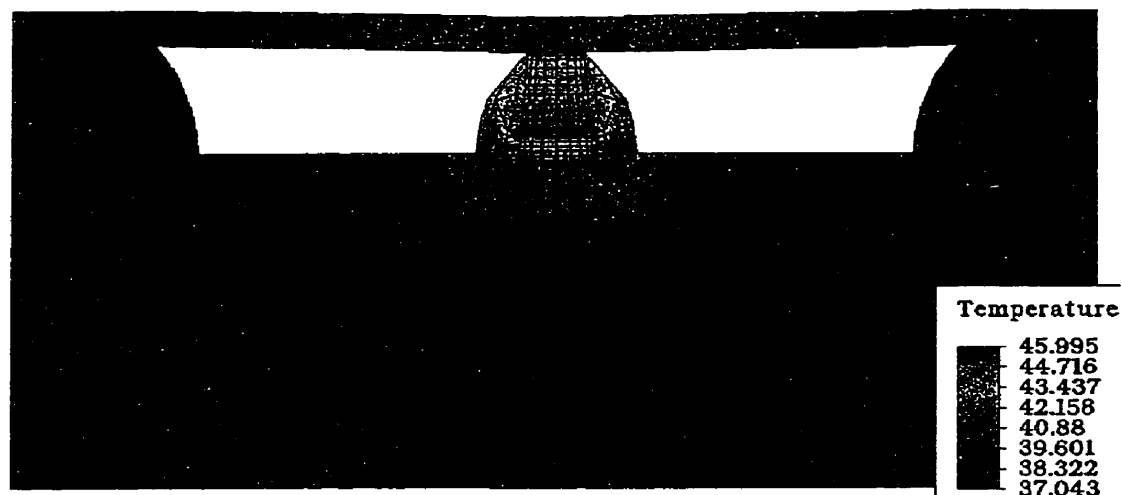
Fig. 5.5 – Temperature Profile in the Waveguide Device
This figure shows the cross-section of the waveguide device; the temperature is represented by a color scale, red being the hottest, blue the coldest.

no stable solution exist for the heat-conduction equation under such conditions. When this happens, the process is stopped when the temperature exceeds 300°C, because no absorption data is available at that temperature. This situation corresponds to thermal runaway, which leads to the destruction of the device; this is further discussed in section 5.5.

5.4. Results

For further reference, all numerical data obtained from thermal modelling has been placed in appendix F.

5.4.1. Effect of Liquid Crystal Thickness on Temperature Measurements

A question raised by the use of liquid crystals to measure the surface temperature is the possibility that its presence on the chip could affect the temperature distribution, and hence, bias the measurements. If the LC is a good thermal conductor, it would help to dissipate the heat away from the hot spot, and the temperature measured would be lower than the actual temperature on the bare device surface. On the other hand, if the LC is a
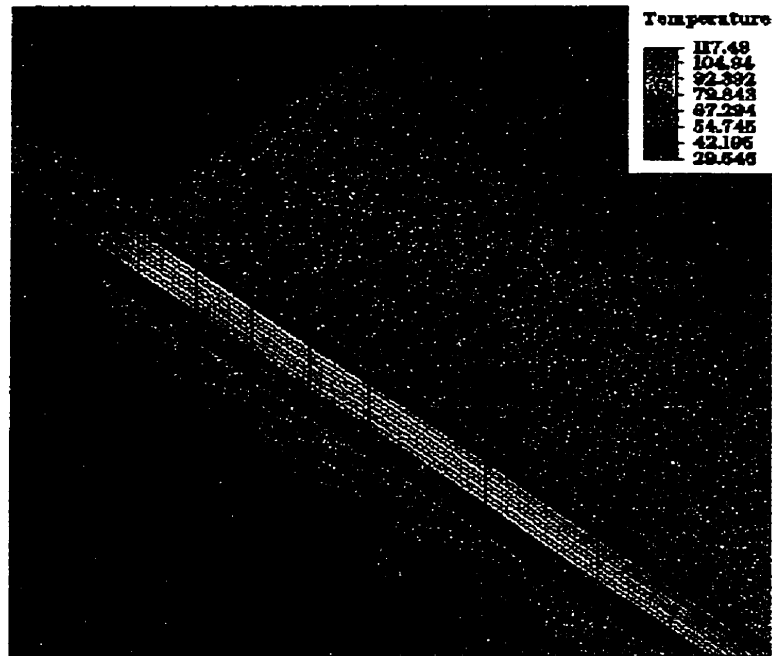
Fig. 5.6 – **Temperature Profile in the Hybrid Device**
This figure shows the junction between the waveguide device and the laser;
the temperature is represented by a color scale, red being the hottest, blue the coldest.

thermal insulator, there is a possibility that the temperature at the surface of the LC layer differs significantly from the surface temperature. This could again bias the measurements, because the full thickness of the LC layer must exceed the transition temperature in order to observe the transition, and the measured temperature corresponds to the temperature on the surface of the LC. To gain some insight on this issue, a LC layer was added to the model.

This was accomplished using different absorption characteristics (measured on wafer R2-1393) and with an earlier version of the model where the conductivity was assumed to remain constant as temperature changed. Thus, the modelling results presented in this section are lower than those given in subsequent sections; however, the comparison between the cases where the LC is present or absent is still valid. The LC was included in the model by adding one more layer on top of the gold pad. The surface of the LC follows a circular arc, so that the thickness is maximum over the ridge and zero at the edges of the device. The thermal conductivity of the LC is not known exactly, but since

it is an organic compound, the value for benzene was used, on the suggestion of the manufacturer. Because the LC is a good thermal insulator, the effect of air convection on top of the LC layer could be significant and was added to the model (ambient temperature 25°C, convection coefficient 130 W/K.m^2).

The results shown in table 5.3 come from a plane (two-dimensional) model. Such a model is easier to modify and faster to run, and was used to investigate the effect of the LC thickness on the surface temperature. The effect of the LC was also studied with the three-dimensional model using a single value of the thickness, 10 μm; the results are presented in table 5.4. The heat sink temperature was set at 25°C.

Later, the modelling work was repeated without the effect of air convection on top of the LC layer. It was found that the effect of convection is negligible.

5.4.2. Large-Pad Devices

The absorption measured on wafer R2-1444 was used for the modelling of the large pad, and the heat sink temperature was set at 30°C. Temperature profiles were obtained at 5, 6, 7, 7.5, 8 and 9 V. More accurate data is needed in the 7 – 8 V range for the activation energy experiment, which is described at the end of this chapter; this justifies the additional set of data acquired at 7.5 V. At each voltage, the photocurrent was successively set at all values between 4 mA to the thermal runaway point (18 mA at the most), with a 2 mA step (1 mA near the runaway point). An example of a temperature profile in the cross-section of the waveguide device is shown in figure 5.5. A typical three-dimensional temperature profile is presented in figure 5.6, which shows an enlarged view of the region between the waveguide device and the laser. The simulations were carried out twice, for both discrete and hybrid devices. The results are presented in two different ways. The temperature maps in figures 5.7 and 5.8 show the temperature using a color scale for all combinations of voltage and photocurrent. Red denotes the hottest temperature and blue, the lowest. The two maps give the peak temperature found in the
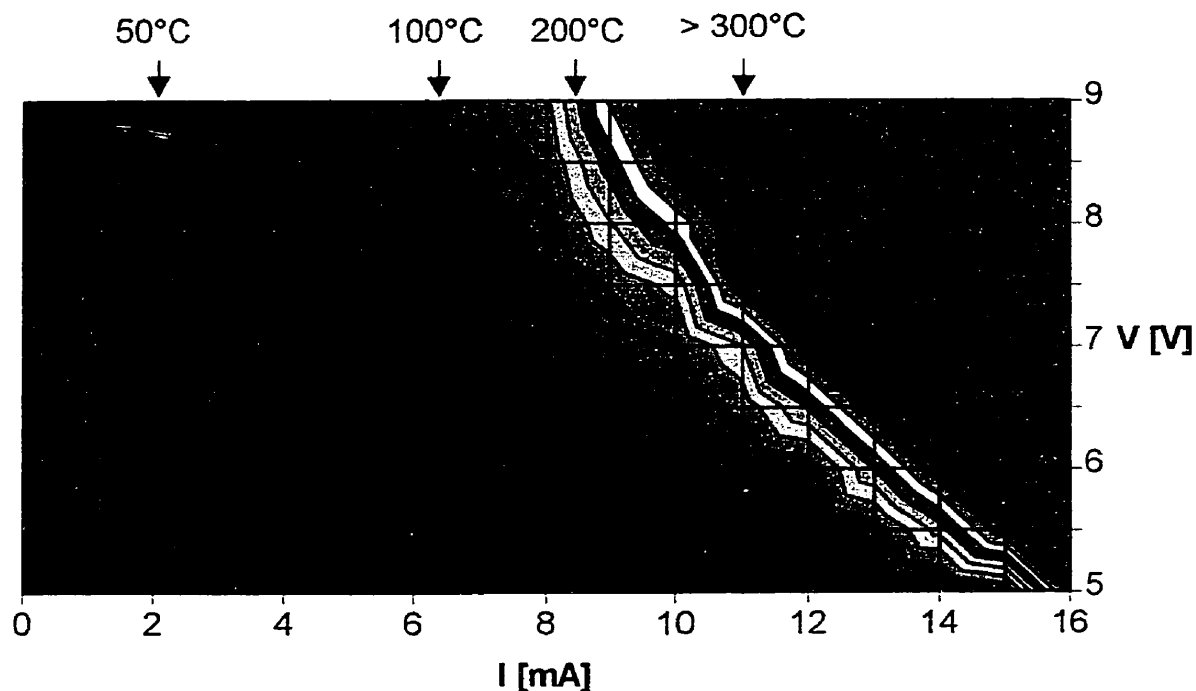
Fig. 5.7 – Temperature Map for the Hybrid Case
This map gives the peak temperature in the active region under the large pad,
as a function of voltage and photocurrent. Isothermic lines are spaced by 25°C.

active region of hybrid and discrete devices, respectively. Note that *Excel* uses linear interpolation to create a "continuous" graph from the discrete set of data, which explains the "jagged" appearance of the isothermic lines. Figure 5.9 compares the peak temperature in the active region, obtained from both the discrete and the hybrid device models, in a conventional graph form.

It is possible that the exact size of the elements along the ridge could influence the outcome of the modelling, particularly under conditions where the absorption in the waveguide is very large. This is a consequence of the fact that, under such conditions, most of the light is absorbed over a short length of the waveguide, in the first two or three cells. Under such conditions, the discrete nature of the model could lead to erroneous predictions. To investigate this, the model was modified by elongating the first four elements in the direction parallel to the waveguide, from 2.5 to 5.0 μm. The maximum temperatures found in both cases are compared in table 5.5.
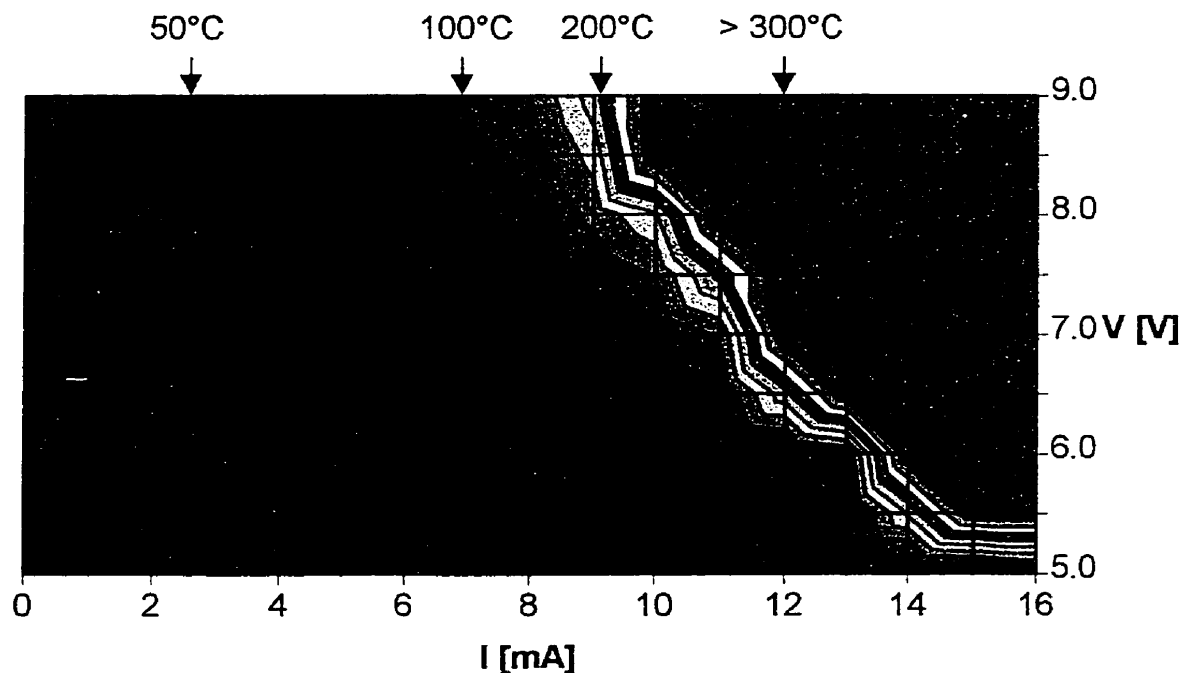
Fig. 5.8 – Temperature Map for the Discrete Case
This map gives the peak temperature in the active region under the large pad,
as a function of voltage and photocurrent. Isothermic lines are spaced by 25°C.

On figure 5.10, the thermal modelling data is compared to the experimental data obtained with the liquid-crystal technique on samples from wafer R2-1444. The graph shows the peak surface temperature, since this is the only information given by the experiments.

5.4.3. Narrow-Electrode Devices

A similar investigation has been carried out on narrow-electrode devices. As mentioned earlier, this device has not been designed to handle large heating, thus, the temperatures in this device are expected to be significantly higher than on the large pad for identical voltage and photocurrent. Six values of the voltage have been used, ranging from 4 to 9 V, with photocurrents of 2 to 16 mA, with a 2 mA step. The heat sink temperature was set at 25°C, to compare the modelling results with the liquid-crystal measurements carried out on narrow-electrode devices.
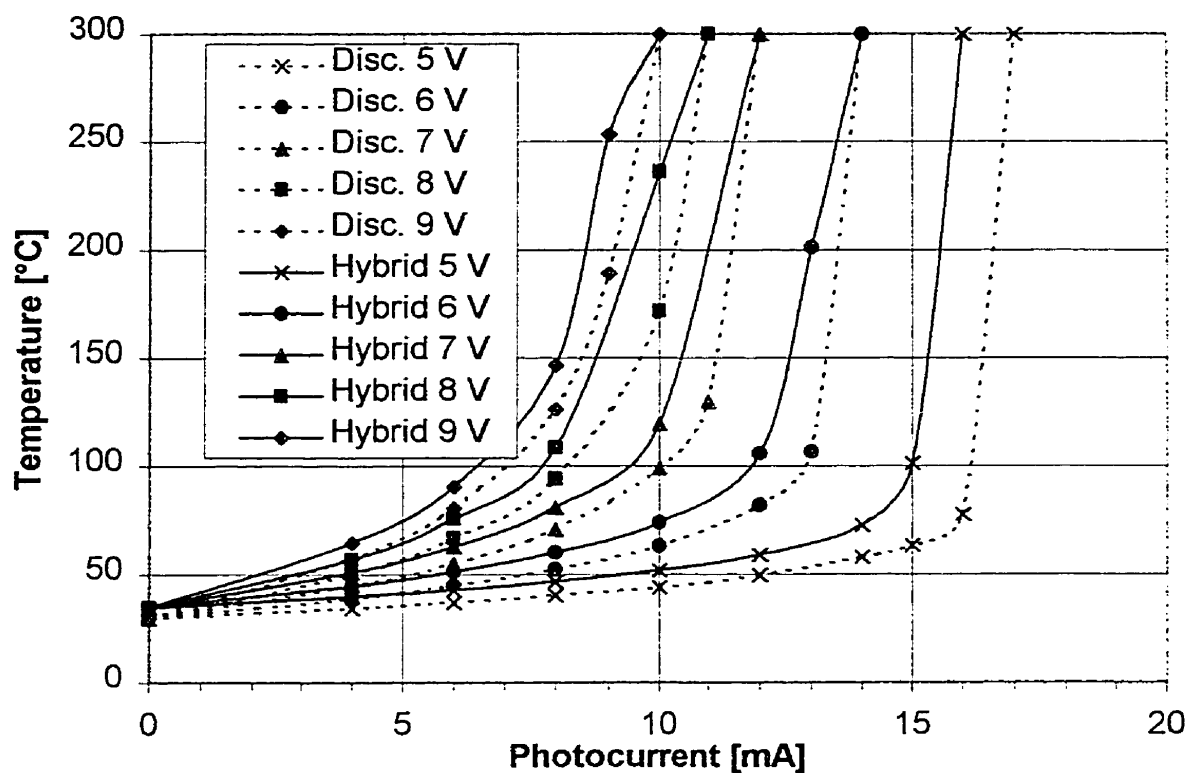
Fig. 5.9 – Temperature in Active Region under Large Pads

Figure 5.11 and 5.12 give the peak temperature found in the MQW, respectively in a temperature map and in a standard graph. Figure 5.13 compares the model predictions (surface temperature) with the liquid crystal measurements. The experimental values shown are averages of the temperatures measured on all devices originating from wafer R2-1444.

5.4.4. Comparison Between Large Pads and Narrow Electrodes

The last set of modelling results compares the temperature on a large-pad and a narrow-electrode device, to quantify the improved heat dissipation of the large pad. Since the heat sink temperature in the former data is 30°C for the large pad and 25°C for the narrow electrode, a direct comparison is not possible. New modelling data was obtained for
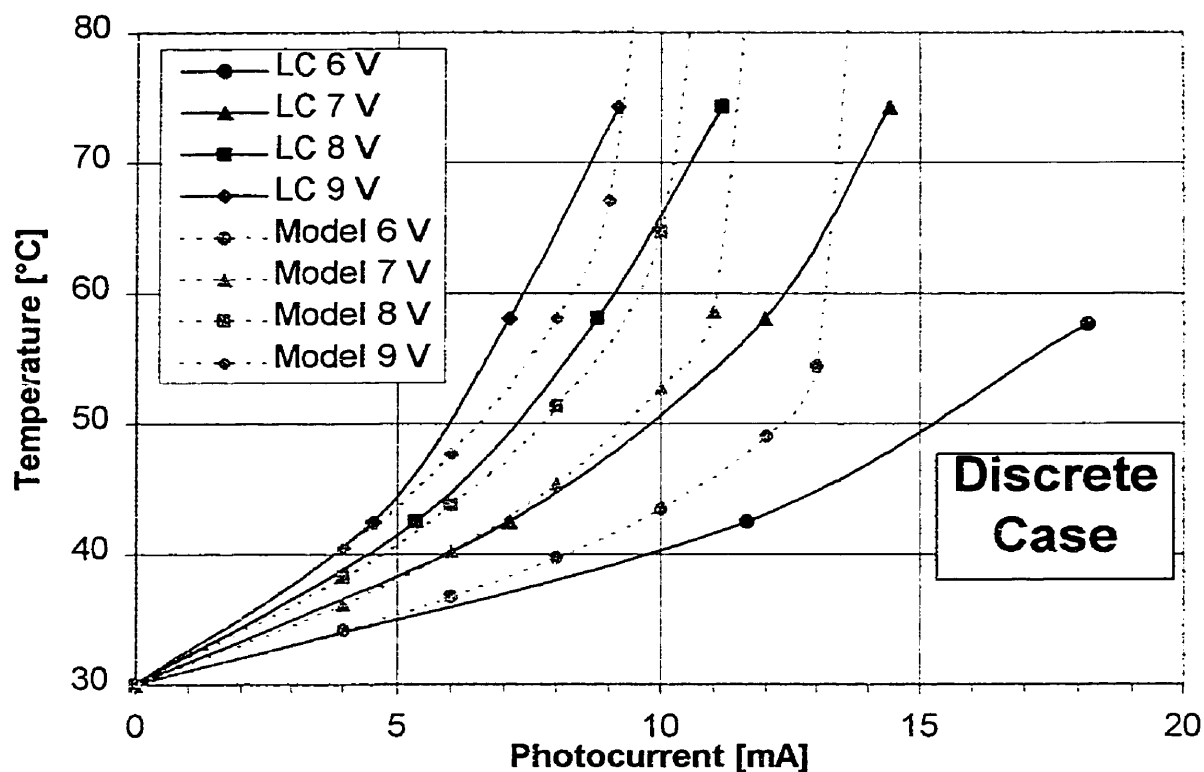
Fig. 5.10 – **Comparison of Experimental and Modelling Results on Large-Pad Devices**
This graph compares the peak surface temperature obtained from the liquid-crystal technique
and from the model on large pads of discrete devices.

Chart legend:
- LC 6 V
- LC 7 V
- LC 8 V
- LC 9 V
- Model 6 V
- Model 7 V
- Model 8 V
- Model 9 V

Y-axis: Temperature [°C] (30 to 80)
X-axis: Photocurrent [mA] (0 to 20)

Discrete Case

Table 5.5 - **Effect of Element Length along the Ridge**

Conditions	Optical Power [mW]	MQW Temperature [°C]			Surface Temperature [°C]		
		2.5 μm	5.0 μm	Diff. [%]	2.5 μm	5.0 μm	Diff. [%]
8 V, 4 mA	3.22	50.3	50.3	0.1	38.2	38.2	0.1
8 V, 6 mA	4.82	66.6	66.4	0.2	43.7	43.7	0.1
8 V, 8 mA	6.42	94.2	93.4	0.8	51.3	51.2	0.3
8 V, 10 mA	8.02	171.6	166.7	2.9	64.7	56.4	12.9
8 V, 12 mA	8.81	> 300	> 300	0.0	> 100	> 100	0.0

the narrow electrode at 30°C and 8 V, and is plotted in figure 5.14, along with the large
pad data.
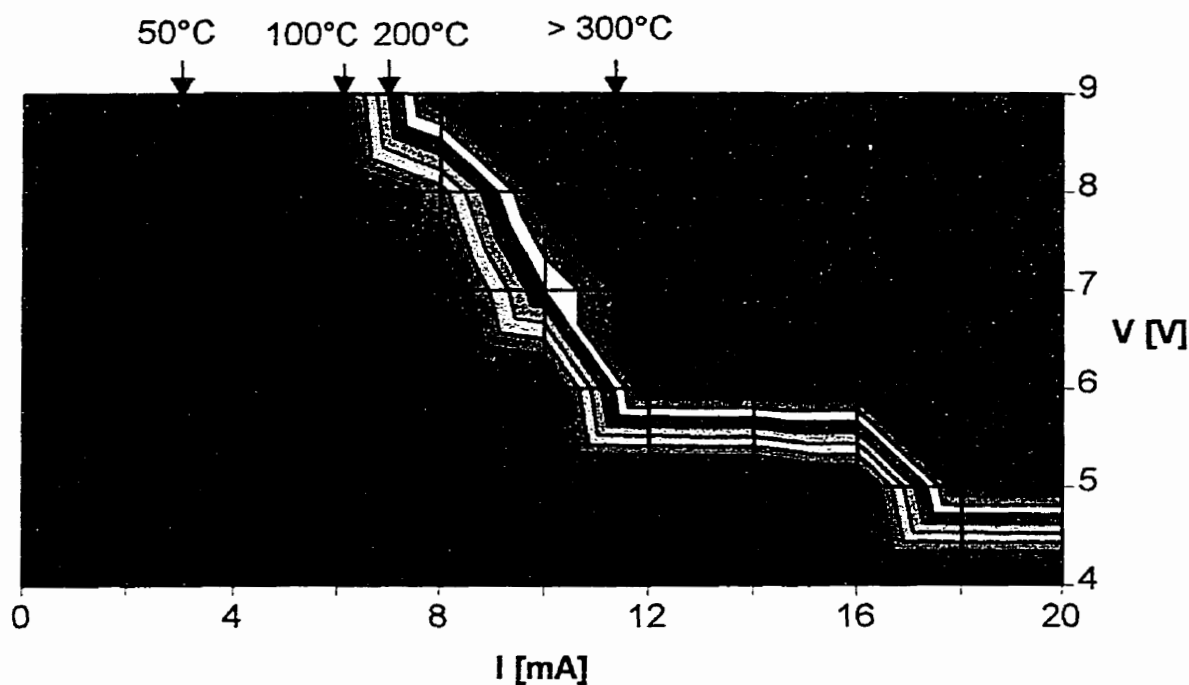
Fig. 5.11 – Temperature Map for Narrow-Electrode Devices
This map gives the peak temperature in the active region under large pads,
as a function of voltage and photocurrent. Isothermic lines are spaced by 25°C.

5.5. Discussion

A temperature map is a direct and very informative way of presenting the results of the modelling; the respective influence of photocurrent and voltage on the peak temperature can clearly be seen on this kind of graph. The isothermic curves give the set of conditions that lead to the same temperature; therefore, once one sets a maximum temperature ensuring the safe operation of the device, the maximum (I, V) conditions permissible can be established from such a map.

The model reveals that there are combinations of photocurrent and voltage that lead to thermal runaway, which can cause damage and even destruction of the device. The thermal runaway occurs because of the temperature dependence of the absorption co-
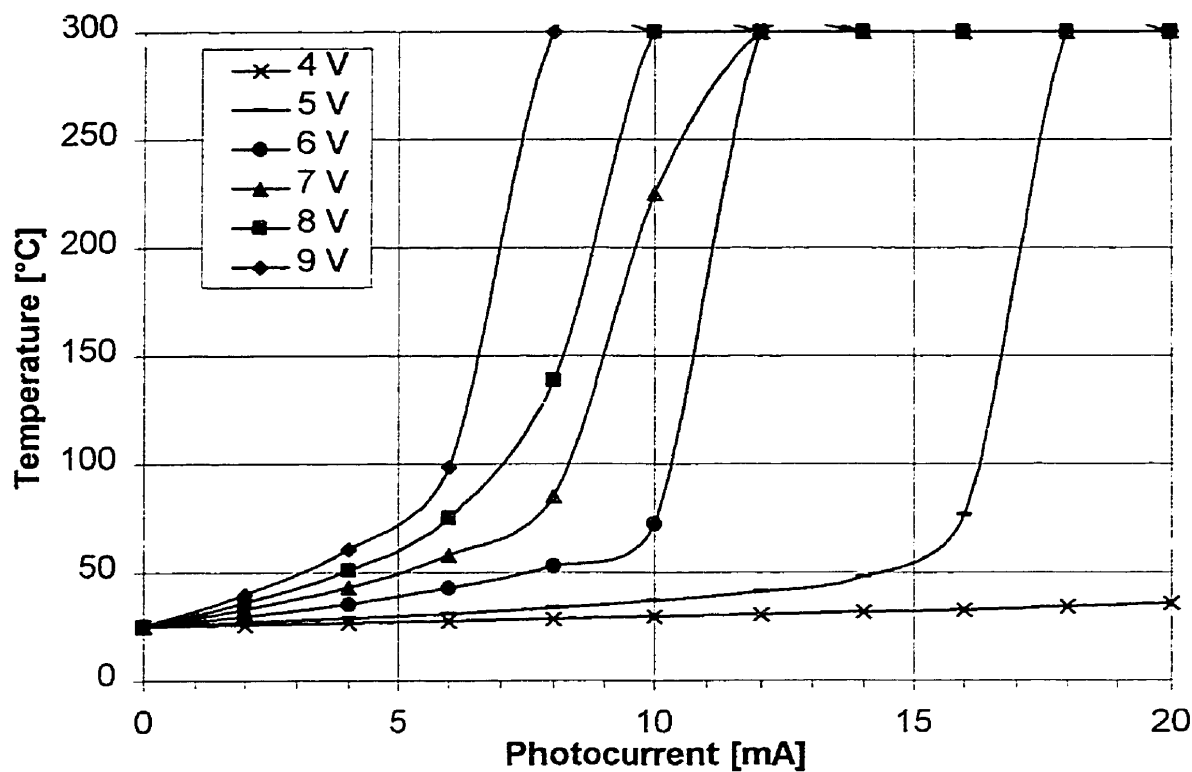
Fig. 5.12 – Peak Temperature in Active Region of Narrow-Electrode Devices

efficient. As temperature rises, the absorption in the waveguide increases, and that, in turn, produces an additional heating, which raises the local temperature further. Eventually, the temperature could increase up to a point where damage is induced in the device. When the voltage or current is increased progressively towards the runaway point, the peak temperature increases rapidly, even though a stable solution to the heat conduction equation still exists. Past the runaway point, however, no stable solution can be found, and the temperature increases from one iteration to another without converging. The isothermic curves are thus closely spaced near the thermal runaway region. Note that the thermal model is ideally suited to study the thermal runaway process, since it does not lead to the costly destruction of real devices. The reduction of the thermal conductivity as temperature increases is also a key ingredient in thermal runaway. In an earlier version of the model, where the conductivity was assumed to remain constant as temperature changed, thermal runaway was never predicted. Thus, thermal runaway re-
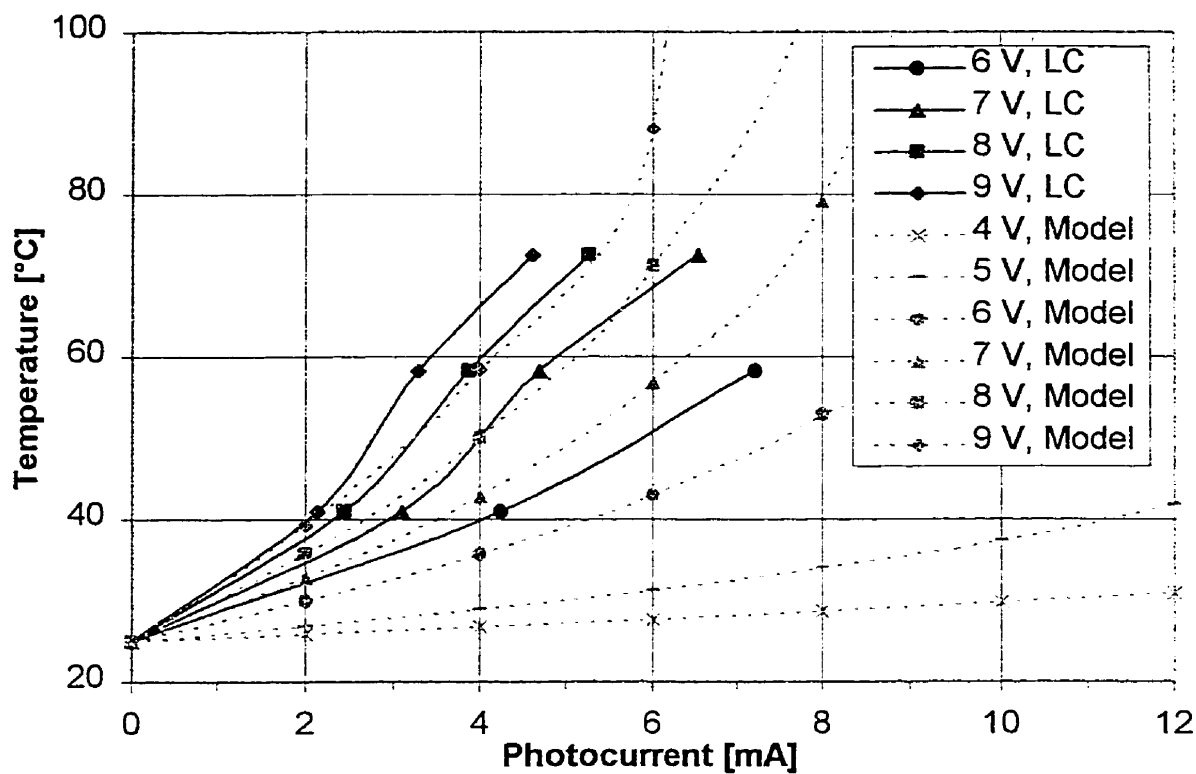
Fig. 5.13 – **Comparison of Experimental and Modelling Results on Narrow-Electrode Devices**
This graph compares the peak surface temperature obtained from the model
and from the liquid-crystal technique.

quires the dependence of both the thermal conductivity and the absorption in the waveguide with respect to temperature.

The model shows that, when approaching thermal runaway, the temperature increases more rapidly with photocurrent at low voltages than at high voltages. The cause of this can be found in the absorption graphs presented in the chapter 4. Between 100 and 200°C, the absorption varies more rapidly with temperature at low voltages. Since temperature is expected to follow the absorption in the waveguide, the internal temperature increases more rapidly with photocurrent when the voltage is low, in conditions close to thermal runaway.

The model also constitutes a good way of investigating the possible influence of the LC on the temperature inside the device. Tables 5.3 and 5.4 show unambiguously that the
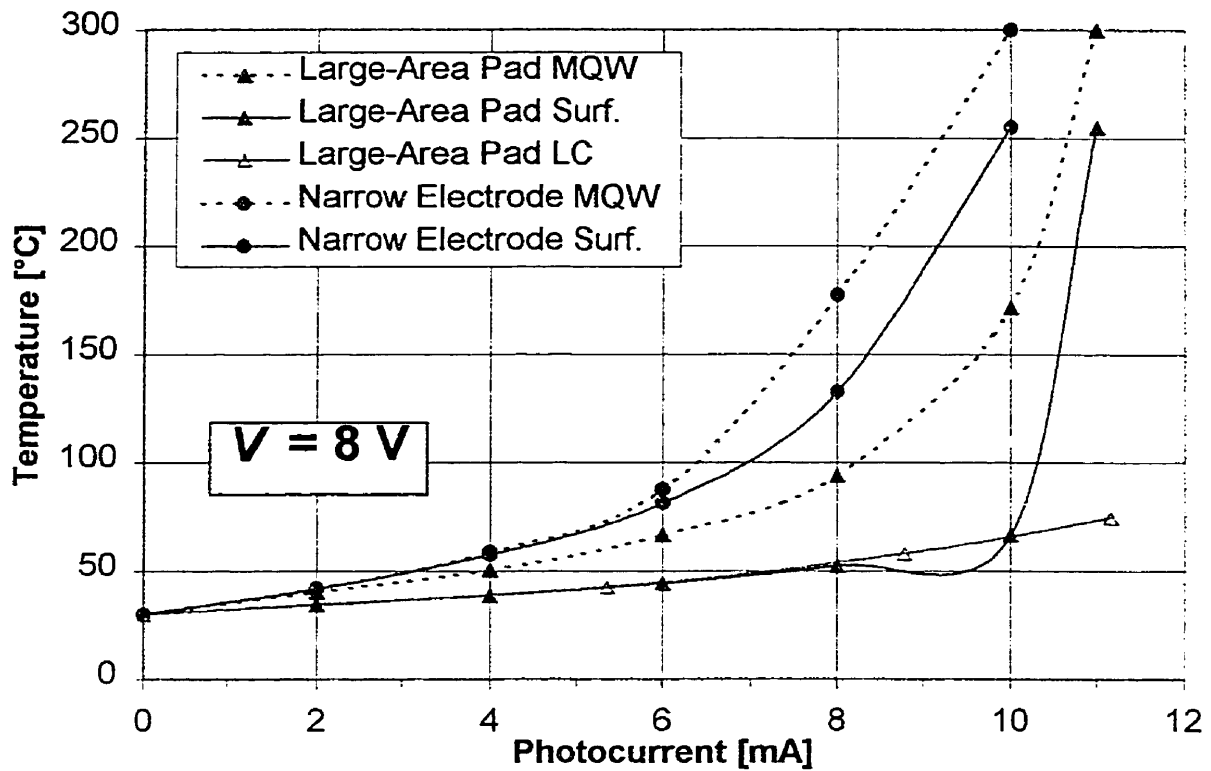
Fig. 5.14 – Comparison Between Large-Pads and Narrow-Electrodes Devices, at 8 V

surface temperature remains the same in the device when LC is added on the surface of the chip, meaning that it does not affect at all the temperature profile in the device. However, depending on the LC thickness, the temperature at the surface of the LC can potentially differ significantly from the device surface temperature. Thus, the thickness of the LC must be kept at a minimum, otherwise the measurements could give erroneous results. An upper limit on the LC thickness was set at 5 μm, at which the error is 8% in the two-dimensional model. In the three-dimensional model, the error is greater, because the heat produced at the hot spot must heat a large volume of LC instead of just a "slice" of LC in the plane model. From the data given in tables 5.3 and 5.4, the largest possible error on the experimental measurements is estimated to be about 15% when the LC thickness is 5 μm. This value is high but is judged acceptable.

Another important result of the modelling is that it confirms the presence of a thermal cross-talk between the waveguide device and the laser, which had already been demonstrated by the LC technique and the blow-up experiments. On figure 5.9, the temperature is always higher when laser heating is present, for identical voltage and current conditions.

In order to gain more confidence in the model, its predictions were compared to the LC measurements. Figure 5.10 shows that the agreement between the model predictions and the measured surface temperature is very good on the discrete large-pad devices. The comparison on hybrid devices, although not shown here, also shows a satisfactory agreement. One important discrepancy is that the model predicts thermal runaway to happen at a photocurrent that is too low, for a given voltage. This is especially true at low voltage: at 6 V, thermal runaway occurs at 14 mA in the model, but liquid-crystal measurements have been carried out at photocurrents up to 19 mA.

There are several possible causes for this discrepancy. The first one is the effect of the discrete nature of the model under high temperature and, hence, high absorption conditions, as was explained in section 5.4. Table 5.5 shows that, under high bias and photocurrent, the modelling results depend on the exact dimension of the elements along the ridge; this means that the finite size of the elements can cause the model to make unreliable predictions in such conditions. When temperature and absorption are not as high, the generated heat is spread over a larger region, and the elements' dimensions do not affect the outcome of the model. However, the difference of a few percent associated with this effect can hardly explain entirely the discrepancy. Another possible cause that can be invoked is a gradual "ramping up" of absorption near the edge of the pad. In the model, no absorption occurs before the electrode edge. In real devices, however, the p-doped InP layer on top of the ridge can conduct the current for some distance past the edge of the gold pad, thus establishing a partial voltage drop across the p-n junction outside of the pad area. Some light should be absorbed before it reaches the pad itself, spreading the heat generation over a longer region of the waveguide than what is pre-

dicted by the model and leading to an overestimation of the temperature under the pad. The effect would be again more important in high temperature and absorption conditions. Unfortunately, it is virtually impossible to modify the model to account for this effect. Finally, the assumption made on the thermal conductivity of quaternary semiconductors and its dependence on temperature can also be invoked as a cause of the discrepancy. If the variation of the conductivity with temperature (given by the exponent n) was slower than assumed, the model would again overestimate the internal temperature.

Although the discussion up to this point concerns the large-pad device, it is also valid for the narrow-electrode device. The temperature map presented in figure 5.11 is not as smooth as for the large pad, because fewer sets of conditions are mapped. The agreement between the model predictions and the experimental data is acceptable, although not as good as on the large-pad devices. Here also, the thermal runaway appears to occur at a higher photocurrent than what is predicted by the model. Finally, the modelling results show that, under similar conditions, the temperature in the active region under the narrow electrode is higher than under a large pad; this proves that the pad is better at dissipating heat. Of course, the gold electrode temperature is very different in the two cases, since the pad provides a way for heat to escape the hot spot, whereas in the narrow electrode, the heat is trapped and can only travel along the ridge. Although the comparison is limited to the 8 V case, the situation is expected to be the same at other voltages.

5.6. Activation Energy Evaluation

Optoelectronic components serving in telecommunications are required to be extremely reliable. The expected lifetime of any component must typically exceed twenty years. Since most optical fiber links are buried or even submerged in the ocean, the cost associated with the replacement of failing components is extremely high, which justifies the high priority placed on reliability. However, testing devices for a period of twenty years

is impractical, and it is necessary to develop accelerated testing schemes to study the degradation mechanisms. The usual procedure is to overstress the device over prolonged periods of time, thus accelerating the aging process. Overstress consists of high temperatures, voltages and optical powers. These tests are based on the assumption that the accelerated degradation mimics the one occurring during normal operation of the device, so that the long-term behavior of the device subjected to normal stress can be deduced from the high-stress testing.

Studying the degradation of the waveguide devices presented in this document is not easy, because most of the times there is no external sign of gradual degradation prior to the occasional failures observed when devices are submitted to high voltage and optical power. Laser diodes, on the contrary, suffer gradual degradation over time, characterized by an increase in the threshold current and a reduction in output efficiency. The only way to study the degradation of waveguide devices is to overstress them and to evaluate the rate of failures. A procedure needs to be established in order to deduce from these tests the estimated lifetime of waveguide devices under normal conditions of operation. To this intent, a number of devices are operated for long periods of time in a variety of high-photocurrent and high-voltage conditions, each leading to a different internal temperature (the stage temperature is fixed at 30°C for these particular overstress tests). One can reasonably assume that degradation is solely a function of internal temperature, and that it is described by an Arrhenius law, with the degradation rate proportional to exp $(-E_a / k_B T)$. The **activation energy**, E_a, is a characteristic of the degradation process, and is given by the slope of the curve on a graph showing the logarithm of lifetime versus the inverse of absolute temperature. If only one degradation is involved over the whole temperature range (in other words, if E_a is not a function of temperature) the lifetime of the device under normal conditions of operation can be estimated by extrapolating this line to the internal temperature expected during normal operation. The activation energy then provides an essential link between the high-stress aging tests and the degradation of the device under normal operating conditions. Note

that this does not hold if the degradation is caused by different mechanisms at the high temperatures found in the overstress tests and at normal operating temperatures.

The role of the model would be to provide the internal temperature for all sets of conditions the devices are submitted to during the aging tests. This information could be further validated by the liquid-crystal technique. If the combination of the aging tests and the modelling were to lead to a determination of the activation energy, this would constitute a very useful application of the thermal model and the experimental technique developed during the course of this work. The aging experiments have been undertaken in the reliability department at Nortel. This work is, however, beyond the scope of this thesis.

Conclusion

The thermal model of the waveguide device has proven to be an efficient tool to study thermal issues. The model computes the internal temperature for any combination of voltage and photocurrent; a convenient way of presenting these results is in the form of temperature maps, in the voltage-photocurrent plane. Despite difficulties in predicting the conditions that lead to thermal runaway, the model predictions were found to agree well with the temperature measured using the liquid-crystal technique; this increases the confidence in the validity of the model predictions. One interesting feature of the model is that it can be easily modified to reflect different configurations of the waveguide device, such as the narrow electrode or the large pad. Eventually, the model could also be used to study the effect of minor changes to the device design, such as a reduction of the length of the pad or electrode or changes in the exact composition or geometry of the ridge, etc. Eventually, the design of future similar devices could be optimized before the device is actually manufactured with the aid of thermal models.

Computer models are becoming an intricate part of the design cycle of optoelectronic devices; thermal models, however, are still uncommon for devices other than laser di-

odes. Because of all the issues already mentioned, the need for thermal models will increase in the near future. This work has demonstrated that, despite the inherent complexity of these models due to temperature-dependent processes and thermal conductivity, accurate and reliable predictions can be made. Apart from what is mentioned in this chapter, the model has also found many other applications within Nortel, proving its usefulness. Thermal modelling of optoelectronic devices is viable and useful: this is perhaps the most important conclusion of this work.

Chapter 6
Correlation of Electro-optic Data and Overstress Tests

It is customary in the optoelectronic industry to assess the reliability of a given lot of devices before using them in commercial products. This can be accomplished by submitting a small number of devices coming from this lot to high stresses, such as high temperature, voltage and photocurrent, and monitoring for any sign of degradation. An example of such overstress test has been given in section 5.6. Because of the duration (typically thousands of hours) and cost associated with these tests, it would be highly desirable to eliminate batches of devices showing poor resistance to high stresses as early as possible in the production process, even before the overstress tests when possible. This would save the cost involved in testing that particular lot.

Because a large number of physical quantities were measured in the course of this work, this is an opportunity to investigate the possibility that any of these quantities could constitute an early indicator of the robustness of the devices under high-stress conditions. With this purpose, all the data acquired on a given wafer, either with the aid of the liquid-crystal technique or from the absorption measurements, was put in relation with the overstress tests results performed on the same wafer. If a sufficient number of wafers is available, it is possible to measure the correlation in any pair of given quantities. For example, a good correlation is expected between the temperature rise measured with the liquid-crystal technique and the absorption coefficient in the waveguide. If the overstress data is found to be well correlated to any other measured quantity, the latter could qualify as an early indicator of the performance of a given wafer to the overstress tests, and potentially of the long-term reliability of the devices coming from this wafer.

Note that, for this study, the correlation will be established uniquely on a wafer basis, and not on any other lot size.

In this chapter, all the quantities measured during the course of this work are compared, and the correlation with the data obtained from the overstress tests is evaluated. The overstress aging tests that this chapter refers to are different from the tests described in section 5.6, as they involve submitting the devices to high reverse bias and high temperatures in large ovens. No optical power is injected into the waveguide for these tests; this simplifies the testing procedure since it does not involve the troublesome operation of coupling light in the waveguide. The overstress data consists of the fraction of the devices that have failed during the established test period. In order to complement the data already available, an additional set of measurements was done; this yielded quantities such as the leakage current and the instantaneous blow-up voltage in the waveguide device. At the end of this chapter, the correlation found between the different quantities enumerated here and the potential existence of early indicators of the long-term reliability are discussed.

6.1. Additional Measurements

Additional measurements were necessary to acquire some missing but important information on the waveguide device that could eventually be linked to the resistance of the device to high levels of stress. Four quantities were measured: the leakage current, the voltage corresponding to a π radian phase shift of the light having propagated through the waveguide, the optical absorption as a function of voltage and the voltage and photo-current causing instantaneous blow-up of the waveguide device. All measurements were made on narrow-electrode devices. Since the measurements of most of these quantities were already described, the manipulation and the test procedure are described only briefly in this chapter.

Fig. 6.1 (A) – **Block Diagram Describing the Additional Measurements**

```
        ┌─────────────────────┐
        │   INSTANTANEOUS      │
        │   BLOW-UP TEST       │
        └─────────────────────┘
                 ↓
   ┌──────────────────────────────┐
   │ • Set laser current at 200 mA │
   │ • Set EDFA current at 150 mA  │
   └──────────────────────────────┘
                 ↓
   ┌──────────────────────────────┐
   │  Set voltage at 8 → 20 V;     │
   │  0.1 V steps                  │
   └──────────────────────────────┘
```

Measure Photocurrent

Adjust EDFA current to have
8 mA of photocurrent in
device

Check for blow-up
(if sudden reduction in
photocurrent)

Write voltage and last photocurrent
to file
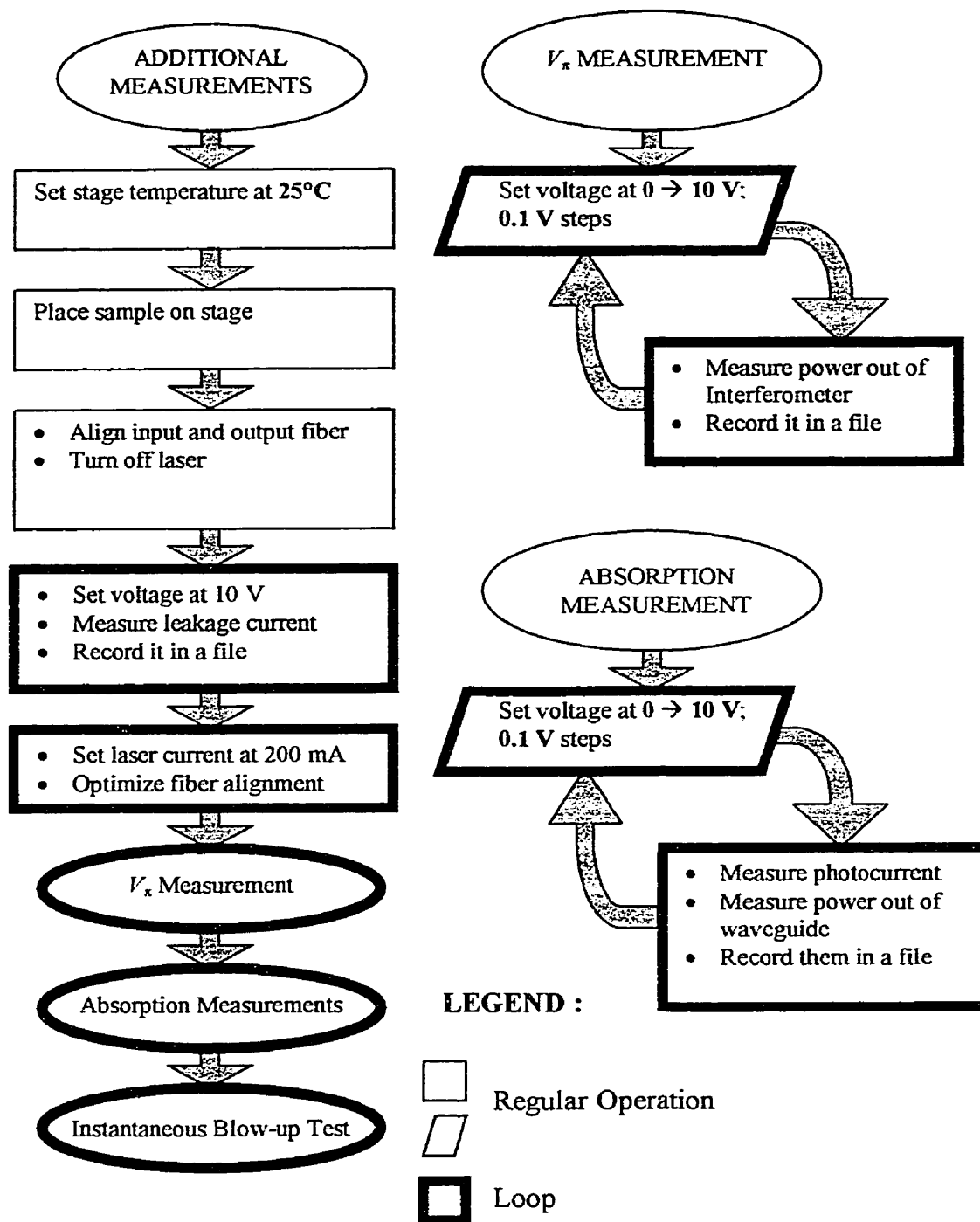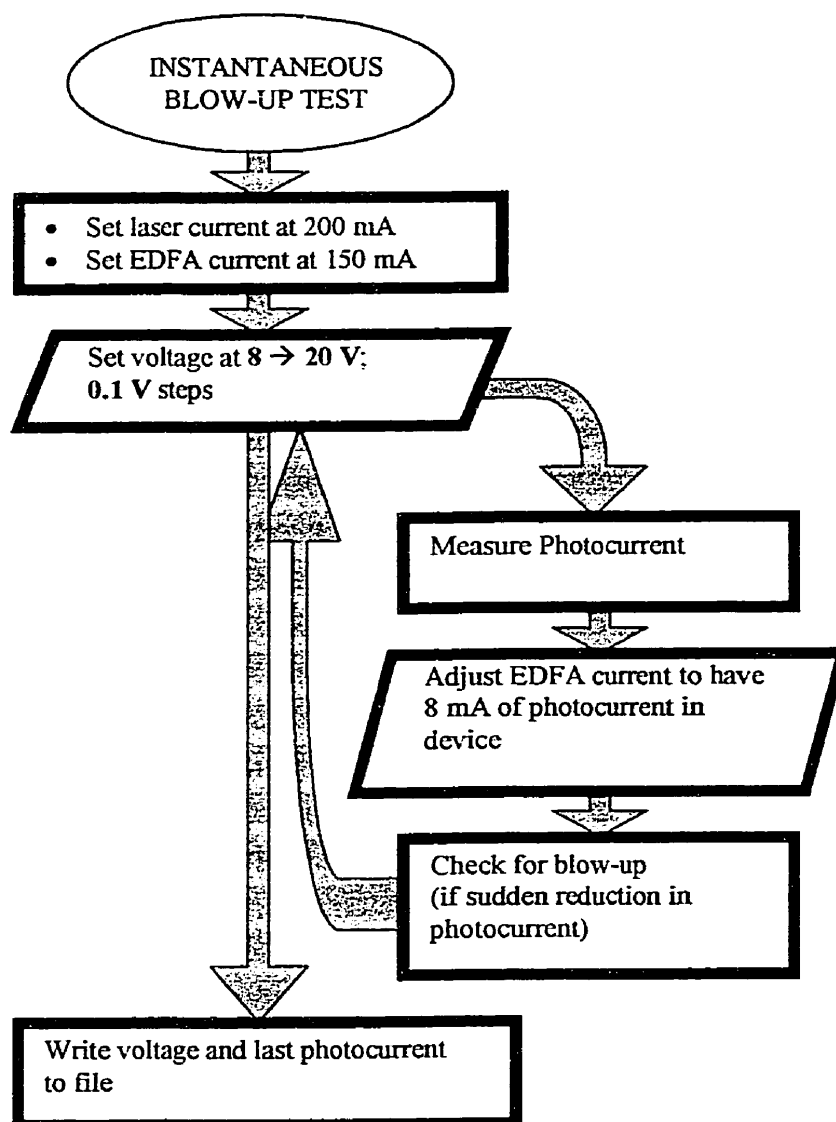
Fig. 6.1 (B) — Block Diagram Describing the Additional Measurements

6.1.1. Measurements

Figure 6.1 shows a block diagram describing how the measurements are carried out. The first step is to measure the leakage current at 10 V; the external laser used to inject light in the waveguide is turned off for this. For the second experiment, the waveguide device is placed in an interferometer, where the light is split in two beams that recombine after one beam has traveled through the waveguide device. The power at the output

of the interferometer is measured as a function of the voltage applied to the waveguide electrode, in order to find the voltage corresponding to a π-radian phase shift. This information indicates the magnitude of the variation of the refractive index in the waveguide as a function of the applied voltage, and is of great importance if the device is to be operated as a phase modulator. The third series of measurements is simply to evaluate again the absorption, to verify that it corresponds well to the measurements presented in chapter 4. Absorption is only measured at one temperature (25°C). Finally, the voltage is increased on the waveguide electrode until instantaneous blow-up occurs, while the laser power is continuously adjusted to maintain the photocurrent at 8 mA. Because it is difficult to inject a large optical power into the waveguide, it is not practical to use a higher photocurrent. These measurements are typically done on eight waveguide devices from each wafer.

The measurements are performed on the test station used for the liquid-crystal experiments, on the samples on which the absorption measurements and the liquid-crystal experiments have already been carried out. The sample is placed on the temperature-controlled stage, under the microscope, the electrical probes are put in contact with the carrier contact pads and two tapered fibers are brought near the facets of the waveguide. The fine alignment and the entire measurements are carried out by the computer via a *HPVee* program.

6.1.2. Data Processing

The processing of the test data is straight-forward. The dark current and the blow-up voltage and photocurrent require no additional treatment. The voltage corresponding to a π-radian phase change, noted V_π, is calculated as the difference between the voltages corresponding to the first two extrema in the power at the output of the interferometer, whether a minimum or a maximum comes first. This is explained graphically by figure 6.2. Only the absorption data needs elaborate treatment, to obtain the absorption in dB
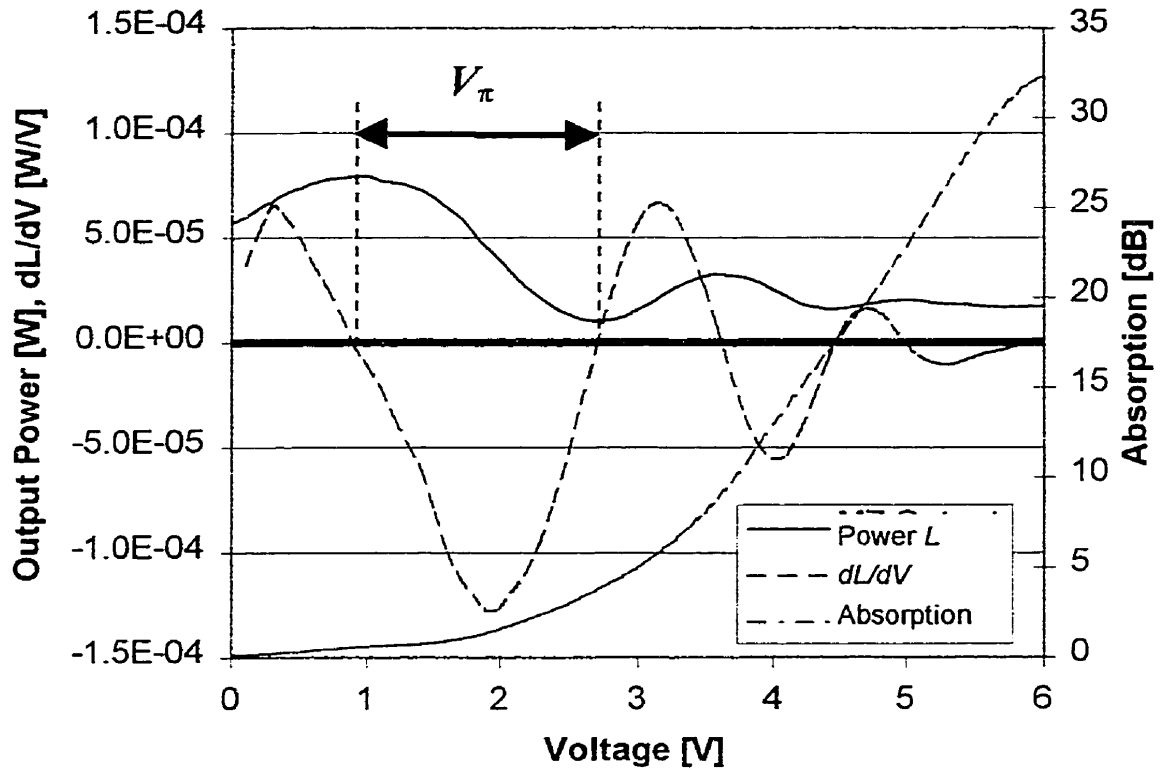
Fig. 6.2 – **Power at Output of the Interferometer as a Function of Voltage** – This graph shows the optical power measured at the output of the interferometer, its derivative with respect to voltage and the absorption measured simultaneously in the waveguide.

from the photocurrent and output power measured as a function of voltage. The procedure used was described in chapter 4.

6.1.3. Results

Typical results of the additional measurements are found in table 6.2. Figure 6.2 shows an example of the power measured at the output of the interferometer as a function of voltage and gives a graphical definition of V_π; also shown is the absorption measured in the waveguide.

6.2. Comparison

6.2.1. Selected Variables

Due to the large amount of data collected during the course of this work, it is impossible to include all of it in the comparison. Instead, specific measured quantities are selected because they were representative of the ensemble of the data. These selected quantities are enumerated in table 6.1, and are referred to as statistical variables in the following discussion.

Three values of the absorption are selected, at voltages of 4, 5 and 6 V, each at a different temperature; these conditions were chosen because they are associated with high absorption but are within the 40 dB limit that has been described in chapter 4. These three quantities are judged to be representative of the ensemble of the absorption data; note that no absorption data is available at high temperatures (over 60°C), since measurements have been performed on large-area devices only on three wafers out of nine. The waveguide absorption was measured again during the additional measurements described in this chapter, this time only at 25°C; these measurements are also included in the comparison.

Similarly, three quantities were used for the liquid-crystal measurements: they are the photocurrents required for the surface temperature to reach the transition temperature of each liquid crystal, at selected voltages. Again, these quantities should be representative of the entire data obtained from liquid-crystal measurements. The other quantities retained are the leakage current, the voltage and electrical power ($I \times V$ product) at blow-up and the voltage corresponding to a π–radian phase shift.

The overstress tests consists of placing a certain number of devices (typically 20) coming from one wafer in a high-temperature (200°C) oven and to apply a large reverse bias (-15 V) to the waveguide electrode, for several thousand hours. The results consist of

Table 6.1 - Selected Variables Retained for the Comparison

Quantity	Definition
Absorption	Absorption measurements (chapter 4)
Abs. 4V 60°C	Absorption in waveguide at $V = 4$ V, $T = 60$°C
Abs. 5V 50°C	Absorption in waveguide at $V = 5$ V, $T = 50$°C
Abs. 6V 25°C	Absorption in waveguide at $V = 6$ V, $T = 25$°C
LC	Liquid-crystal measurements (chapter 2)
I 7V 41°C	Current required for peak surface temperature to be 41°C (clearing point of 1st LC); $T_0 = 25$°C, $V = 7$ V
I 8V 58°C	Current required for peak surface temperature to be 58°C (clearing point of 2nd LC); $T_0 = 25$°C, $V = 8$ V
I 9V 73°C	Current required for peak surface temperature to be 73°C (clearing point of 3rd LC); $T_0 = 25$°C, $V = 9$ V
Add. Meas.	Additional measurements (chapter 6)
Leak. I	Leakage current on waveguide device (junction leakage)
V_π	V_π: Voltage corresponding to a π radian phase shift (difference between 1st and 2nd extrema)
Abs. 4V 25°C	Absorption in waveguide at $V = 4$ V, $T = 25$°C
Abs. 5V 25°C	Absorption in waveguide at $V = 5$ V, $T = 25$°C
Abs. 6V 25°C	Absorption in waveguide at $V = 6$ V, $T = 25$°C
V_{bu} (8 mA)	Voltage leading to instantaneous blow-up, photocurrent kept constant at 8 mA
P_{bu}	Electrical power ($I \times V$) at blow-up, $I \le 8$ mA†
Overstress	Overstress tests (chapter 6)
% Fail 500 hrs	Percentage of devices failing after 500 hrs of stress (200°C, 15V)
% Fail 1000 hrs	Percentage of devices failing after 1000 hrs of stress (200°C, 15V)
% Fail 2000 hrs	Percentage of devices failing after 2000 hrs of stress (200°C, 15V)

† For some devices, the optical power in the waveguide was insufficient to get 8 mA of photocurrent, but the blow-up test was still performed at the maximum possible photocurrent. The blow-up voltage was not registered as V_{bu}, but P_{bu} was still recorded in the subsequent tables.

the fraction of the devices for which significant degradation has been observed after a given number of hours. No sign of damage was observed in the devices still alive at the end of the test.

6.2.2. Comparison of Variables

The results of the measurements made on all devices coming from the same wafer were averaged, to get one single value per wafer for each of the variables defined above; this facilitates the comparison. Table 6.2 shows the averaged value of all the variables on each wafer. Nine wafers are part of this study.

To evaluate the quality of the correlation within any pair of variables, the correlation coefficient was calculated. The correlation coefficient between two variables, X and Y, is given by

$$R_{X,Y} = \frac{\text{Cov}(X,Y)}{\sigma_X \cdot \sigma_Y} \qquad \{6.1\}$$

where σ_X and σ_Y are the standard deviations of variables X and Y and the covariance is defined as

$$\text{Cov}(X,Y) = \frac{1}{N}\sum_{i=1}^{N}(x_i - \bar{x})(y_i - \bar{y}) \qquad \{6.2\}$$

with $\bar{x}$ and $\bar{y}$ the averages of X and Y. N is the size of the statistical sample, i.e. the number of data points. The correlation coefficient is a number between −1 and +1. Close to zero, it means that no correlation exists between the two variables; near 1, there is a strong direct correlation, and near −1, it is an anti-correlation, which means that a decrease in one variable is accompanied by an increase in the other. It is possible to assign to any value of the correlation coefficient a probability that the correlation is meaningful and not the result of two independent random distributions. This threshold depends on the level of confidence desired and the number of data points. For example, with 9 data points, a correlation coefficient over 0.582 ensures that the correlation is meaningful with 90% confidence. Note that there are variables having less than 9 data points, and the threshold for the coefficient is increased accordingly; a table of the re-

Table 6.2 - Comparison of All Variables on a Wafer Basis

Quantity	Unit	R2-1108	R2-1126	R2-1269	R2-1302	R2-1383	R2-1393	R2-1444	R2-1471	R2-1510
Wavelength	nm	1556	1556	1556	1556	1556	1556	1538	1556	1547
Absorption										
$Abs.$ 4 V, 60°C	dB	6.15	2.90	5.26	14.47	14.03	11.73	14.55	18.83	12.74
$Abs.$ 5 V, 50°C	dB	10.30	4.05	8.19	21.32	19.67	20.63	29.51	26.32	17.28
$Abs.$ 6 V, 25°C	dB	8.92	3.81	5.42	21.30	20.34	21.22	31.69	23.38	17.42
LC										
I 7 V, 41.0 °C	mA	5.29	8.66	6.59	3.13	3.88	3.11	3.10	4.02	3.95
I 8 V, 58.2°C	mA	5.09	7.27	5.43	3.75	5.00	4.33	3.87	4.83	4.28
I 9 V, 72.5°C	mA	5.35	6.44	5.27	3.99	5.05	5.00	4.62	5.32	4.88
Add. Meas.										
Leak. I	μA	0.59	0.33	0.04	4.24	21.49	0.13	25.44	1.83	29.90
V_π	V	2.85	4.49	4.26	3.24	2.28	4.45	1.68	2.33	1.90
$Abs.$ 4 V 25°C	dB	0.90	1.09	1.21	3.53	3.38	3.08	13.74	4.79	3.84
$Abs.$ 5 V 25°C	dB	3.10	2.67	2.95	11.09	8.88	8.47	31.99	12.53	11.28
$Abs.$ 6 V 25°C	dB	9.42	7.57	8.12	25.22	22.29	22.27	37.96	27.99	28.29
V_{bu} (8 mA)	V	10.44	10.39	10.12	9.65	11.52	N/A	N/A	10.57	N/A
P_{bu}	mW	80.30	81.05	79.21	74.43	90.69	70.48	63.68	82.35	78.00
Overstress										
% Fail., 500 hrs	%	0	0	N/A	30	5	0	10	25	0
% Fail., 1000 hrs	%	0	0	N/A	70	5	5	10	25	N/A
% Fail., 2000 hrs	%	N/A	3	N/A	88	20	21	N/A	25	N/A

N/A signifies that the data is not available, either because the overstress tests were stopped before 2000 hours, or because, in the case of the blow-up measurements, the maximum optical power that could be injected into the waveguide was not sufficient to obtain a photocurrent of 8 mA.

quired value of the correlation factor as a function of the number of data points has been placed in appendix G.

Table 6.3 gives the correlation coefficients between each pair of variables. For obvious reasons, it is symmetric around the main diagonal. The coefficient has been shaded where the correlation is meaningful with a 90% level of confidence.

Table 6.3 - Correlation of Each Pair of Variables

R	Absorption			Temperature Rise			Additional Measurements							Overstress Test		
	4 V 60°C	5 V 50°C	6 V 25°C	7 V 41°C	8 V 58°C	9 V 73°C	Leak. I	V_π	Abs. 4 V	Abs. 5 V	Abs. 6 V	V_{bu} 8 mA	P_{bu}	% Fail. 500 hrs.	% Fail. 1000 hrs.	% Fail. 2000 hrs.
Abs. 4 V	1.000	0.933	0.889	-0.842	-0.729	-0.635	0.412	-0.660	0.553	0.615	0.871	0.193	-0.120	0.659	0.484	0.439
Abs. 5 V	0.933	1.000	0.986	-0.880	-0.794	-0.673	0.442	-0.643	0.776	0.818	0.941	0.157	-0.410	0.552	0.361	0.446
Abs. 6 V	0.889	0.986	1.000	-0.882	-0.790	-0.678	0.517	-0.641	0.818	0.858	0.958	0.204	-0.461	0.469	0.323	0.479
T 7V 41°C	-0.842	-0.880	-0.882	1.000	0.947	0.823	-0.433	0.564	-0.536	-0.604	-0.820	-0.089	0.366	-0.393	-0.420	-0.567
T 8V 58°C	-0.729	-0.794	-0.790	0.947	1.000	0.912	-0.421	0.539	-0.539	-0.608	-0.767	0.196	0.496	-0.414	-0.521	-0.731
T 9V 73°C	-0.635	-0.673	-0.678	0.823	0.912	1.000	-0.360	0.429	-0.435	-0.508	-0.652	0.297	0.416	-0.532	-0.700	-0.881
Leak. I	0.412	0.442	0.517	-0.433	-0.421	-0.360	1.000	-0.776	0.590	0.612	0.661	0.770	-0.105	-0.183	-0.113	-0.021
V_π	-0.660	-0.643	-0.641	0.564	0.539	0.429	-0.776	1.000	-0.618	-0.653	-0.721	-0.524	0.013	-0.212	-0.088	-0.224
Abs. 4V	0.553	0.776	0.818	-0.536	-0.539	-0.435	0.590	-0.618	1.000	0.994	0.836	0.180	-0.644	0.230	0.053	0.392
Abs. 5V	0.615	0.818	0.858	-0.604	-0.608	-0.508	0.612	-0.653	0.994	1.000	0.883	0.073	-0.647	0.286	0.136	0.578
Abs. 6V	0.871	0.941	0.958	-0.820	-0.767	-0.652	0.661	-0.721	0.836	0.883	1.000	0.135	-0.469	0.425	0.352	0.535
V_{bu} 8 mA	0.193	0.157	0.204	-0.089	0.196	0.297	0.770	-0.524	0.180	0.073	0.135	1.000	0.995	-0.507	-0.678	-0.662
P_{bu}	-0.120	-0.410	-0.461	0.366	0.496	0.416	-0.105	0.013	-0.644	-0.647	-0.469	0.995	1.000	-0.074	-0.159	-0.375
% Fail. 500 hrs.	0.659	0.552	0.469	-0.393	-0.414	-0.532	-0.183	-0.212	0.230	0.286	0.425	-0.507	-0.074	1.000	0.896	0.786
% Fail. 1000 hrs.	0.484	0.361	0.323	-0.420	-0.521	-0.700	-0.113	-0.088	0.053	0.136	0.352	-0.678	-0.159	0.896	1.000	0.971
% Fail. 2000 hrs.	0.439	0.446	0.479	-0.567	-0.731	-0.881	-0.021	-0.224	0.392	0.578	0.535	-0.662	-0.375	0.786	0.971	1.000
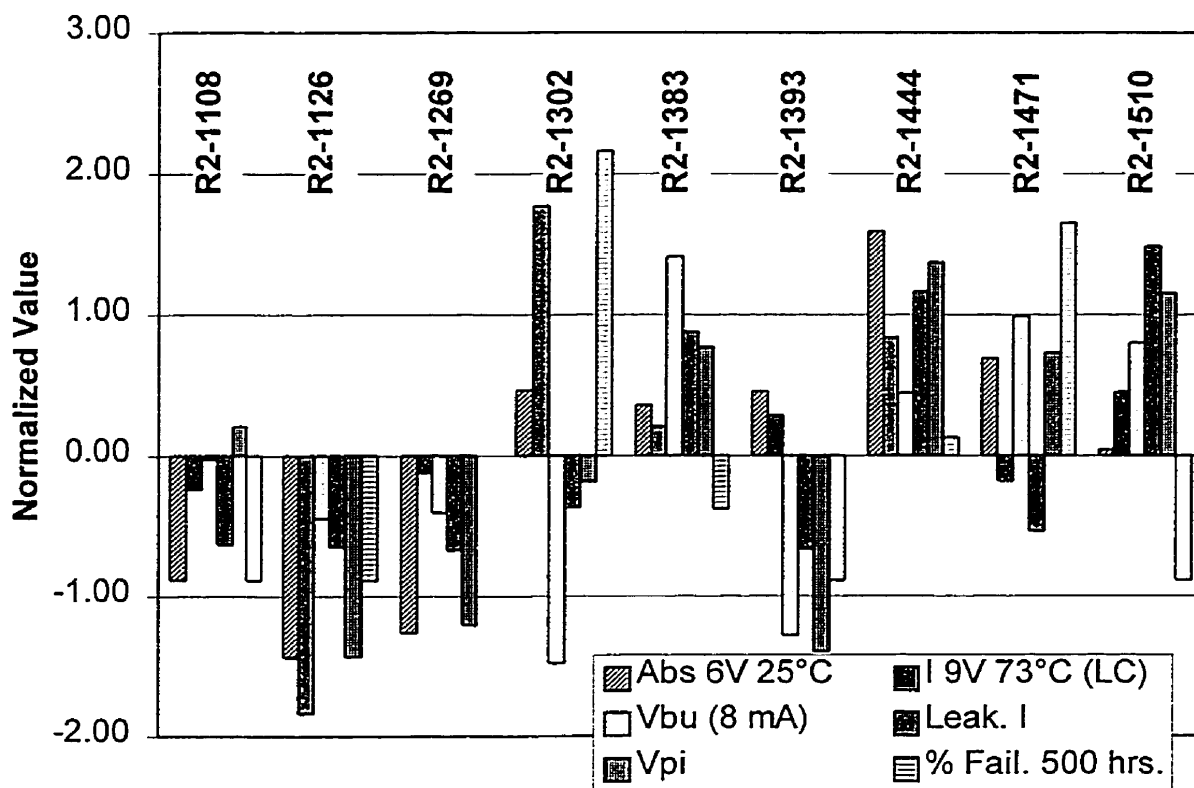
Fig. 6.3 — Correlation of Selected Variables on a Wafer Basis

Selected variables have been plotted together in the graph of figure 6.3. It shows in a graphical form the relationships between all variables. The data in figure 6.3 has been normalized, so that the actual value given on the vertical axis is the difference between the measured value on one wafer and the average on all wafers, divided by the standard deviation associated with this variable across all wafers. The sign of the difference has also been inverted for the liquid-crystal current and V_π, since they exhibit an anticorrelation with the other variables, so that the deviation of a variable from the average, on a given wafer, should be of the same sign for all variables. This graph should be interpreted in the following way: if two variables were perfectly correlated $(R = \pm 1)$, the corresponding bars would always have the same height on any wafer; if they were uncorrelated, no relation would appear between their respective height.

To summarize the data, table 6.4 gives a qualitative appreciation of the correlation between the different variables. In this table, *Very good* means that the correlation is good to the level that one variable could be used to predict the other, *Good* and *Reasonable*, that a correlation is very likely/likely to exist, but not to a point of predictability, and *None*, that there is no clear sign that a correlation exists.

6.3. Discussion

A number of interesting observations can be made from the data in the preceding tables. On a general level, when a correlation is said to be significant with a 90% level of confidence, it only means that the probability that two completely independent random variables give the same level of correlation is 10%. Thus, it establishes that the two variables are linked together. However, unless the coefficient of correlation is close to one, the data points, when plotted on a graph, are not expected all to fall on a straight line. In other words, this means that the knowledge of one of the two variables is not sufficient to predict the other one.

The correlation between all variables describing the optical absorption is excellent, confirming the reproducibility of the measurements. The same situation is observed between the three variables associated with the liquid-crystal experiments, between the blow-up voltage and the blow-up power and also between the three variables describing the overstress tests.

The application of an external electric field across the quantum wells located in the waveguide causes variations in both the refractive index and the absorption coefficient. These two quantities are related by the Kramers-Krönig relationships [31]. For this reason, a good correlation exists between absorption and V_π. Since the temperature rise is also closely related to the absorption in the waveguide, a good correlation should also be found there; this is confirmed by the analysis. One curious result is that these three quantities do not seem to be closely related to the blow-up voltage. If the instantaneous

Table 6.4 - Qualitative Appreciation of the Correlation

Variables	Absorption	Temperature Rise	π Phase-Shift Voltage	Blow-up Voltage	Leakage Current	Overstress Lifetime
Absorption	-	Very good	Very good	None	Good	Reasonable
Temperature Rise	Very good	-	Good	None	Uncertain	Reasonable
π Phase-Shift Voltage	Very good	Good	-	Reasonable	Good	None
Blow-up Voltage	None	None	Reasonable	-	Good	Reasonable
Leakage Current	Reasonable	Uncertain	Good	Good	-	None
Overstress Lifetime	Reasonable	Reasonable	None	Reasonable	None	-

blow-up is a consequence of thermal runaway and is triggered by a large temperature rise, a clear correlation should exist here. This indicates that the instantaneous blow-up is a more complicated process, influenced by a variety of factors.

The analysis also shows that the leakage current is linked in a certain extent to other variables such as V_π, the blow-up voltage and possibly absorption. However, it is known within Nortel that the leakage current is strongly influenced by the history of the device, that is, by previous measurements performed on it; the leakage current can also vary significantly from one device to another. This behavior was observed during the absorption measurements presented in chapter 4. Thus, one has to be very careful when interpreting this quantity, and the correlation observed here is still uncertain.

Finally, maybe the most interesting result of this study is that the performance of the waveguide devices in the overstress tests is correlated reasonably well to the absorption and the temperature rise. This indicates that high absorption could be associated with a reduction of the lifetime of the device under high stresses. There is also a probable correlation between lifetime and the blow-up voltage (although the coefficient is slightly under the 90%-confidence threshold): that is understandable and desirable, since both are believed to be indicators of the long-term reliability of the waveguide device. It is

however not clear why a correlation should exist between the absorption in the waveguide and the lifetime in high-temperature and high-voltage conditions, where no light is coupled in the device. The answer to this is related to the details of the degradation mechanisms occurring in the device, which are not all fully understood yet.

At this point, although a possible correlation has been observed between the overstress lifetime and other variables, this correlation is not sufficient and can not be used to screen out weak wafers, as far as the performance in high-stress conditions is concerned. There is enough variability in the data to indicate that a high absorption does not automatically involve poor performance in high-stress tests. The data does suggests however that one way of improving the performance under overstress and in instantaneous blow-up tests could be to modify the device design to reduce the absorption in the waveguide, or, equivalently, to reduce the temperature rise for a given current-voltage combination, in order to produce more robust and reliable devices. Unfortunately, one possible consequence is that a higher operating voltage would be required to achieve the same level of performance of the device (to achieve the same optical absorption in an electro-absorption device, for example); the increase in internal temperature during normal operation could then negate the improvement in reliability. Nonetheless, there is probably still room for optimization.

Conclusion

This study has revealed that a clear correlation exists between the various electro-optic quantities, that is, the absorption coefficient and the voltage corresponding to a phase shift of π radian, and the temperature increase in the waveguide device. This correlation was expected, and this adds confidence to the present understanding of how light is absorbed as it travels along the waveguide and how temperature increases locally as a result of this.

Device lifetime in high-stress conditions was also found to be correlated to the other variables in the study. The present data does not point to any screening process but indicates how to modify the design parameters to increase the resistance to high stresses and potentially the long-term reliability of the waveguide device. The number of wafers part of this study is too small to draw definite conclusions, and should be increased in the future to acquire a clearer view of the links that exist between the various quantities considered during this investigation.

General Conclusion

A separate conclusion has been included at the end of each chapter, which reviewed the principal findings of each set of experiments. The general conclusion presented here contains comments on this work from a more general point of view.

Over the course of this work, thermal issues in the waveguide device have been studied extensively, and are much better understood now. A number of interesting phenomena have been clarified and described in detail, for example, thermal runaway and the thermal cross-talk between the laser and the waveguide device in the hybrid configuration. In that sense, this work has fulfilled its primary objective, that is, to improve the understanding of thermal issues in the waveguide device.

The liquid-crystal technique was demonstrated to constitute a valuable means of studying the temperature rise in the waveguide device. It has provided very valuable information, and is still used within Nortel for various investigations at this moment. This technique met all the criteria enumerated at the beginning of this document. The only problem encountered had to do with obtaining a thin and uniform layer of liquid crystal on the surface of the chip; the problem can be circumvented by careful manipulation, so that the accuracy of the results does not suffer. Thermal modelling of the waveguide device was carried out in order to complement the information obtained from the liquid-crystal technique. Although the development of the model has been a slow process, its predictions were successfully validated by comparison to the experimental data. The model predictions were found to be accurate and reliable in most cases (one exception being for conditions near the thermal runaway point).

The model and the liquid-crystal technique are two characterization tools, now considered to be mature, and can serve in more complex investigations. One example has been presented in chapter 6, where various electro-optic quantities and the measured temperature rise in the waveguide device were compared to the results of instantaneous blow-up tests and long-term overstress tests. The results indicate that a link could exist between the performance under high electrical and thermal stresses and the absorption and the temperature rise measured in the waveguide. This analysis suggests design modifications that could help to improve the robustness of the waveguide device in high-stress conditions and potentially also its long-term reliability.

As optical power continues to increase in optical fiber systems, thermal management in optoelectronic devices is becoming increasingly important. The trend towards increased integration of multiple devices on a common substrate will only make the situation more critical. It is hoped that this work has helped to demonstrate the importance of thermal issues in optoelectronic devices, and that the research community and the industry will consider the tools developed here as a useful means of further studying these issues.

References

1. P.S. ZORY ET AL., *Quantum Well Lasers*, Academic Press (1993).

2. Nortel's Product Datasheet on EDFA Module

3. M. NISHIGUCHI, M. FUJIHARA, A. MIKI, H. NISHIZAWA, "Precision Comparison of Surface Temperature for GaAs IC's", *IEEE Transactions on Components, Hybrids, and Manufacturing Technology*, vol. 16, no. 5, pp. 543-549 (1993).

4. M. ASHAUER, J. ENDE, H. GLOSH, H. HAFFNER, K. HILTMANN, "Thermal Characterization of Microsystems by Means of High-Resolution Thermography", *Microelectronics Journal*, vol. 28, no. 3, p. 327-335 (1997).

5. C. HALL, L. GOLDBERG, D. MEHUYS, "Technique for Lateral Temperature Profiling in Optoelectronic Devices Using a Photoluminescence Microprobe", *Applied Physics Letters*, vol. 61, no. 4, pp. 384-386 (1992).

6. P. W. EPPERLEIN, G. L. BONA, P. ROENTGENS, "Local Mirror Temperatures of Red-Emitting (Al)GaInP Quantum-Well Laser Diodes by Raman Scattering and Reflectance Modulation Measurements", *Applied Physics Letters*, vol. 60, no. 6, pp. 680-682 (1992).

7. P. W. EPPERLEIN, P. BUCKMANN, A. JAKUBOWICZ, "Lattice Disorder, Facet Heating and Catastrophic Optical Mirror Damage of AlGaAs Quantum-Well Lasers", *Applied Physics Letters*, vol. 62, no. 5, pp. 455-457 (1993).

8. D. BURGESS, P. TAN, "Improved Sensitivity for Hot Spot Detection Using Liquid Crystals", *IEEE International Reliability Physics Symposium 1984 Proc.*, pp. 119-121.

9. ZS. KOHÁRI, A. CSENDES, V. SZÉKELY, M. RENCZ, "Thermal Investigations of Monolithic Structures", *Microelectronics Journal*, vol. 28, no. 3, pp. 317-325 (1997).

10. A. GOEL, A. GRAY, "Liquid Crystals Technique as a Failure Analysis Tool", *IEEE International Reliability Physics Symposium 1981 Proc.*, p. 115.

11. J. HIATT, "A Method of Detecting Hot Spot Using Liquid Crystals", *IEEE International Reliability Physics Symposium 1981 Proc.*, pp. 130-133.

12. J. WEST, "A Simple Technique for Analysis of ESD Failures of Dynamic RAMS Using Liquid Crystals", *IEEE International Reliability Physics Symposium 1982 Proc.*, pp. 185-187.

13. E. M. FLEUREN, "A Very Sensitive, Simple Analysis Technique Using Liquid Crystals", *IEEE International Reliability Physics Symposium 1983 Proc.*, pp. 148-149.

14. W. NAKWASKI, "Thermal Model of the Catastrophic Degradation of High-Power Stripe-Geometry GaAs/AlGaAs Double-Heterostructure Diode Lasers", *Journal of Applied Physics*, vol. 67, no. 4, pp. 1659-1668 (1990).

15. R. SCHATZ, C.G. BETHEA, "Steady-State Model for Facet Heating Leading to Thermal Runaway in Semiconductor Lasers", *Journal of Applied Physics*, vol. 76, no. 4, pp. 2509-2521 (1994).

16. C. KITTEL, *Introduction to Solid-state Physics*, 6th Edition, John Wiley & Sons (1986).

17. W. ASHCROFT, N. D. MERMIN, *Solid State Physics*, Saunders College Publishing (1976)

18. A. AMITH, I. KUDMAN, E.F. STEIGMEIER, "Electron and Phonon Scattering in GaAs at High Temperatures", *Physical Review*, vol. 138, no. 4A, pp. A1270-A1276 (1965).

19. S. ADACHI, "Chapter 4: Thermal Properties", *Physical Properties of III-V Semiconductor Compounds: InP, InAs, GaAs, GaP, InGaAs, InGaAsP*, edited by John Wiley and Sons, Wiley Interscience Publications, pp. 55-62 (1992).

20. S. ADACHI, "Lattice Thermal Resistivity of III-V Compounds", *Journal of Applied Physics*, vol. 54, no. 4, pp. 1844-1848 (1983).

21. S. ADACHI, "Thermal conductivity of InGaAs", *Properties of Lattice-Matched and Strained Indium Gallium Arsenide*, edited by Pallab Bhattacharya, INSPEC (IEE), pp. 35-40 (1993).

22. W. NAKWASKI, "Thermal Conductivity of Binary, Ternary and Quaternary III-V Compounds", *Journal of Applied Physics*, vol. 64, no. 1, pp. 159-166 (1988).

23. E.F. HOCKINGS, I. KUDMAN, T.E. SEIDEL, C.M. SCHMELTZ, E.F. STEIGMEIER, "Thermal and Electrical Transport in InAs-GaAs Alloys", *Journal of Applied Physics*, vol. 37, no. 7, pp. 2879-2887 (1966).

24. B. ABELES, *Physical Review*, vol. 131 (1963), p. 1909.

25. J.C. BRICE, "Thermal Conductivity of Indium Phosphide", *Properties of Indium Phosphide*, EMIS Data Series No. 6, INSPEC (IEE), pp. 20-21 (1991).

26. E.F. STEIGMEIER, I. KUDMAN, "Acoustical-Optical Phonon Scattering in Ge, Si, and III-V Compounds", *Physical Review*, vol. 141, no. 2, pp. 767-774 (1966).

27. H.S. CARSLAW, J.C. JAEGER, *Conduction of Heat in Solids*, 2nd edition, Oxford, pp. 10-11 (1959).

28. Y. S. TOULOUKIAN, R. W. POWELL, C. Y. HO, P. G. CLEMENS, *Thermophysical Properties of Matter: Thermal Conductivity, Nonmetallic Solids*, The TPRC Data Series, Vol. 2, IFI/Plenum (1970).

29. N.B. VARGAFTIK, *Tables on the Thermophysical Properties of Liquid and Gases*, 2nd Edition, Hemisphere Publishing Corp., Washington (1975).

30. Internal Publication, Nortel

31. R.W.P. KING, S. PRASARD, *Fundamental Electromagnetism Theory and Applications*, Prentice-Hall, p. 124 (1986).

Appendix A - Information on Liquid Crystals

Manufactured by Merck (Germany), now owning BDH (England)

Reported Data

Liquid Crystal Designation	Melting Point [°C]	Clearing Point [°C]
K18	15	29
K21	30	43
E7	<-30	58
N4	?	84

Notes:
1) K18 was not used in experiments, because its clearing point is too low.
2) K21 was most of the times liquid, but sometimes solid at room temperature; in that case, the warmth of a human hand holding the syringe was enough to melt it.
3) The clearing point of N4 was found to change over long periods of time (weeks), when left in the syringe, down to about 70 C; the clearing point was measured every time this LC was used.

Appendix B - List of Equipment

Equipment	Manufacturer	Model	Comment
Computer	Sona	Pentium 133 MHz	
-> GPIB Card	National Instruments	AT-GPIB/TNT	
HPVee software	Hewlett-Packard	HPVee Version 4.0	

Electrical Equipment

Laser diode controller	ILX Lightwave	LDC-3722B	GPIB-controlled
Digital multimeter	Keithley	196	GPIB-controlled
Dual power supply	Xantrex	XTD20-3	GPIB-controlled
Lightwave multimeter	Hewlett-Packard	HP8153A	GPIB-controlled
-> Sensor module	Hewlett-Packard	HP81531A	
Micropositioner controller	Newport	ESA-C	GPIB-controlled
Piezoelectric crystal voltage source	Physik Intrumente	P-263	
TEC controller	ILX Lightwave	LDT-5412	
Precision current source	ILX Lightwave	LDX-3412	
Microscope lamp power supply	Mitutoyo		
GPIB cables			
Electrical wires			
Tunable laser	Hewlett-Packard	HP8168F	1435 - 1595 nm

Optical Equipment

High-magnification microscope	Microview Canada		
-> Objectives, long working distance (4)	Mitutoyo		10X (NA), 20X (NA), 40X (NA), 60X (NA)
-> Lamp	Mitutoyo		
Low-magnification microscope	Titan		for LC application; x15 - x60
Packaged laser diode	Nortel		$\lambda = 1556$ nm
Erbium-doped-fiber amplifier	Nortel		
Tapered fibers (2)	Namiki		
Connectorized fibers			

Mechanical Equipment

Optical anti-vibration pneumatic table	Melles Griot	070TC011/I	
Piezoelectric crystals (3)	Physik Intrumente	P.282.10	
Electro-striction actuators (3)	Newport	ESA-1330-OPT-01	
Fiber micro-positioner stages (2)	LineTool Co.	J-LH, J-RH	3-axis
Probe micro-positioner stage	Quater	XYZ 500TIS	3-axis; for LC deposition
Large micro-positioner stage	Opto Micron Ind.	Marv Fx118	2-axis; under microscope
Magnetic bases (3)	Newport	MB-3	

Appendix C.1 - LC Data, Hybrid Large-Pad Devices

V [V]		Device	...	
T [°C]		I [mA]	...	
...		...	...	

9 V		R2-1444 P1	R2-1444 P2	R2-1444 P3
	30.0	0.00	0.00	0.00
	41.5	3.48	3.53	3.19
	57.3	6.50	7.12	6.06
	74.0	8.15	8.27	7.60

8 V		R2-1444 P1	R2-1444 P2	R2-1444 P3
	30.0	0.00	0.00	0.00
	41.5	4.12	4.27	3.65
	57.3	7.79	8.20	7.05
	74.0	9.45	10.34	9.18

7 V		R2-1444 P1	R2-1444 P2	R2-1444 P3
	30.0	0.00	0.00	0.00
	41.5	5.27	5.65	4.66
	57.3	10.27	11.02	9.25
	74.0	12.63	14.34	12.14

6 V		R2-1444 P1	R2-1444 P2	R2-1444 P3
	30.0	0.00	0.00	0.00
	41.5	7.99	8.77	6.41
	57.3	15.63		
	74.0			

Note:
Empty cells are due measurements that are either incorrect
or impossible because of the limitations of the optical power available

Appendix C.2 - LC Data, Discrete Large-Pad Devices

V [V]	Device	...
T [°C]	I [mA]	...
...	...	...

9 V		R2-1444 PB2	R2-1444 PB3	R2-1444 P7	R2-1444 P6	R2-1444 P5
	30.0	0.00	0.00	0.00	0.00	0.00
	42.5	4.54	4.85	4.21		4.60
	58.0	7.49	7.12	6.66	7.41	
	74.3		9.91	8.73	8.86	

8 V						
	30.0	0.00	0.00	0.00	0.00	0.00
	42.5	5.35	5.72	5.04		5.34
	58.0	9.13	8.93	8.27	9.41	
	74.3		11.98	10.39	11.12	

7 V						
	30.0	0.00	0.00	0.00	0.00	0.00
	42.5	7.11	7.73	6.73		6.84
	58.0	12.46	11.99	11.47	14.18	
	74.3		14.87	14.08	14.31	

6 V						
	30.0	0.00	0.00	0.00	0.00	0.00
	42.5	11.00	13.04	10.97		11.51
	58.0			18.19		
	74.3			18.72		

Note:
Empty cells are due measurements that are either incorrect
or impossible because of the limitations of the optical power available

Appendix C.3 - LC Data, Discrete Narrow-Electrode Devices

V [V]	Device	...
T [°C]	I [mA]	...
...	...	...

9 V	R2-1108 I	R2-1108 II	R2-1126 I	R2-1126 II	R2-1269 I	R2-1269 II	R2-1302 I	R2-1302 II
25.0	0.00	0.00	0.00	0.00	0.00	0.00	0.00	0.00
41.0	2.54	2.85	3.19	3.51	2.77	2.76	2.11	2.08
58.2	3.72	3.79	4.30	5.16	3.70	3.96	3.22	3.16
72.5	5.64	5.07	5.86	7.01	5.15	5.39	4.04	3.94

8 V	R2-1108 I	R2-1108 II	R2-1126 I	R2-1126 II	R2-1269 I	R2-1269 II	R2-1302 I	R2-1302 II
25.0	0.00	0.00	0.00	0.00	0.00	0.00	0.00	0.00
41.0	3.24	3.23	4.53	5.60	3.50	3.61	2.34	2.41
58.2	5.10	5.08	6.74	7.79	5.24	5.63	3.83	3.66
72.5	7.55	6.56	8.66	10.84	7.18	7.88	4.83	4.70

7 V	R2-1108 I	R2-1108 II	R2-1126 I	R2-1126 II	R2-1269 I	R2-1269 II	R2-1302 I	R2-1302 II
25.0	0.00	0.00	0.00	0.00	0.00	0.00	0.00	0.00
41.0	5.34	5.24	8.19	9.13	6.38	6.79	3.09	3.17
58.2	8.28	8.46	11.67		9.04	9.70	4.64	4.75
72.5	10.93	10.71			12.19		6.27	6.25

6 V	R2-1108 I	R2-1108 II	R2-1126 I	R2-1126 II	R2-1269 I	R2-1269 II	R2-1302 I	R2-1302 II
25.0	0.00	0.00	0.00	0.00	0.00	0.00	0.00	0.00
41.0	10.80				11.49		4.99	5.50
58.2							8.01	7.93
72.5							10.23	10.33

9 V	R2-1383 I	R2-1383 II	R2-1383 III		R2-1393 I	R2-1393 II	R2-1393 III	R2-1393 IV
25.0	0.00	0.00	0.00		0.00	0.00	0.00	0.00
41.0	2.38	2.23	2.31		1.66	1.70		1.79
58.2		3.85	4.07		3.30	3.27	3.51	
72.5	4.90	5.14	5.12		4.95	4.68	5.58	4.78

8 V	R2-1383 I	R2-1383 II	R2-1383 III		R2-1393 I	R2-1393 II	R2-1393 III	R2-1393 IV
25.0	0.00	0.00	0.00		0.00	0.00	0.00	0.00
41.0	2.81	2.74	2.85		2.20	2.19		2.27
58.2		4.87	5.12		4.26	4.11	4.63	
72.5	6.19	6.68	6.76		6.35	5.79	7.16	

7 V	R2-1383 I	R2-1383 II	R2-1383 III		R2-1393 I	R2-1393 II	R2-1393 III	R2-1393 IV
25.0	0.00	0.00	0.00		0.00	0.00	0.00	0.00
41.0	3.91	3.73	3.99		3.11	3.13		3.10
58.2		7.73	8.05		6.27	6.06	6.64	
72.5	9.16	10.01	10.30					

6 V	R2-1383 I	R2-1383 II	R2-1383 III		R2-1393 I	R2-1393 II	R2-1393 III	R2-1393 IV
25.0	0.00	0.00	0.00		0.00	0.00	0.00	0.00
41.0	8.59	8.41	8.66			5.57		5.39
58.2								
72.5								

9 V	R2-1444 I	R2-1444 II	R2-1444 III	R2-1444 IV	R2-1471 I	R2-1471 II	R2-1471 III	R2-1471 IV
25.0	0.00	0.00	0.00	0.00	0.00	0.00	0.00	0.00
41.0	2.04	2.20	2.21	2.07	2.31	2.25	2.41	2.10
58.2	3.23	3.27	3.37	3.26	3.83	3.81	4.04	3.45
72.5	4.40		5.01	4.47	5.32	5.60	5.02	

8 V	R2-1444 I	R2-1444 II	R2-1444 III	R2-1444 IV	R2-1471 I	R2-1471 II	R2-1471 III	R2-1471 IV
25.0	0.00	0.00	0.00	0.00	0.00	0.00	0.00	0.00
41.0	2.39	2.72	2.35	2.31	2.95	3.00	2.94	2.75
58.2	3.87	3.96	3.86	3.79	4.86	4.98	5.00	4.49
72.5	5.06		5.72	5.00	7.18	7.37	6.29	

7 V	R2-1444 I	R2-1444 II	R2-1444 III	R2-1444 IV	R2-1471 I	R2-1471 II	R2-1471 III	R2-1471 IV
25.0	0.00	0.00	0.00	0.00	0.00	0.00	0.00	0.00
41.0	3.05	3.35	3.03	2.98	4.13	4.28	3.92	3.74
58.2	4.69	4.58	5.10	4.44	7.84	7.76	7.15	6.68
72.5	6.44		6.77	6.46		10.61	9.24	

6 V	R2-1444 I	R2-1444 II	R2-1444 III	R2-1444 IV	R2-1471 I	R2-1471 II	R2-1471 III	R2-1471 IV
25.0	0.00	0.00	0.00	0.00	0.00	0.00	0.00	0.00
41.0	4.37	4.37	4.20	4.08	8.24	8.35		
58.2	7.44	7.16	7.11	7.14				
72.5								

9 V	R2-1510 I	R2-1510 II	R2-1510 III	R2-1510 IV	R2-1510 V	R2-1510 VI
25.0	0.00	0.00	0.00	0.00	0.00	0.00
41.0	2.73	3.01	2.34	2.25	2.18	2.20
58.2	4.02	4.11			3.51	3.43
72.5	5.65	6.31	5.14		4.94	4.57

8 V	R2-1510 I	R2-1510 II	R2-1510 III	R2-1510 IV	R2-1510 V	R2-1510 VI
25.0	0.00	0.00	0 00	0.00	0.00	0.00
41.0	3.27	3.58	2.94	3.07	2.79	2.81
58.2	5.51	5.23			4.30	4.26
72.5	7.57	7.76	6.27		6.14	6.06

7 V	R2-1510 I	R2-1510 II	R2-1510 III	R2-1510 IV	R2-1510 V	R2-1510 VI
25.0	0.00	0.00	0.00	0.00	0.00	0.00
41.0	5.45	5.23	4.16	3.97	3.82	3.85
58.2		8.43			7.43	6.25
72.5			9.18		8.59	

6 V	R2-1510 I	R2-1510 II	R2-1510 III	R2-1510 IV	R2-1510 V	R2-1510 VI
25.0	0.00	0.00	0.00	0.00	0.00	0.00
41.0				8.79	8.06	
58.2						
72.5						

Appendice C.4 - Averaged Temperature Rise on each Wafer

V [V]	Device	...
T [°C]	I [mA]	...
...	...	...

Narrow-electrode Devices

9 V	R2-1108	R2-1126	R2-1269	R2-1302	R2-1383	R2-1393	R2-1444	R2-1471	R2-1510
25.0	0.00	0.00	0.00	0.00	0.00	0.00	0.00	0.00	0.00
41.0	2.70	3.35	2.76	2.10	2.31	1.72	2.13	2.26	2.24
58.2	3.75	4.73	3.83	3.19	3.96	3.36	3.28	3.78	3.47
72.5	5.35	6.44	5.27	3.99	5.05	5.00	4.62	5.32	4.88

8 V	R2-1108	R2-1126	R2-1269	R2-1302	R2-1383	R2-1393	R2-1444	R2-1471	R2-1510
25.0	0.00	0.00	0.00	0.00	0.00	0.00	0.00	0.00	0.00
41.0	3.23	5.07	3.56	2.37	2.80	2.22	2.44	2.91	2.90
58.2	5.09	7.27	5.43	3.75	5.00	4.33	3.87	4.83	4.28
72.5	7.05	9.75	7.53	4.76	6.54	6.43	5.26	6.95	6.15

7 V	R2-1108	R2-1126	R2-1269	R2-1302	R2-1383	R2-1393	R2-1444	R2-1471	R2-1510
25.0	0.00	0.00	0.00	0.00	0.00	0.00	0.00	0.00	0.00
41.0	5.29	8.66	6.59	3.13	3.88	3.11	3.10	4.02	3.95
58.2	8.37	11.67	9.37	4.69	7.89	6.32	4.70	7.36	6.84
72.5	10.82		12.19	6.26	9.82		6.56	9.92	8.89

6 V	R2-1108	R2-1126	R2-1269	R2-1302	R2-1383	R2-1393	R2-1444	R2-1471	R2-1510
25.0	0.00	0.00	0.00	0.00	0.00	0.00	0.00	0.00	0.00
41.0	10.80		11.49	5.25	8.55	5.48	4.26	8 30	8.42
58.2				7.97			7.21		
72.5				10.28					

Large-Pad Devices, Wafer R2-1444

9 V	Hybrid	Discrete
30.0	0.00	0.00
42.0	3.40	4.55
58.0	6.56	7.09
74.0	8.01	9.17

8 V	Hybrid	Discrete
30.0	0.00	0.00
42.0	4.01	5.36
58.0	7.68	8.78
74.0	9.66	11.16

7 V	Hybrid	Discrete
30.0	0.00	0.00
42.0	5.19	7.10
58.0	10.18	11.98
74.0	13.04	14.42

6 V	Hybrid	Discrete
30.0	0.00	0.00
42.0	7.72	11.63
58.0	15.63	18.19
74.0		

Appendix D - Polynomial Coefficients Giving Absorption

Notes:

1) for a given voltage,

$$\alpha(T) = A_5\,T^5 + A_4\,T^4 + A_3\,T^3 + A_2\,T^2 + A_1\,T + A_0$$

2) a blank value means that a lower-order polynomial is used; that coefficient is then 0.

A_5	A_4	A_3	A_2	A_1	A_0	Max. T
			1.28E-01	-5.08E+00	1.15E+02	70
			1.37E-01	-5.04E+00	1.17E+02	70
			1.75E-01	-6.52E+00	1.63E+02	70
			2.66E-01	-1.06E+01	2.42E+02	70
			3.13E-01	-9.63E+00	2.63E+02	70
	1.28E-03	-1.93E-01	1.05E+01	-2.26E+02	1.91E+03	70
		2.46E-02	-1.82E+00	5.95E+01	-1.66E+02	70
		1.07E-02	5.02E-01	-2.23E+01	8.71E+02	70
-1.19E-05	4.00E-03	-4.37E-01	2.21E+01	-4.35E+02	3.71E+03	150
-4.51E-06	1.28E-03	-9.67E-02	4.74E+00	-7.91E+00	5.44E+02	150
	-3.40E-05	6.46E-03	4.00E+00	-7.69E+01	3.41E+03	250
	-4.45E-05	1.25E-02	2.36E+00	7.34E+01	3.71E+03	250
	-2.78E-05	5.26E-03	3.16E+00	3.22E+01	8.69E+03	250
	8.65E-07	-7.79E-03	4.99E+00	-8.49E+01	1.48E+04	250
			2.17E+00	1.90E+02	1.04E+04	250
			2.03E+00	2.03E+02	1.24E+04	250
			1.87E+00	2.18E+02	1.42E+04	250
			1.84E+00	2.00E+02	1.75E+04	250
			1.91E+00	1.64E+02	2.15E+04	250
			2.00E+00	1.25E+02	2.51E+04	250
			2.02E+00	1.09E+02	2.72E+04	250

Predicted Absorption, R2-1444, 1544 nm
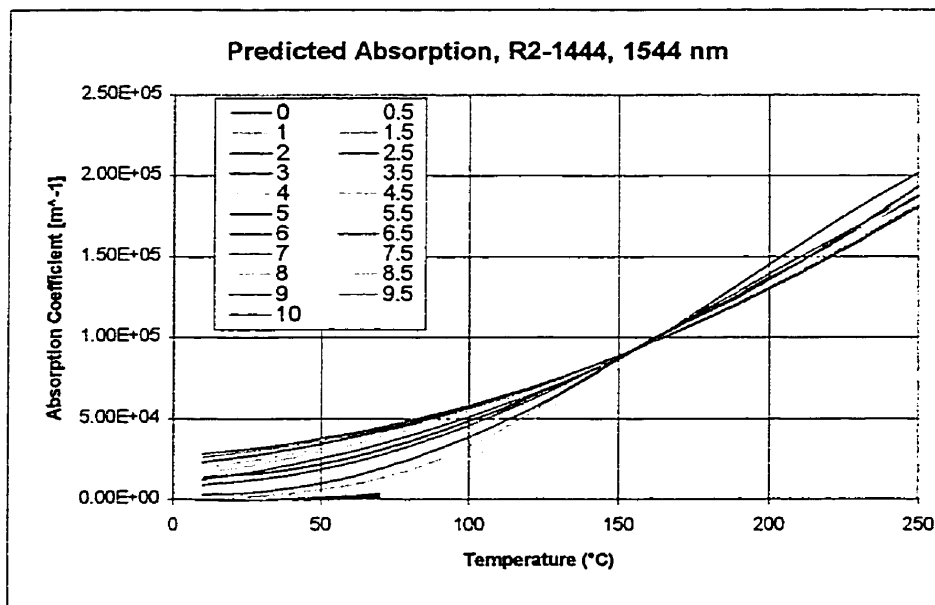
Appendix E - Heat Generation Calculation

Large-Pad Device Model   R2-1444, 1544 nm   T.T.

Lo =   **5.03** mW   V =   **8.00** Volts

x [μm]	Temp. [°C]	alpha [m^-1]	L [mW]	dL [mW]	dI [mA]	dP [mW]	dP/dV [mW/μm³]
0.0	50.2	5043.108	5.030	0.063	0.079	0.158	*0.086*
2.5	66.4	6466.200	4.967	0.080	0.100	0.199	*0.108*
5.0	64.6	6192.754	4.887	0.075	0.094	0.375	*0.204*
7.5	64.0	5854.719	4.812	0.070	0.087	0.350	*0.190*
10.0	61.4	5151.238	4.742	0.121	0.151	0.603	*0.164*
15.0	56.5	4400.911	4.622	0.101	0.126	0.503	*0.137*
20.0	51.8	3715.595	4.521	0.165	0.206	0.825	*0.112*
30.0	46.0	2976.364	4.356	0.252	0.315	1.259	*0.086*
50.0	38.8	2342.382	4.105	0.454	0.567	2.268	*0.062*
100.0	34.0	1985.343	3.651	0.345	0.431	1.725	*0.047*
150.0	31.7	1834.381	3.306	0.398	0.498	1.992	*0.039*
220.0	30.9		2.907				

Photocurrent 220 um: *6.001* mA
Absorption 220 um: *23.92* dB

Notes:
1) Underlined = input parameters
2) *Italic* = Output Values
3) **Lo** is the optical power entering the waveguide; **V** is the applied voltage

Appendix F.1 - Modelling results for the hybrid large-pad device

V	L	P(las)	I	Abs.	Max. Temp. in Pad			... in Laser		Joint Temp.	Joint Diff.
					MQW	Interface	Surface	MQW	Surface	MQW	MQW
[V]	[mW]	[mW]	[mA]	[dB]	[°C]	[°C]	[°C]	[°C]	[°C]	[°C]	[°C]
0.0	8.08	400	0.095	0.042	34.8	34.5	34.5	68.5	58.0	51.7	-
5.0	5.44	400	4.00	5.8	39.8	37.2	37.1	68.6	58.1	52.1	0.4
5.0	6.35	400	6.00	6.1	42.8	38.7	38.6	68.6	58.1	52.3	0.6
5.0	8.23	400	8.00	6.5	46.7	40.4	40.3	68.7	58.2	52.5	0.8
5.0	10.02	400	10.00	7.0	51.7	42.6	42.5	68.7	58.2	52.8	1.1
5.0	11.70	400	12.00	7.5	58.8	45.4	45.2	68.8	58.3	53.0	1.3
5.0	13.27	400	14.00	8.1	72.7	50.0	49.6	68.8	58.3	53.3	1.6
5.0	13.91	400	15.00	8.6	101.3	56.6	55.8	68.9	58.3	53.5	1.8
5.0	13.78	400	16.00	11.5	> 300	> 300	> 300	> 300	> 300	> 300	
6.0	3.34	400	4.00	13.6	44.6	39.2	39.1	68.6	58.1	52.3	0.6
6.0	4.99	400	6.00	14.2	51.2	42.0	41.8	68.7	58.2	52.5	0.8
6.0	6.62	400	8.00	14.8	60.1	45.6	45.3	68.7	58.2	52.9	1.2
6.0	8.32	400	10.00	15.5	73.8	50.3	49.8	68.8	58.3	53.2	1.5
6.0	9.82	400	12.00	16.5	105.9	58.6	57.7	68.9	58.4	53.6	1.9
6.0	10.58	400	13.00	17.7	201.0	72.5	70.1	68.9	58.4	53.9	2.2
6.0	11.35	400	14.00	18.9	> 300	> 300	> 300	> 300	> 300	> 300	
7.0	3.24	400	4.00	19.6	50.8	41.5	41.3	68.6	58.1	52.4	0.7
7.0	4.84	400	6.00	20.4	62.6	46.0	45.6	68.7	58.2	52.8	1.1
7.0	6.45	400	8.00	21.3	81.1	52.0	51.4	68.8	58.3	53.2	1.5
7.0	8.05	400	10.00	22.4	119.5	61.4	60.3	68.9	58.4	53.6	1.9
7.0	8.84	400	11.00	23.2	174.8	70.4	68.4	68.9	58.4	53.9	2.2
7.0	9.63	400	12.00	25.1	> 300	> 300	> 300	> 300	> 300	> 300	
7.5	3.22	400	4.00	21.8	53.8	42.5	42.3	68.6	58.1	52.5	0.8
7.5	4.83	400	6.00	22.7	68.9	47.9	47.5	68.7	58.2	52.9	1.2
7.5	6.43	400	8.00	23.7	94.0	55.4	54.6	68.8	58.3	53.3	1.6
7.5	8.02	400	10.00	25.1	159.0	68.3	66.5	68.9	58.4	53.8	2.1
7.5	8.82	400	11.00	26.9	> 300	> 300	> 300	> 300	> 300	> 300	
8.0	3.21	400	4.00	24.0	56.9	43.6	43.3	68.7	58.2	52.5	0.8
8.0	4.82	400	6.00	25.0	75.5	50.0	49.4	68.7	58.2	53.0	1.3
8.0	6.42	400	8.00	26.1	108.5	58.9	57.9	68.8	58.3	53.5	1.8
8.0	7.21	400	9.00	26.8	143.1	65.8	64.3	68.9	58.4	53.7	2.0
8.0	8.01	400	10.00	28.0	236.0	78.4	75.4	68.9	58.4	54.0	2.3
8.0	8.81	400	11.00	29.2	> 300	> 300	> 300	> 300	> 300	> 300	
9.0	3.20	400	4.00	29.3	64.4	46.1	45.7	68.7	58.2	52.7	1.0
9.0	4.80	400	6.00	30.3	90.4	54.2	53.4	68.8	58.3	53.2	1.5
9.0	6.40	400	8.00	31.6	146.6	66.7	65.1	68.9	58.4	53.7	2.0
9.0	7.20	400	9.00	33.0	253.5	80.7	77.5	69.0	58.4	54.1	2.4
9.0	8.00	400	10.00	33.4	> 300	> 300	> 300	> 300	> 300	> 300	
8.0	8.02	0	10.00	26.4	172.0	66.7	64.7	30.4	30.4	32.1	2.1
5.0	15.39	0	16.00	7.7	78.3	48.2	47.7	30.3	30.3	31.7	1.7
7.5	8.83	0	11.00	24.9	213.1	71.5	68.9	30.4	30.4	32.1	2.1

Notes:
1) P(las) is the electrical power dissipated in the laser in the form of heat.
2) Abs. is the waveguide absorption over the full length of the electrode (220 um).
3) Interface refers to the Semiconductor / Gold interface.
4) The joint is plane where the waveguide and the laser meet together, 80 um away from the pad edge.
5) BC Diff. is the temperature difference at the joint between the stated condition and the case where only the laser heating is present.

Appendix F.2 - Modelling results for the discrete large-pad device

| V | L | I | Abs. | Max. Temp. in AP | | |
| | | | | MQW | Interface | Surface |
[V]	[mW]	[mA]	[dB]	[°C]	[°C]	[°C]
5.00	4.60	4.00	5.2	34.5	32.4	32.4
5.00	6.69	6.00	5.5	37.2	33.8	33.7
5.00	8.67	8.00	5.8	40.3	35.3	35.2
5.00	10.53	10.00	6.3	44.0	37.0	36.9
5.00	12.29	12.00	6.6	49.5	39.3	39.1
5.00	13.93	14.00	7.1	57.8	42.3	42.1
5.00	14.70	15.00	7.3	63.3	44.3	43.9
5.00	15.40	16.00	7.7	77.8	48.1	47.6
5.00	14.61	17.00	11.6	> 300	> 300	> 300
6.00	3.37	4.00	12.9	39.0	34.3	34.2
6.00	5.03	6.00	13.4	44.9	36.8	36.7
6.00	6.67	8.00	14.0	52.3	39.9	39.7
6.00	8.29	10.00	14.6	63.1	43.8	43.5
6.00	9.89	12.00	15.3	82.0	49.6	49.0
6.00	10.68	13.00	15.9	106.8	55.4	54.4
6.00	10.56	14.00	18.1	> 300	> 300	> 300
7.00	3.24	4.00	18.6	44.4	36.3	36.2
7.00	4.86	6.00	19.4	55.1	40.5	40.2
7.00	6.46	8.00	20.2	70.7	45.9	45.4
7.00	8.06	10.00	21.2	99.2	53.7	52.8
7.00	8.86	11.00	21.8	130.0	60.0	58.6
7.00	9.64	12.00	23.7	> 300	> 300	> 300
7.50	3.23	4.00	20.9	47.2	37.4	37.2
7.50	4.83	6.00	21.7	60.2	42.2	41.9
7.50	6.44	8.00	22.6	80.8	48.8	48.2
7.50	8.03	10.00	23.8	126.5	59.3	43.9
7.50	8.83	11.00	24.8	208.3	71.0	68.4
8.00	3.22	4.00	23.0	50.3	38.4	38.2
8.00	4.82	6.00	23.2	66.6	44.2	43.7
8.00	6.42	8.00	25.0	94.2	52.2	51.3
8.00	8.02	10.00	26.4	171.6	66.7	64.7
8.00	8.81	11.00	28.1	> 300	> 300	> 300
9.00	3.2	4.00	28.4	57.4	40.8	40.5
9.00	4.81	6.00	29.3	80.7	48.3	47.7
9.00	7.21	8.00	30.5	126.4	59.4	58.0
9.00	7.21	9.00	31.5	189.1	69.4	67.1
9.00	8.00	10.00	33.2	> 300	> 300	> 300
8.00	3.22	4.00	23.0	50.3	38.4	38.2	5 µm
8.00	4.82	6.00	23.9	66.4	44.1	43.7	5 µm
8.00	6.42	8.00	24.9	93.4	52.0	51.2	5 µm
8.00	7.22	9.00	25.6	117.6	57.6	56.4	5 µm
8.00	8.02	10.00	26.4	166.7	65.9	64.0	5 µm
8.00	8.81	11.00	28.3	> 300	> 300	> 300	5 µm

Notes: 5 um means that the minimum size of the elements
along the ridge was extended from 2.5 to 5 µm

Appendix F.3 - Modelling results for the narrow-electrode device

V	L	I	Abs.	Max. Temp. in AP			
				MQW	Interface	Surface	
[V]	[mW]	[mA]	[dB]	[°C]	[°C]	[°C]	
4.00	2.92	2.00	3.4	25.8	25.9	25.9	
4.00	5.71	4.00	3.6	26.7	26.7	26.7	
4.00	8.39	6.00	3.7	27.5	27.7	27.7	
4.00	10.95	8.00	3.8	28.5	28.7	28.7	
4.00	13.40	10.00	3.9	29.5	29.8	29.8	
4.00	15.75	12.00	4.1	30.6	30.9	30.9	
4.00	18.00	14.00	4.2	31.6	31.9	31.9	
4.00	20.18	16.00	4.4	32.7	33.1	33.1	
4.00	22.28	18.00	4.5	34.1	34.6	34.6	
4.00	24.30	20.00	4.7	35.7	36.3	36.3	
5.00	1.74	2.00	10.9	26.8	26.9	26.9	
5.00	3.47	4.00	11.1	28.7	28.9	28.9	
5.00	5.17	6.00	11.4	30.8	31.2	31.2	
5.00	6.86	8.00	11.8	33.5	34.0	34.0	
5.00	8.52	10.00	12.1	36.7	37.4	37.4	
5.00	10.17	12.00	12.5	41.1	41.8	41.8	
5.00	11.74	14.00	13.0	47.7	48.5	48.5	
5.00	13.36	16.00	13.8	76.4	72.0	71.9	
5.00	14.51	18.00	21.2	> 300	> 300	> 300	
6.00	1.60	2.00	30.5	29.7	29.9	29.9	
6.00	3.20	4.00	31.1	35.4	35.7	35.7	
6.00	4.80	6.00	31.6	42.6	42.9	42.9	
6.00	6.40	8.00	32.3	53.0	52.9	52.9	
6.00	8.00	10.00	33.1	72.3	70.0	69.9	
6.00	9.60	12.00	36.4	> 300	> 300	> 300	
7.00	1.60	2.00	43.9	32.8	32.9	32.9	
7.00	3.20	4.00	44.8	43.0	42.9	42.9	
7.00	4.80	6.00	45.7	57.8	56.9	56.8	
7.00	6.40	8.00	46.8	85.3	79.3	79.2	
7.00	8.00	10.00	49.0	224.9	147.6	146.8	
8.00	1.60	2.00	55.2	35.8	35.8	35.8	
8.00	3.20	4.00	56.2	50.7	50.1	50.0	
8.00	4.80	6.00	57.4	75.0	71.3	71.2	
8.00	6.40	8.00	59.0	138.5	112.2	111.8	
8.00	8.00	10.00	62.4	> 300	> 300	> 300	
9.00	1.60	2.00	70.7	39.7	39.3	39.3	
9.00	3.20	4.00	71.7	60.7	58.5	58.4	
9.00	4.80	6.00	73.0	98.7	88.3	88.1	
9.00	6.40	8.00	75.9	> 300	> 300	> 300	
8.00	1.60	2.00	59.4	41.7	41.6	41.6	To = 30°C
8.00	3.20	4.00	60.5	58.4	57.4	57.4	To = 30°C
8.00	4.80	6.00	61.8	87.5	81.5	81.3	To = 30°C
8.00	6.40	8.00	63.7	177.3	133.0	132.5	To = 30°C

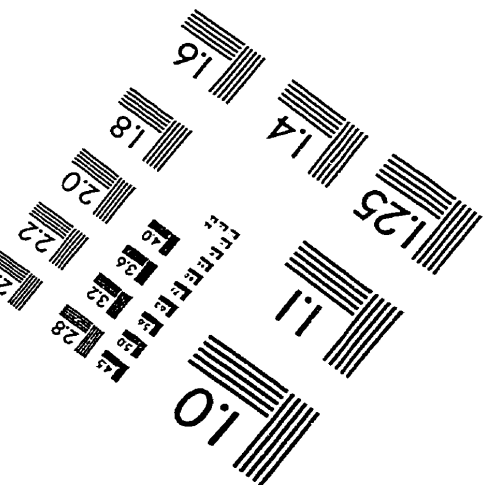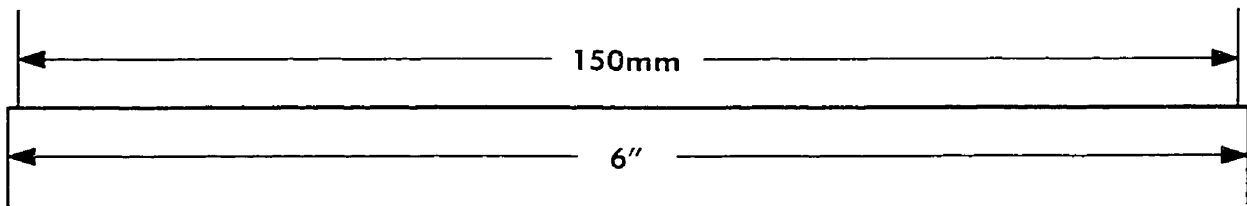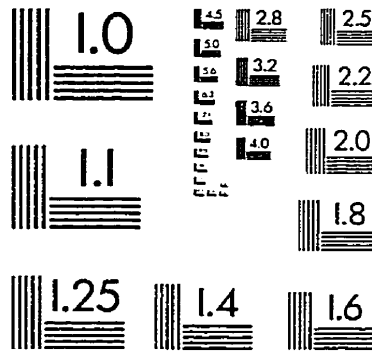Notes: The heat sink temperature was set at 25°C for this device, otherwise stated.
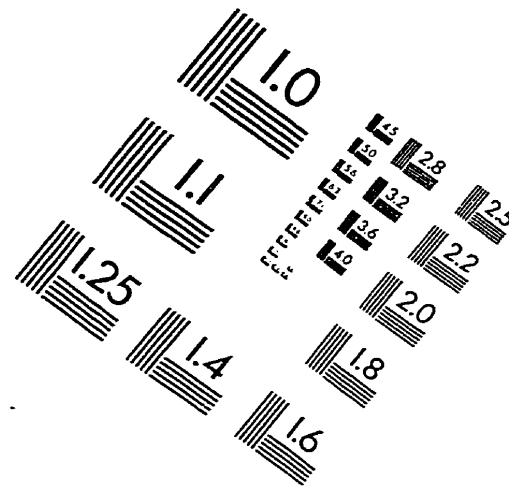
Appendix G - Required Correlation Coefficient for Signifiant Correlation

Size		Level of Confidence			
N		80%	90%	95%	99%
	9	0.472	0.582	0.666	0.798
	8	0.507	0.622	0.707	0.834
	7	0.551	0.669	0.754	0.875
	6	0.608	0.729	0.811	0.917
	5	0.687	0.805	0.878	0.959
	4	0.800	0.900	0.950	0.990
	3	0.951	0.987	0.997	1.000
	2	-	-	-	-
	1	-	-	-	-

Reference:
P. R. Bevington, D. K. Robinson, *Data Reduction and Error Analysis for the Physical Sciences*, 2nd Edition, Mc-Graw-Hill, pp. 255-256 (1992).

IMAGE EVALUATION
TEST TARGET (QA-3)